ABSTRACT

RESOURCE ALLOCATION FOR CDMA DOWNLINK TO ACHIEVE MAXIMUM THROUGHPUT

by
Anil Bircan

Growing interest in cellular phones, wireless modems, instant messaging, pagers with the increasing use of the Internet in daily life indicate that wireless high speed Internet access and wireless multimedia applications are in great demand. The barrier to satisfy this demand is the provision of sufficiently high bit rates in severe wireless mobile channel conditions, for a multitude of services, each requiring different and perhaps even time-varying quality of services (QoS) that can be more demanding than the QoS required by today's voice service. New generation systems will enable provision of a multitude of services each with different QoS and data rate requirements. To resolve problems lying in the integration of new generation systems with today's wireless voice services, several contributions are made as listed below. Signal processing techniques that help analyze the spectral properties and models representing the mobile wireless channel are increasingly important in new generation wireless systems for applications such as multipath mitigation, geolocation, line of sight detection. Models representing the mobile wireless channel and methods to trace the energy concentration in its spectrum are tested and effects of the channel environment are examined. After irregular subbands, equal bin subbands in frequency spectrum which corresponds to Discrete Multitone or Orthogonal Frequency Division Multiplexing methods are analyzed for multicarrier option of next generation wireless services. Noise levels in the multicarriers, environmental effects and availability of the channel are related to achievable bit rates using generic adaptive loading. Advantages/disadvantages of using multicarrier systems versus

single carrier systems are analyzed with decision feedback equalization. In CDMA systems, for a fixed bandwidth allocation, the transmission rate can be altered by varying one or more of the coding, interleaving, modulation and spreading block parameters. In the downlink of DS-CDMA systems, once the parameters of the above mentioned blocks are set, the base station will transmit at the lowest power level that can provide the QoS requirements of the service provided. Different QoS and data rate requirements of communication channels can be satisfied by varying one or more of the coding, digital modulation and spreading blocks. By varying interblock data rates, bit error rate performance simulations are done with the constraint of keeping transmission bandwidth fixed for all configurations as in IS-95. Various coding, digital modulation and spreading rate combinations yield different performance characteristics in AWGN, flat fading and multipath fading environments allowing trade-off decisions on choices of rate, QoS, and implementation. In addition, performance characteristics of multicode CDMA downlink with systematic convolutional (Turbo) coding are obtained under shadowed multipath fading mobile channel. Two different iterative decoding methods are compared in two different synchronous downlink schemes operating under given channel conditions with the same transmission bandwidth as in IS-95. Multicode CDMA with LogMAP decoding is observed to provide better QoS with lower bit and frame error rates, reasonable complexity and shorter decoding delay compared to DS-CDMA downlink with single code pair assigned to each user. With this scheme, higher rate services can be overlayed on existing voice services without any modifications to existing active system architecture.

RESOURCE ALLOCATION FOR CDMA DOWNLINK TO ACHIEVE MAXIMUM THROUGHPUT

by
Anil Bircan

A Dissertation
Submitted to the Faculty of
New Jersey Institute of Technology
in Partial Fulfillment of the Requirements for the Degree of
Doctor of Philosophy in Electrical Engineering

Department of Electrical and Computer Engineering

January 2001

APPROVAL PAGE

RESOURCE ALLOCATION FOR CDMA DOWNLINK TO ACHIEVE MAXIMUM THROUGHPUT

Anıl Bircan

Prof. Ali N. Akansu, Dissertation Advisor — Date
Professor of Electrical and Computer Engineering, NJIT

Prof. Richard Haddad, Committee Member — Date
Professor of Electrical and Computer Engineering, NJIT

Dr. Şirin Tekinay, Committee Member — Date
Assistant Professor of Electrical and Computer Engineering, NJIT

Dr. Joseph Frank, Committee Member — Date
Associate Professor of Electrical and Computer Engineering, NJIT

Dr. ir. Matthijs A. Visser, Committee Member — Date
Member of Technical Staff, Lucent Technologies

BIOGRAPHICAL SKETCH

Author: Anıl Bircan

Degree: Doctor of Philosophy

Date: January 2001

Undergraduate and Graduate Education:

- Doctor of Philosophy in Electrical Engineering,
  New Jersey Institute of Technology, Newark, NJ, Dec. 2000.
- Master of Science in Electrical and Electronics Engineering,
  Bilkent University, Ankara, Turkey, 1996.
- Bachelor of Science in Electrical and Electronics Engineering,
  Hacettepe University, Ankara, Turkey, 1994.

Major: Electrical Engineering

Publications and Presentations:

Anıl Bircan, M. Oğuz Sunay and Ali N. Akansu,
"Downlinks with Variable Interblock Rates and Overlay with Multicodes for 3G CDMA" submitted to IEEE Journal on Selected Areas in Communications.

Anıl Bircan, M. Oğuz Sunay and Ali N. Akansu,
"Multicode CDMA Downlink in Shadowed Multipath Fading",
submitted to IEEE ICC 2001.

Anıl Bircan, M. Oğuz Sunay and Ali N. Akansu,
"Comparison of Different Interblock Data Rate Downlinks,"
Proceedings of IEEE GlobeCom, San Francisco, CA, Nov.28, 2000.

Anıl Bircan, Ali N. Akansu and Şirin Tekinay,
"Model Based Capacity Measurements For Wireless DMT Channels,"
IEEE 33rd Annual Conference on Information Sciences and Systems (CISS), March 17-19, 1999, Baltimore, MD.

Anıl Bircan, Şirin Tekinay and Ali N. Akansu,
"Time-Frequency and Time-Scale Representation of Wireless Communication Channels," IEEE-SP Conference on Time-Frequency and Time-Scale Analysis, pp. 373-376, Oct. 6-9, 1998, Pittsburgh, PA.

A. Altıntaş, A. Bircan, and V.B. Yurchenko,
"Approximating Circular Radome by a Dielectric Slab in the Antenna Simulations," NATO ARW *Microwave Physics and Technique*,
Sept. 30 - Oct. 5, 1996, Sozopol, Bulgaria.

To my family..

ACKNOWLEDGMENT

I would like to thank my advisor Prof. Ali N. Akansu, my committee members Dr. Sirin Tekinay, Prof. Richard Haddad, Dr. Joseph Frank, Dr. Matthijs A. Visser, also Dr. Edip Niver, Dr. Oguz M. Sunay, Dr. Hongya Ge, my intern mentors Dr. Ibrahim Tekin, Dr. Byron Chen, Dr. T.C. Chiang, also Dr. Walter Honcharenko, my friends Dr. Feihong Chen, Alper Altinordu, Dr. Mahalingham Ramkumar, Dr. Tariq, Dr. Amit, Dr. Lale Alatan, Dr. Aydin Alatan, Dr. Aykut Bultan, Sebnem, Burak, Kadir, Zafer, Surong, Dr. Tong Li, Yinchun Li, Liangzhong Chen, Xiadong, Minyi, Taha, Litao, Beongku An, Dr. Sennur Ulukus, Dr. Aylin Yener, Dr. Sitki Timucin, Dr. Mehmet Aktuna, Ramazan Ali Isik, Dr. Nail Cadalli, Dr. Jinwen Ma, Dr. Weichen, Dr. George Elmasry, Bin He, Dr. Xueming, Dr. Mehmet V. Tazebay, Dr. E. Erkip, Dr. Enid Dame, Dr. Murat Okyar, Usha, my mom Gulay, my dad Ismail, my brother Aril and New Jersey Center for Multimedia Research.

TABLE OF CONTENTS

TABLE OF CONTENTS
(Continued)

LIST OF TABLES

LIST OF FIGURES

Figure **Page**

LIST OF FIGURES
(Continued)

Figure **Page**

LIST OF FIGURES
(Continued)

Figure **Page**

LIST OF FIGURES
(Continued)

Figure **Page**

CHAPTER 1

INTRODUCTION

Growing interest in cellular phones, wireless modems, instant messaging, pagers with the increasing use of the Internet in daily life indicate that wireless high speed Internet access and wireless multimedia applications are in great demand. The barrier to satisfy this demand is the provision of sufficiently high bit rates in severe wireless mobile channel conditions, for a multitude of services, each requiring different and perhaps even time-varying quality of services (QoS) that can be more demanding than the QoS required by today's voice service. In response to this demand, much research and standardization activities are being conducted globally towards third generation (3G) wireless systems under the common label "IMT-2000". IMT-2000 is aimed to provide significant improvements over their second generation (2G) counterparts [24]. Physical layer research activities within IMT-2000 include the provision of seamless, high data rate multiuser communication system design that is capable of providing the QoS's that envisioned services require on a multitude of wireless traffic channels. This is currently done with time-division multiple access (TDMA) or code-division multiple access (CDMA) in digital second generation systems and with frequency-division multiple access in analog second generation systems. In IMT-2000, CDMA is widely thought as the multiple access scheme of choice due to its flexibility (In Europe, one path of the GSM evolution is the Wideband CDMA (W-CDMA) system, in the US, IS-95 evolution is cdma2000. Also, in Korea and Japan derivatives of these schemes are being considered). The current efforts in combining the standardization efforts taking place in different parts of the world into a single global standard have resulted in the formation of a number of Task Groups (TG-PP and TG-PP2). Consequently, it has been decided that

the global 3G standard based on the CDMA protocol will have two options (when frequency division duplexed): DS-CDMA and MC-CDMA. The DS-CDMA system will be based on W-CDMA and the MC-CDMA will be based on cdma2000.

In DS-CDMA, all users spread their information symbols over the entire system bandwidth. In Multicarrier CDMA, on the other hand, the available bandwidth is divided into a group of subcarriers. The users' information symbols are demultiplexed across these subcarriers. In [26], BER comparison of DS-CDMA and MC-CDMA systems for frequency selective fading channels is done and it is shown that under certain conditions, both systems have equivalent performance characteristics. The choice of one over the other then, will depend on non-performance related issues such as complexity, need for overlay, QoS provision flexibility.

As stated before, third generation systems will enable provision of a multitude of services each with potentially different QoS and data rate requirements. To resolve problems in the integration of new generation systems with today's wireless voice services, several contributions are made as listed below. Signal processing techniques that help analyze the spectral properties and models representing the mobile wireless channel are increasingly important in new generation wireless systems for applications such as multipath mitigation, geolocation, line of sight detection. Models representing the mobile wireless channel and methods to trace the energy concentration in frequency spectrum are tested and effects of the channel environment are examined. After irregular subbands, equal bin subbands in frequency spectrum which corresponds to Discrete Multitone or Orthogonal Frequency Division Multiplexing methods are analyzed for multicarrier option of next generation wireless services. Noise levels in the multicarriers, environmental effects and availability of the channel are related to achievable bit rates using generic adaptive loading. Advantages/disadvantages of using multicarrier systems versus single carrier systems are analyzed with decision feedback equalization. In CDMA systems, for a fixed

bandwidth allocation, the transmission rate can be altered by varying one or more of the coding, interleaving, modulation and spreading blocks. In the downlink of DS-CDMA systems, once the parameters of the above mentioned blocks are set, the base station will transmit at the lowest power level that can provide the QoS requirements of the service provided. Different QoS and data rate requirements of communication channels can be satisfied by varying one or more of the coding, digital modulation and spreading blocks. By varying interblock data rates, in order to see how these configurations would perform, a performance analysis is done with the constraint of keeping transmission bandwidth fixed as in IS-95 for all configurations. Various coding, digital modulation and spreading rate combinations yield different performance characteristics in AWGN, flat fading and multipath fading environments allowing trade-off decisions on choices of rate, QoS, and implementation. In addition, performance characteristics of multicode CDMA downlink with systematic convolutional (Turbo) coding are obtained under shadowed multipath fading mobile channel. Two different iterative decoding methods are compared in two different synchronous downlink schemes operating under given channel conditions with the same transmission bandwidth as in IS-95. Multicode CDMA with LogMAP decoding is observed to provide better QoS with lower bit and frame error rates, reasonable complexity and shorter decoding delay compared to DS-CDMA downlink with single code pair assigned to each user. With this scheme, higher rate services can be overlayed on existing voice services without any modifications.

The outline of the dissertation is as follows. The models and parameters that define the time-varying, fading wireless channel are covered in Chapter 2. The mobile environment simulation techniques and examples are provided. Spectral properties and energy distribution of the wireless channel are analyzed in Chapter 3 with multiresolution decomposition techniques. Irregular tree structure algorithm tracing the energy localization in the time-varying mobile channel is demonstrated

with examples for various wireless environments. Chapter 4 presents analysis of the channel with equal frequency bands which corresponds to DMT/OFDM systems with generic adaptive loading algorithms. Environmental effects of the channel, noise levels in the multicarriers and achievable bit rates are analyzed in this chapter. Chapter 5 starts with a survey on spread spectrum techniques and diversity methods for CDMA. The second part describes DS-CDMA downlink system utilizing various interblock rates and addresses provision of a multitude of services for 3G CDMA with performance analysis under several channel conditions. In Chapter 6, performance of the multicode structure is investigated under shadowed multipath fading channel. Last chapter summarizes the contributions made, provides discussions on choices of interblock rates, QoS, implementation, trade-off between downlink structure designs, decoding algorithms, complexity, capability of overlaying a higher rate service over an existing standard voice service.

CHAPTER 2

COMPOSITE TIME-VARYING MOBILE WIRELESS CHANNEL MODELING TECHNIQUES

One of the main challenges faced in wireless mobile communications is the physical radio propagation channel due to the interference limitations introduced by its delays and fades. The time-varying setting of the scatterers in the radio propagation environment causes reflection, refraction and scattering of transmitted waves (multipath fading). A distorted version of the transmitted signal is received as a combination of corrupted waves arriving via indirect paths (non-line-of-sight) possibly with an additional direct path (line-of-sight). The time-varying mobile channel is characterized by [1] and widely accepted as the wide sense stationary uncorrelated scattering model. Statistical models have been developed to simulate realistic urban radio propagation channels [2, 3] and more recently indoor channels like factories and buildings [4]. These works provide ways to model the path number distributions, path arrival times and magnitude distributions that best fit the data collected by channel sounding and different kinds of measurements.

Modeling wireless communication channels is crucial for the solutions of many fundamental problems in wireless system design. There have been intensive research efforts on channel modeling. Conventional models have the disadvantages of 1) the necessity for tedious data collection such as channel sounding and measurements, 2) limited reliability in predictive tools with built-in propagation models which put a heavy burden on field engineering. It is also difficult to generalize these channel models which are specific for different environments such as indoor, urban, rural, etc.

The traditional and widely accepted wireless communication channel models are considered in this section. The received signal and the response of a time-varying wireless channel is expressed as [1, 2]

$$r(t) = y(t) + n(t), \qquad y(t) = \int_0^\infty h(t,\tau)x(t-\tau)d\tau, \tag{2.1}$$

respectively, where τ is the delay parameter. The Fourier transform of $h(t,\tau)$ on time variable t is defined as

$$S(\theta,\tau) = \int_{-\infty}^{\infty} h(t,\tau)e^{-j2\pi\theta t}dt,$$

where θ is the Doppler frequency. Therefore, we can rewrite the channel output $y(t)$ in terms of $S(\theta,\tau)$ as

$$y(t) = \int_{0}^{\infty}\int_{-\infty}^{\infty} S(\theta,\tau)x(t-\tau)e^{j2\pi\theta t}d\theta d\tau. \tag{2.2}$$

Similarly, $y(t)$ can be expressed in terms of $T(t,\nu)$ as

$$y(t) = \int_{-\infty}^{\infty} T(t,\nu)X(\nu)\ e^{j2\pi\nu t}\ d\nu, \tag{2.3}$$

where $T(t,\nu)$ is the Fourier transform of $h(t,\tau)$ on variable τ and defined as

$$T(t,\nu) = \int_{-\infty}^{\infty} h(t,\tau)e^{-j2\pi\nu\tau}d\tau. \tag{2.4}$$

The frequency variable for time delay τ is chosen to be ν. Finally, $y(t)$ can be rewritten in terms of $H(\theta,\nu)$ as

$$y(t) = \int_{-\infty}^{\infty}\int_{-\infty}^{\infty} X(\nu-\theta)H(\nu-\theta,\theta)\ e^{j2\pi\nu t}\ d\theta d\nu. \tag{2.5}$$

where

$$H(\theta,\nu) = \int_{-\infty}^{\infty} T(t,\nu)\ e^{-j2\pi\theta t}dt \quad or$$
$$H(\theta,\nu) = \int_{-\infty}^{\infty} S(\theta,\tau)\ e^{-j2\pi\nu\tau}d\tau.$$

Rayleigh distribution is used to describe the received envelope of the fading signal through one path. Envelope of an individual multipath component is the sum of two quadrature Gaussian noise signals and this obeys Rayleigh distribution

$$p(r) = \frac{r}{\sigma^2}e^{-\frac{r^2}{2\sigma^2}}, \quad r \geq 0,$$

where σ^2 is the time-average power of the received signal before envelope detection. Wide sense stationary uncorrelated scattering (WSSUS) model for a fading wireless

channel at the 2GHz. range is used for graphical illustration of the channel models. WSSUS is the most common model due to its characterization of randomly time-varying linear channels [1]. It is assumed that received signals passing through wide-sense stationary (WSS) channel with different Doppler shifts are uncorrelated. Similarly, received signals passing through uncorrelated scattering (US) channel with different scatterer delays are assumed to be uncorrelated. Each simulated received path fading is Rayleigh distributed as they are composed of two orthogonal quadrature components. And the seperate paths are independently generated according to uncorrelated scattering (US) rule. Since the simulated environment is time-varying or mobile, the phase change in the received signal due to the difference in path lengths has to be taken into account. If the velocity of the mobile or the maximum velocity of an obstacle in the environment is v, the difference in path length (electrical length) is $v\triangle t\cos\theta$. So, the phase change can be written as $\triangle\phi = \frac{2\pi v\triangle t}{\lambda}\cos\theta$. Thus, the maximum Doppler shift can be determined as $f_d = \frac{1}{2\pi}\frac{\triangle\phi}{\triangle t} = \frac{v}{\lambda}\cos\theta$, where θ is the angle between direction of the mobile motion and the direction of arrival of the incoming wave. Due to this Doppler shift, the fading coefficients should be filtered so that, the spectrum is centered at carrier frequency and zero outside of $f_c \mp f_d$. Power spectral density of a received signal for a quarter wave vertical antenna with uniform distribution is found as [16, 4],

$$S_{E_z}(f) = \frac{1.5}{\pi f_d\sqrt{1-(\frac{f-f_c}{f_d})^2}}. \tag{2.6}$$

This resulting RF envelope expression is used as the time domain fading waveform to shape the temporal correlation of the Rayleigh fading coefficients generated.

The test environment for the model is vehicular (i.e., maximum Doppler frequency θ=240Hz and maximum velocity $v = \theta \cdot \lambda = 36m/s$) or indoor. Here, please note that θ is used as the Doppler frequency variable instead of f_d. By changing the maximum Doppler frequency and the number of paths, the channel conditions can be modified. The maximum Doppler frequency determines the cutoff

frequency of the Doppler filter used in the channel simulation [16]. 5000 tap FIR filter is used for Doppler spectral shaping. Maximum of 6 scatterers are included in this model to suit the European ETSI or North American COST models.

Figure 2.1 illustrates how the energy is distributed in t-time,τ-delay (upper and lower left), θ-Doppler frequency, ν-frequency (upper and lower right), t-time, ν-frequency (middle left) and θ-Doppler frequency, τ-delay (middle right) planes as given by Eqs. (1-3) and (5). Note in the Doppler frequency dependent curves, the Doppler shaping is just as described in the given power spectral density of received signal envelope formula. On delay axis, we can observe the fading level variation on the different receiving paths in time. On Figure 2.2, we see three different wireless mobile channel conditions with three different Doppler frequencies. Topmost figure has the lowest Doppler frequency, thus the slowest variation in its fading levels with respect to time. The profile at the bottom has the highest mobile velocity, thus the highest maximum Doppler frequency. This results in higher frequency cutoff in the Doppler shaping filter and more correlation between the successive fading coefficients. So, the temporal variation is highest. In pedestrian model we have a 20Hz maximum Doppler frequency. This model represents the transition from indoor to vehicular model. Characterization of the channel can be done with the help of Figure 2.3 [30]. In the figure T_x is the transmitted symbol duration and B_x is the bandwidth of transmitted signal. These values are to be compared with the coherence time and bandwidth. Coherence bandwidth B_c represents the frequency seperation between two frequency components which still demonstrates an amplitude correlation. If the frequency correlation function is taken above 0.5, $B_c \approx \frac{1}{5\sigma_\tau}$, where σ_τ is rms delay spread. This is accepted as a rule of thumb [29] but note that there is not an exact relationship between coherence bandwidth and rms delay spread. Similarly, if the time correlation in the received signal envelope is taken above 0.5, then coherence time can be taken as $T_c \approx \frac{9}{16\pi f_d}$, where f_d is the maximum Doppler frequency. If

Table 2.1 Indoor channel parameters. θ=8Hz, flat Doppler shaping filter.

	path 1	path 2	path 3	path 4	path 5	path 6
Magnitude	1.0000	0.5012	0.1259	0.0398	0.0100	0.0020
Delay (μs)	0	0.0700	0.1700	0.3100	0.4100	0.5300

Table 2.2 Pedestrian channel parameters. θ=20Hz, classical Doppler shaping filter.

	path 1	path 2	path 3	path 4	path 5	path 6
Magnitude	1.0000	0.1660	0.1202	0.0457	0.0178	0.0501
Delay (μs)	0	0.1100	0.2900	0.4100	1.0900	1.3100

more than one multipath are considered in the channel, the category of the simulated wireless channel generally falls into slow frequency selective fading channel. Fast frequency selective fading channels generally arise in satellite communications where the maximum Doppler frequencies far exceed the ones in mobile environments. The rms delay spreads are found as a function of the transmitter-receiver distance and other empirical propagation parameters which are going to be explained in the future chapters where lognormal shadowing is simulated. In the meanwhile, the channel realizations include constant ETSI specified [31] instantaneous excess delay values unless otherwise noted. These values used in the simulations are provided in Tables 2.1-3. In indoor scenario, the Doppler shaping filter is flat rather than the classical shape given by Eq. 2.6.

Table 2.3 Vehicular channel parameters. θ=240Hz, classical Doppler shaping filter.

	path 1	path 2	path 3	path 4	path 5
Magnitude	0.1259	1.0000	0.1000	0.0398	0.0251
Delay (μs)	0	0.3100	1.4900	2.5100	3.3100

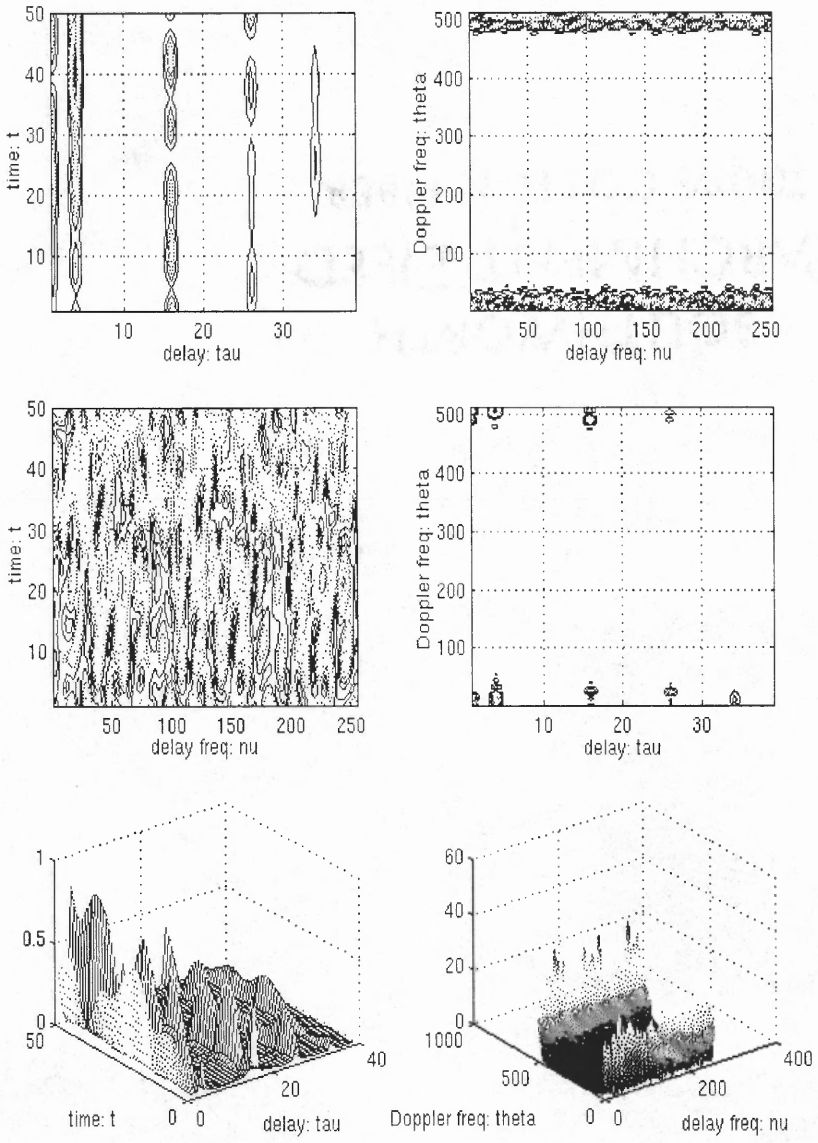

Figure 2.1 Channel model / Energy distribution in time and frequency

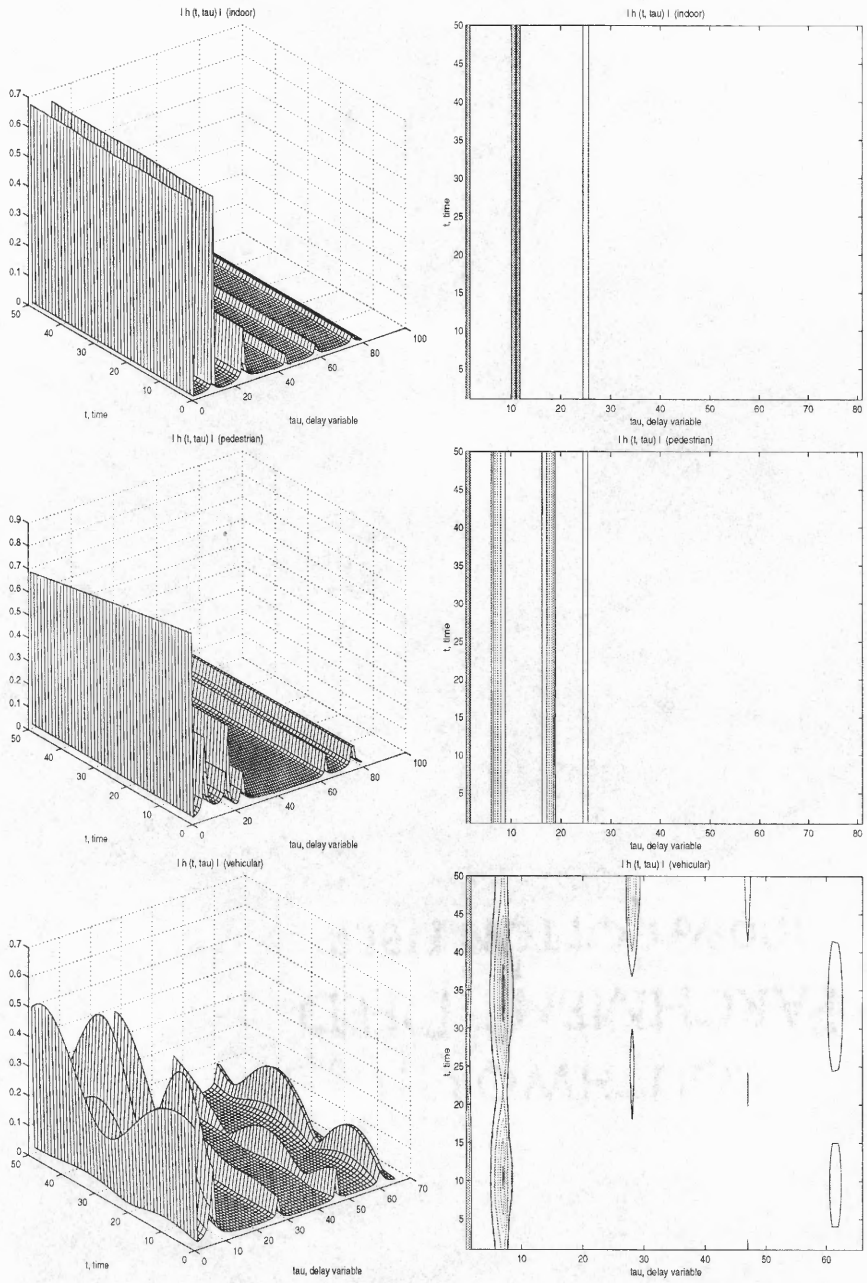

Figure 2.2 From top to bottom: a. Indoor channel model, b. Pedestrian channel model, c. Vehicular channel model, $|h(t,\tau)|$ mesh and contour plots

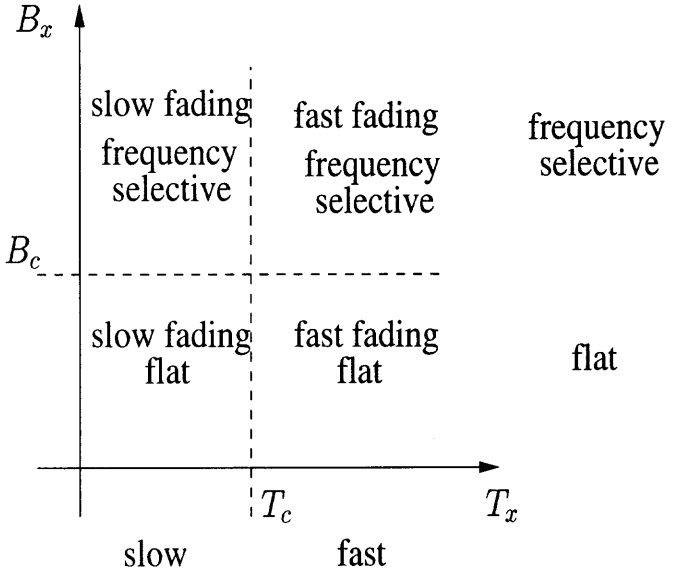

Figure 2.3 Wireless mobile channel characterization

CHAPTER 3

MULTIRESOLUTION DECOMPOSITION OF WIRELESS CHANNELS

Signal processing techniques that help analyze the spectral properties and models representing the mobile wireless channel are increasingly important in new generation wireless systems for applications such as multipath mitigation, geolocation, line of sight detection. Models representing the mobile wireless channel and methods to trace the energy concentration in frequency spectrum are tested and effects of the channel environment are examined in this chapter.

Multiresolution decomposition techniques [6, 7] can be utilized towards possible solutions to the problems of multipath mitigation and line of sight detection in wireless geolocation systems. Spectral properties and energy distribution can be traced and the energy concentration in the frequency domain can be analyzed with the aid of perfect reconstruction (PR) subband filter banks. Analysis and synthesis stages of the PR filter banks allow the reconstuction of the input signal at the end of the synthesis part. The channel impulse response can be thought as a response to unit impulse input. So the tree structure takes the channel impulse response as its input. Using multiband PR analysis/synthesis multirate filter banks [6, 7], resolutions of energy localization in different wireless environments are compared.

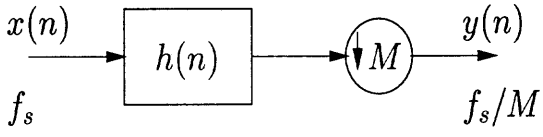

Figure 3.1 Downsampling or decimation.

In a multirate system, after the band-limited signal is sampled at the Nyquist rate, by interpolation or decimation, higher or lower clock rates can be used. Decimation is the process of reducing the sampling rate of a signal by an integer factor of M as shown in Figure 3.1. This is also known as down-sampling. The subsampled signal $y(n)$ is obtained from $x(n)$ as

$$x'(n) = \begin{cases} x(n) & n = 0, \pm M, \pm 2M, ... \\ 0 & \text{otherwise} \end{cases} \tag{3.1}$$

$$y(n) = x'(Mn) = x(Mn). \tag{3.2}$$

In frequency domain, the subsampled signal can be expressed as

$$Y(e^{j\omega}) = \frac{1}{M} \sum_{k=0}^{M-1} X(e^{j(\frac{\omega - 2\pi k}{M})}). \tag{3.3}$$

Time compression corresponds to stretching in frequency domain and the interval $[0 - \pi/M]$ in the original signal $X(e^{j\omega})$ is converted to $[0 - \pi]$ in the downsampled signal $Y(e^{j\omega})$. So if the original signal is not bandlimited to $\pm\pi/M$, we have aliasing. This is avoided by an antialiasing filter $h(n)$ operating before downsampling by factor M. Similarly, interpolation or upsampling is increasing the sampling rate of the

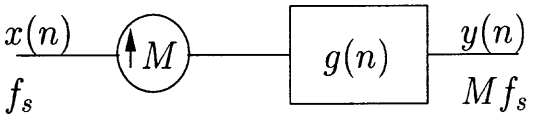

Figure 3.2 Upsampling or interpolation.

input signal by an integer factor M as shown in Figure 3.2. This can be written as

$$y(n) = \begin{cases} x(n/M) & n = 0, \pm M, \pm 2M, ... \\ 0 & \text{otherwise} \end{cases} \tag{3.4}$$

The rate is increased by a factor of M. This is done by padding $M - 1$ zeros between sample values which corresponds to time stretching. In the frequency domain, time

stretch effect appears as compression,

$$Y(z) = \sum_{k=-\infty}^{\infty} x(k)(z^M)^{-k}, \qquad Y(e^{j\omega}) = X(e^{j\omega M}). \tag{3.5}$$

Forcing zeros between the samples or interpolating results in high frequency terms which do not exist in the input signal. The low-pass filter $g(n)$ eliminates these periodic high frequency terms and original signal is retrieved.

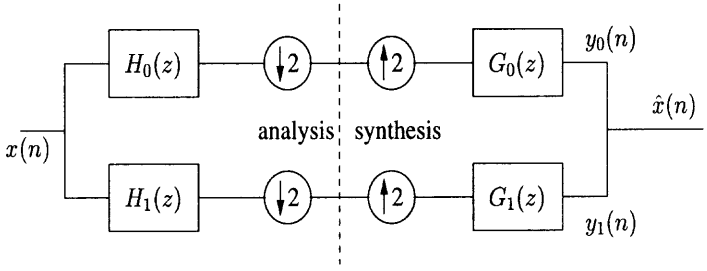

Figure 3.3 Two band PR-QMF subband filterbank.

Downsampling and upsampling are used in the analysis/synthesis sections of the subband decomposition, respectively. A two channel subband analysis/synthesis filter structure is shown in Figure 3.3. The spectrum is analyzed in two parts where the aliasing filters on opposite subbands obey the mirror image property. This property explains the relation between the filters in low and high pass filters. If $h_0(n)$ is the FIR low-pass filter with real coefficients the mirror filter is given as

$$h_1(n) = (-1)^n h_0(n), \quad H_1(e^{j\omega}) = H_0(e^{j(\omega-\pi)}). \tag{3.6}$$

The magnitude is an even function given by

$$|H_1(e^{j(\frac{\pi}{2}-\omega)})| = |H_0(e^{j(\frac{\pi}{2}+\omega)})|, \tag{3.7}$$

which shows the symmetry about $\omega = \pi/2$, hence the name quadrature mirror filters (QMF). The filter pair $H_0(z)$ and $H_1(z)$ are power complementary if they satisfy

$$|H_0(e^{j\omega})|^2 + |H_1(e^{j\omega})|^2 = 1. \tag{3.8}$$

For the M-band filter banks, its extension

$$\sum_{k=0}^{M-1} |H_k(e^{j\omega})|^2 = 1. \tag{3.9}$$

is used.

Refering to Figure 3.3, the input spectrum $X(e^{j\omega})$ is divided into two equal bands. The analysis filters, $H_0(z)$ and $H_1(z)$ satisfy the quadrature mirror and power complementary properties and constitute the analysis filters. With Nyquist sampling, the downsampling is accomplished and the analysis is complete. The synthesis operations follow in the opposite order and we have,

$$Y_0(z) = \frac{1}{2}G_0(z)[H_0(z)X(z) + H_0(-z)X(-z)],$$

$$Y_1(z) = \frac{1}{2}G_1(z)[H_1(z)X(z) + H_1(-z)X(-z)].$$

And we have the reconstructed signal as

$$\begin{aligned} \hat{X}(z) &= \frac{1}{2}[H_0(z)G_0(z) + H_1(z)G_1(z)]X(z) \\ &\quad + \frac{1}{2}[H_0(-z)G_0(z) + H_1(-z)G_1(z)]X(-z) \\ &= T(z)X(z) + S(z)X(-z). \end{aligned} \tag{3.10}$$

Thus, for perfect reconstruction $S(z) = 0$ and $T(z) = cz^{-n_0}$ conditions must be satisfied. The condition $S(z) = 0$ requires

$$\begin{aligned} G_0(z) &= -H_1(-z) \\ G_1(z) &= H_0(-z), \end{aligned} \tag{3.11}$$

and the other condition

$$T(z) = \frac{1}{2}[H_0(-z)H_1(z) - H_0(z)H_1(-z)] \tag{3.12}$$

has to be forced to cz^{-n_0} where c is a constant. Assuming N-tap FIR structures for $H_0(z)$ and $H_1(z)$ filters

$$H_1(z) = z^{-(N-1)}H_0(-z^{-1}), \tag{3.13}$$

where N is even and using power complementary property

$$|H_0(e^{j\omega})|^2 + |H_1(e^{j\omega})|^2 = 1 \tag{3.14}$$

the conditions for PR-QMF filter design for a two-band subband decomposition can be stated as follows [6]:

$$\begin{aligned} H_1(z) &= z^{-(N-1)}H_0(-z^{-1}) \\ G_0(z) &= z^{-(N-1)}H_0(z^{-1}) \\ G_1(z) &= z^{-(N-1)}H_1(z^{-1}). \end{aligned} \tag{3.15}$$

Multirate techniques provide the basic tool for multiresolution spectral analysis and with PR-QMF banks the input spectrum is divided into equal subbands. In two-band PR-QMF split we have low (L) and high (H) bands. These (L) and (H) half bands can further be split into quarter bands (LL), (LH), (HL), (HH) as in Figure 3.4. Levels of decompositions can be implemented in a simpler and practical way as shown in Figure 3.5. With the equivalent representation of the analysis filters

$$\begin{aligned} H_0'(z) &= H_0(z)H_0(z^2) \\ H_1'(z) &= H_0(z)H_1(z^2) \\ H_2'(z) &= H_1(z)H_0(z^2) \\ H_3'(z) &= H_1(z)H_1(z^2), \end{aligned} \tag{3.16}$$

and by a 4 downsampler at the end, the filterbank structure in Figure 3.5 can be justified. The subband filterbank structures shown so far represent regular, binary,

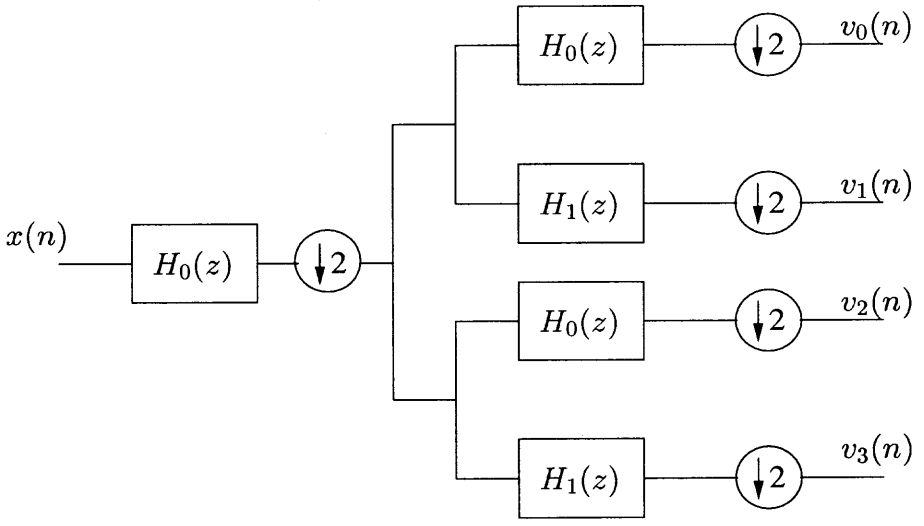

Figure 3.4 Four band PR-QMF subband analysis filterbank.

full splits in the spectrum. However real signal sources are concentrated unevenly in the spectrum. That is, some parts of the spectrum are more significant than others because they contain more energy. Unequal bandwidths can be assigned according to more significant parts of the analyzed signal by terminating the subband structure at different levels of the tree. Thus, the frequency bands of the irregular tree structure have unequal allocated bandwidths. A property which is used to simplify the subband filterbanks is provided in Figure 3.6. This property is particularly useful for implementing practical irregular tree structures.

Assuming a unit impulse input to the wireless mobile fading channel described in Chapter 2, the signal is observed to have unequal energy distribution in its frequency spectrum. In the following, the method to analyze and monitor the energy localization in the multipath delay frequency is described. Since it is time-varying, during the analysis/synthesis process, the channel keeps changing and the multirate

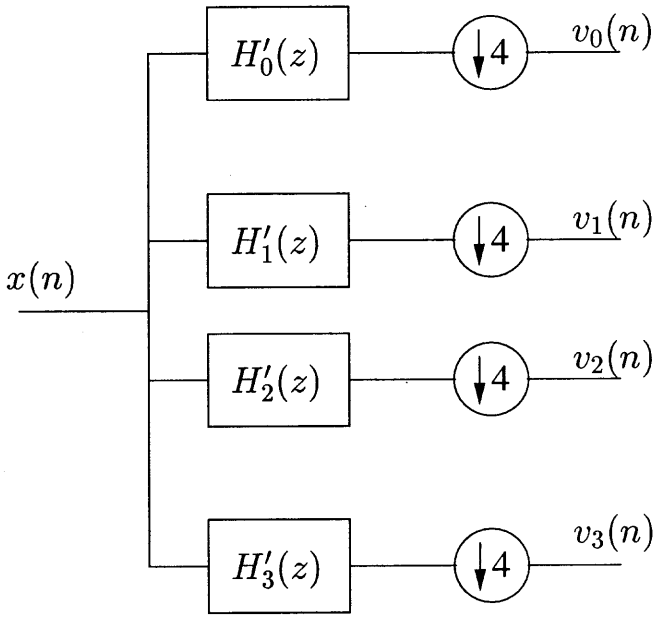

Figure 3.5 Four band PR-QMF equivalent subband analysis filterbank.

adaptive filter banks keep track of this time-varying change in the spectral energy distribution. That is the tree structure is updated according to the new spectral energy distribution. Unevenness of the channel spectrum $|T(t_0, \nu)|$ at every time instant is quantified based on the energy compaction measure,

$$G_{TC} = \frac{\frac{1}{N}\sum_{i=1}^{N}\sigma_i^2}{(\prod_{i=1}^{N}\sigma_i^2)^{\frac{1}{N}}}, \tag{3.17}$$

where σ_i^2 is the power in the i^{th} band of the spectrum. This measure is calculated for two and three spectral splits [7]. The splits are decided by the help of ideal brickwall subband filters. Once the tree structure is complete, the practical filters are designed instantly with the equivalent analysis/synthesis filterbank structure provided in Figure 3.6. The split that provides greater compaction is used to decide which spectral split results in better energy localization in frequency domain. A

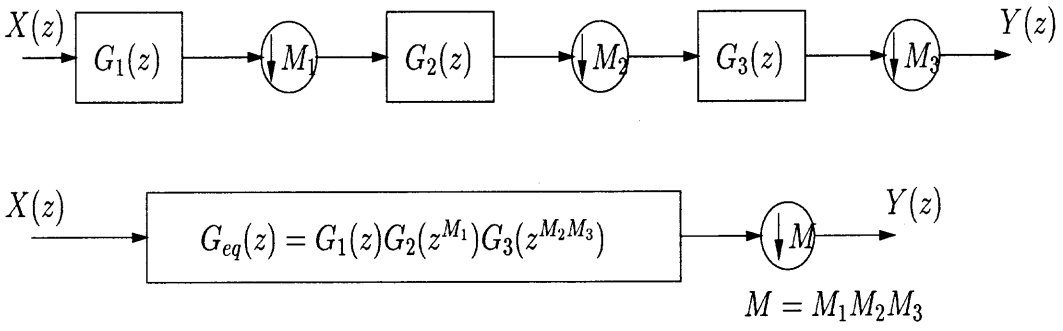

Figure 3.6 Equivalent structures

preset compaction threshold is used to decide if spectral split is needed. This preset compaction measure can be tuned according to the depth of resolution required by the particular wireless channel conditions. The minimum energy which a node should carry is taken as the stopping criteria or tree termination. The result of this procedure is always an irregular subband tree structure for frequency selective mobile channels. Flat fading channels demostrate a totally uniform energy distribution. The tree structure is formed by using ideal brickwall filters. But for practical implementation of this tree structure, practical perfect reconstruction quadrature mirror filters (PR-QMF) are used.

To see the energy localization in different types of wireless environments, an indoor (maximum Doppler frequency $\theta = 8Hz$) and a vehicular scenario ($\theta = 240Hz$) are chosen. In-phase parts of these channel models are analyzed with the procedure described. The spectra and corresponding tree structures are displayed in Figures 3.7 and 3.8. It is observed from these figures that the channel properties change from indoors to vehicular. Finer resolution tree structures have to be obtained due to increased maximum velocity (or Doppler frequency) and increased complexity.

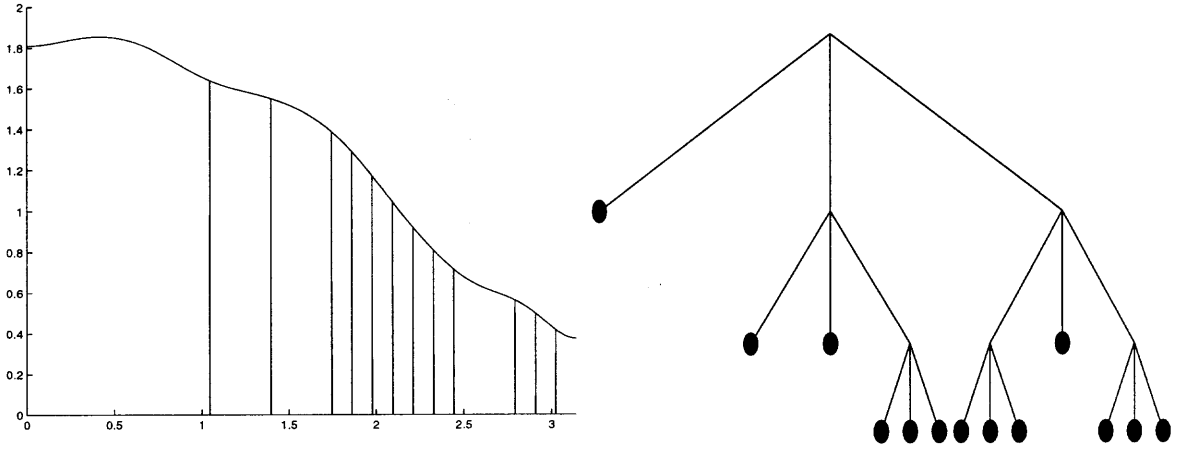

Figure 3.7 a. $|T(t_0, \nu)|$ and ideal tree structure output, b.Tree structure for a wireless indoor channel model signal

As new channel data is available, the tree structure will be formed again taking the new channel data as input. So, it adapts itself to the variations of the time-varying wireless channel [12]. Figure 3.9 shows the implementation of the irregular tree structure obtained for the instantaneous indoor channel shown in Figure 3.7. The alternative implementation property in Figure 3.6 helps an easier by-product architecture rather than the hierarchical one. Here, $H_l(z)$, $H_b(z)$ and $H_h(z)$ are the 3 band PR filters. Implementation of tree structure for the vehicular case or any other case can be performed in a similar manner. Please note that only the analysis stage of the whole system is shown. The 3-band filter design is done in a similar way using the same filter properties as explained earlier. With the forced perfect reconstruction conditions [6, 8] in the synthesis filter design, the input signal is retrieved with a negligable PR error after the synthesis stage. Results of the implemented analysis/synthesis subband decomposition are provided in Figures 3.10

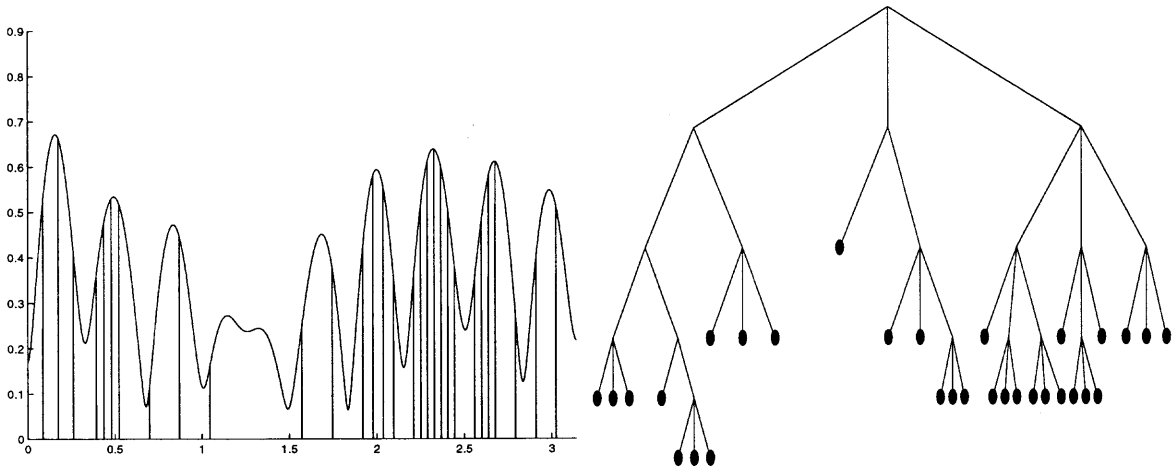

Figure 3.8 a. $|T(t_0, \nu)|$ and ideal tree structure output, b. Tree structure for a wireless vehicular channel model signal

and 3.11. These figures show the same channel environment sampled at different instants. In Figure 3.11 (c), we see the input and PR-QMF filterbank synthesis output superimposed. Everytime the tree structure is built and implemented with practical filters, the original signal is retrieved with negligible PR error.

Finally, in this chapter, we highlight the drawbacks of the conventional channel models and justify the approach of "extended processing" for better resolution. The resolution of a signal is known to be represented by the reciprocal of the time-bandwidth product of the signal [5]. Excitation of the mobile time-varying channel with a fine resolution signal (large time-bandwidth product) would result in the so-called "wideband condition"; i.e., the maximum distance the mobile can move during the signal (maximum velocity $\times$ signal duration) exceeds the signal resolution [5]. When the wideband condition is valid, extended processing can be used as described next. Conventional models assume the channel to be stationary over the

processing interval whereas nonnegligible channel variations occur within a symbol period. Hence, the performance and gain of the mobile system is limited. For wideband condition, the system response is written as [5]

$$y(t) = \int_{-\infty}^{\infty} \int_{-\infty}^{\infty} W(a,b,t) \frac{1}{\sqrt{a}} x(\frac{t-b}{a}) \frac{db\, da}{a^2}, \tag{3.18}$$

where $W(a,b,t)$ is the wavelet transform coefficients of $h(t,\tau)$ on delay variable τ [6]

$$W[h(t,\tau)] = W(a,b,t) =< h(t,\tau), \psi(a,b,\tau) >= \int_{-\infty}^{\infty} h(t,\tau)\ \psi^*(a,b,\tau)\ d\tau. \tag{3.19}$$

The values of $W(a,b,t)$ in time, unlike the usual $h(t,\tau)$, are valid for longer processing durations where the channel is changing linearly with time. In conventional approaches, the processing duration is limited by the bandwidth of the signal and possible mobile velocities in the environment. In contrast, in the extended modeling [5], this duration is limited only by the bandwidth and the accelerations as opposed to the velocities.

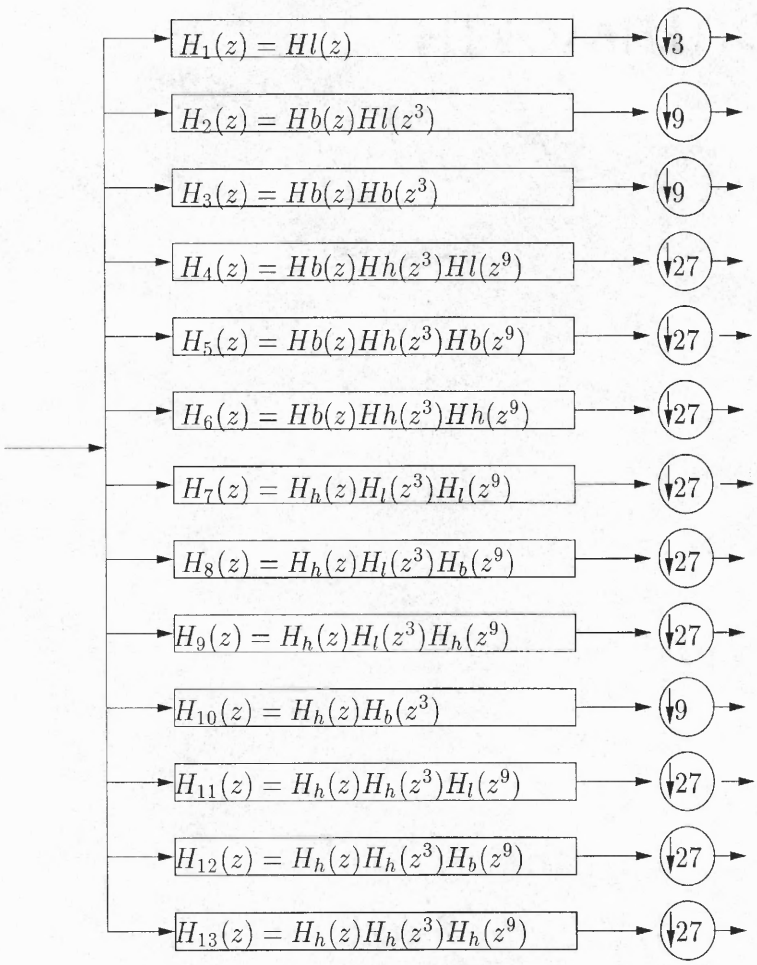

Figure 3.9 Implementation of tree structure shown in Figure 3.7.

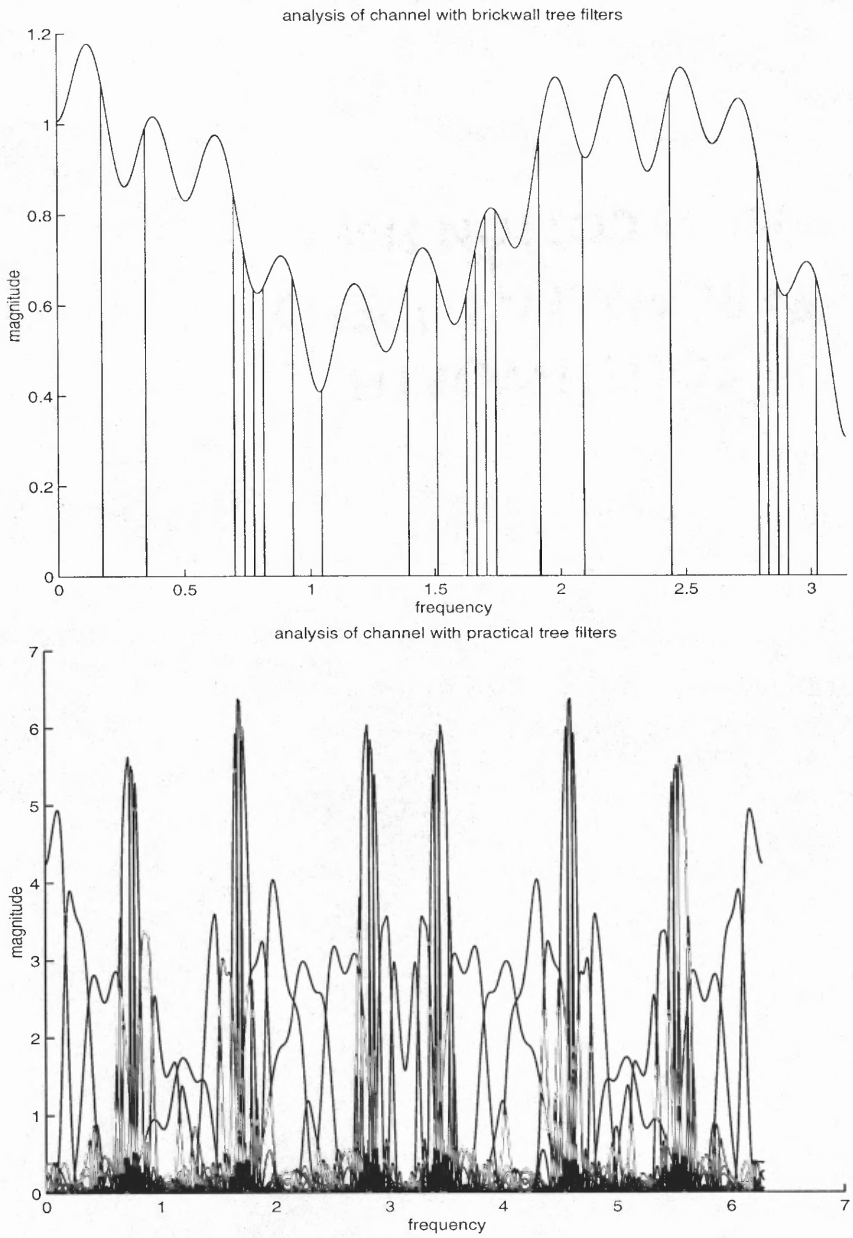

Figure 3.10 a. Ideal brickwall tree structure formation for a pedestrian channel, b. Practical PR-QMF filter output of the pedestrian channel in (a).

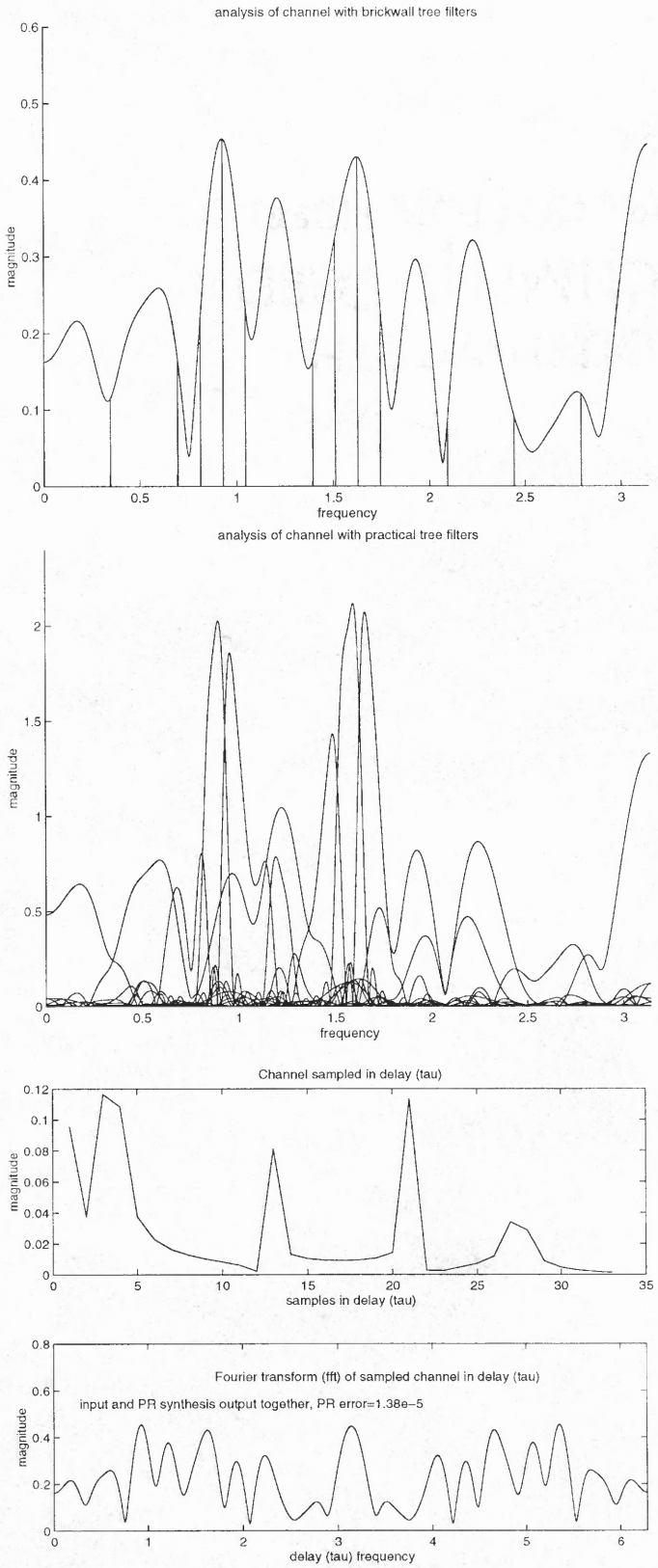

Figure 3.11 a. Ideal brickwall tree structure formation for a pedestrian channel at a different instant, b. Practical PR-QMF filter output of the pedestrian channel in (a), c. Original signal and PR analysis/synthesis filterbank output superimposed.

CHAPTER 4

DISCRETE MULTITONE (DMT) AND ORTHOGONAL FREQUENCY DIVISION MULTIPLE (OFDM) ACCESS SYSTEMS

After irregular subbands investigated in the previous chapter, now, equal bin subbands in frequency spectrum which corresponds to Discrete Multitone or Orthogonal Frequency Division Multiplexing methods are analyzed in this chapter, for multicarrier option of next generation wireless services. Noise levels in the multicarriers, environmental effects and availability of the channel are related to achievable bit rates using generic adaptive loading. Advantages/disadvantages of using multicarrier systems versus single carrier systems are analyzed with decision feedback equalization.

We are now focusing on optimal ways of power distribution among QAM modulated multicarrier systems with no spreading sequence for a single user. This involves several multicarriers which carry the digitally modulated transmission data through the wireless channel. In addition to QAM digital modulation, basic PSK schemes will also be considered. Advantages and disadvantages of using multicarriers and the power distribution among the multicarriers will be addressed in this chapter.

A multicarrier modem can be implemented in several ways. One commonly used technique is called discrete multitone modulation (DMT) [9, 10, 19, 27] and is shown in Fig. 4.1. Encoded data bits are transmitted in parallel non-overlapping subchannels. An alternative technique is called orthogonal division multiplexing (OFDM) [27, 28]. This technique allows subchannels to overlap.

For calculating achievable bit rates for a given wireless channel impulse response, a discrete multitone transceiver system is considered [9, 10, 11]. As outlined in Fig. 4.1, input bits are encoded and converted from serial to parallel. QAM modulation is applied in each subchannel according to the channel condition. Channel state information is assumed to be provided to transmitter. Each subcarrier

carries bits which is assigned according to this channel information as will be explained later in this chapter. The channel is partitioned into its orthogonal subchannels. Orthogonality and frequency separation is obtained using the multi-carrier modulation - inverse Fourier transform (IFFT). The input to the IFFT block is composed of complex QAM symbols and can be assumed to be in frequency domain. Inverse Fourier operation transforms the signal into time domain. Symmetry [20] is assured so that the IFFT output is real in time domain. After parallel to serial conversion, signal is converted from digital to analog and RF filter operates before the antenna.

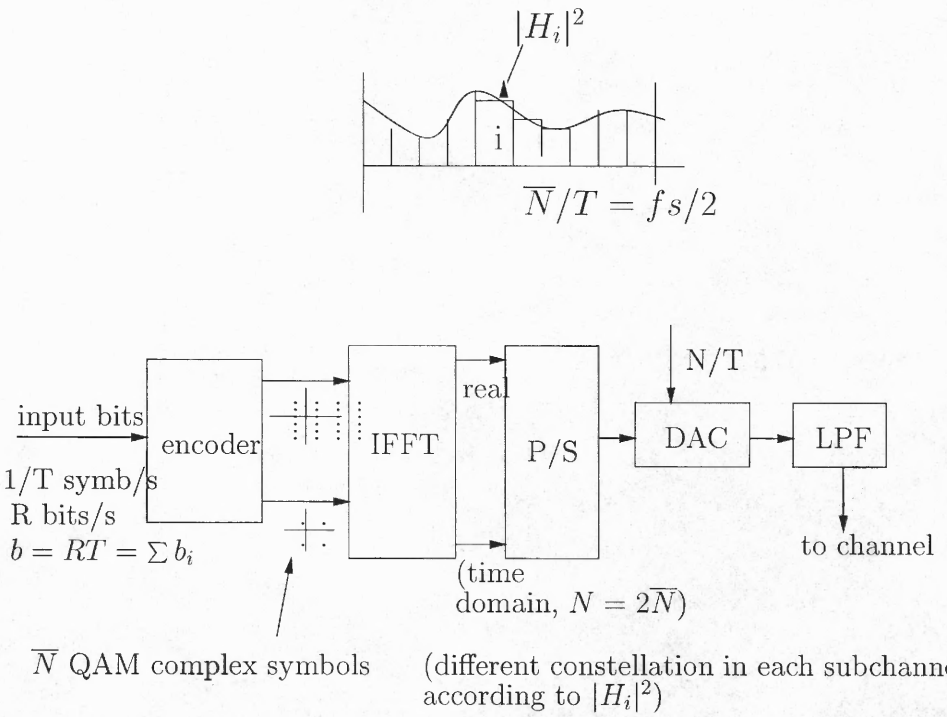

Figure 4.1 Discrete multitone transmitter used for capacity measurements.

In each subchannel, same probability of error is assumed. This is enforced by

$$\frac{Pr\{E\}}{2} = 10^{-7} \leq 4Q(\frac{d_{min}}{N_0}), \tag{4.1}$$

where d_{min} is the minimum distance between the signal points in the QAM constellation at the receiver and N_0 is the noise variance.

Number of bits assigned to subchannel i is n_i. The constellation size is $M = 2^{n_i}$. As in [9], the total transmitted power of each QAM signal is P_i and total transmitted power is equal to P, i.e. $P = \sum P_i$. Solution of the QAM constellation gives

$$Pr\{E\} = 4(1 - \frac{1}{\sqrt{2^{n_i}}})Q(\frac{3k_iP}{N_0W_i(2^{n_i} - 1)}), \tag{4.2}$$

where W_i is the bandwidth of the subchannel. Half of the channel sampling frequency corresponds to $\sum Wi$ if Nyquist sampling rate is used. The power distribution is done with the factor k_i. To find k_i we solve the information theoretic bit rate maximization problem with low probability of error restriction. One additional constraint is the minimum QAM constellation size. Clearly, $\sum k_i = 1$. Solving the Lagrange multiplier bit rate maximization problem [9], one gets

$$k_i = \lambda - \frac{1}{K_0|H_i|^2}, \tag{4.3}$$

where

$$K_0 = \frac{3P_{total}/N_0W_i}{[Q^{-1}(PrE/4)]^2}. \tag{4.4}$$

With the assumption that the transmitter has enough power this power distribution yields equal water pouring into the subchannels. Conditions of low transmitted SNRs and deep spectral attenuation in the channel make the water pouring loading more practical. This power loading scheme is adaptive because as the channel conditions change, this information is fedback to transmitter and bits are distributed accordingly into the subchannels.

Granularity and impracticality issues are investigated in water pouring algorithms, due to intense searching and peak number values reached in the algorithm [9]. It is also possible to approach the adaptive loading problem by keeping the transmission bit rate constant and minimizing the probability of error [14, 15].

Total achievable bit rate can be obtained as

$$Rb = W \sum_{i=1}^{\overline{N}} \log_2(1 + \frac{3|H_i|^2 P_{tot} k_i / N_0 W}{[Q^{-1}(\frac{PrE}{4})]^2}). \tag{4.5}$$

Inphase and quadrature parts of complex channel are used in capacity calculations. For infinite number of subchannels the summation turns to an integral and this is capacity of the system. Bandwidth efficiency is given as C/W.

In this section, information theoretic capacity simulations and results will be discussed. For these simulations, the multicarrier system described in Figure 4.1 and the channel model described in Chapter 2 are used.

4.1 Model Based Capacity Measurements For Wireless DMT Channels

In this section, wireless channel capacity is shown to be sensitive to the effects of various wireless channel parameters by use of computer simulations [17].

It was previously shown that [12], as the channel scatterer numbers, magnitudes and delays are kept constant in the model, the capacity stays the same for different mobile velocities (or the maximum Doppler frequency) involved in the channel.

The capacity is normalized by the efficient bandwidth as R_{DMT}/W yielding bandwidth efficiency in bits/sec/Hz units. In all of the following simulations $S_x(t, \nu) = 1$ is chosen. In Figure 4.2, the effect of the number of scatterers on the bandwidth efficiency is illustrated for indoor, pedestrian and vehicular scenarios. Realistic maximum excess delays are chosen as $3.31\mu s$, $1.31\mu s$ and $0.53\mu s$ for vehicular, pedestrian and indoor scenarios, respectively. For each number of

scatterers the same sampling frequency is used in each propagation scenario. The same fading coefficients are assumed for the different paths in the simulations. At each point in the plot, 10000 capacity values are calculated at succesive time samples and averaged. For a fair comparison, all the channel responses are taken to be unit power discrete signals (Figure 4.2b). 10 unit magnitude scatterers are chosen to be uniformly distributed in [0, maximum excess delay] range on time delay axis for simplicity. In order to realistically assess the case, a vehicular example is chosen. This is illustrated in Figure 4.3. Realistic values for magnitudes and arrival times for the scatterers are considered.

To see the effect of the sampling frequency chosen, three simulations with different sampling frequencies are performed for the same conditions. This is displayed in Figure 4.4. The chosen sampling frequencies reflect the receiver sensitivity and path resolving ability of the receiver. Naturally, as the sampling frequency is increased better performance results are obtained ($fs_1 < fs_2 < fs_3$).

In order to observe the effect of the path arrival times involved in the wireless channel on the system performance, 10 unit magnitude paths in a vehicular environment are considered. The delay difference between two successive paths is constant (7 sampling periods for this simulation) when no time shift is applied to the path delays. To introduce randomness to the delays of the arriving paths, independent Gaussian random variables with zero mean and nonzero variance are added to the path time delays. Figure 4.5 displays the bandwidth efficiency of the vehicular channel for different variances of delay shift random variables. For each variance value, 200 shift random variable vectors are generated and averaged. In each case, 1000 time samples are used to average the capacity. The simulation is carried out for 2, 10 and 20 paths. The capacity increases as the path arrival times are shifted from their uniform places on time delay axis with higher variances. All channel responses generated are unit norm discrete signals.

Table 4.1 Matched filter inputs (decision equations) and corresponding probability of errors for different intersymbol interferences (ISI) introduced by the channel.

Channel Type	Decision Equation	Probability of Error
AWGN, $h(\tau) = \delta(\tau)$	$z_i = \sqrt{E}b_i + \eta$	$Pe = Q(\sqrt{\frac{2E}{N_0}})$
AWGN+ISI($T/3$), $h(\tau) = \delta(\tau) + \delta(\tau - T/3)$	$z_i = \sqrt{E}b_i + \sqrt{E}(\frac{1}{3}b_{i-1} + \frac{2}{3}b_i) + \eta$	$Pe = \frac{1}{2}Q(2\sqrt{\frac{2E}{N_0}}) + \frac{1}{2}Q(\frac{4}{3}\sqrt{\frac{2E}{N_0}})$
AWGN+ISI($T/2$), $h(\tau) = \delta(\tau) + \delta(\tau - T/2)$	$z_i = \sqrt{E}b_i + \sqrt{E}(\frac{1}{2}b_{i-1} + \frac{1}{2}b_i) + \eta$	$Pe = \frac{1}{2}Q(2\sqrt{\frac{2E}{N_0}}) + \frac{1}{2}Q(\sqrt{\frac{2E}{N_0}})$
AWGN+ISI(T), $h(\tau) = \delta(\tau) + \delta(\tau - T)$	$z_i = \sqrt{E}b_i + \sqrt{E}b_{i-1} + \eta$	$Pe = \frac{1}{4} + \frac{1}{2}Q(2\sqrt{\frac{2E}{N_0}})$
AWGN+ISI(ϵT) ($0 < \epsilon < 1$), $h(\tau) = \delta(\tau) + \delta(\tau - \epsilon T)$	$z_i = \sqrt{E}b_i + \sqrt{E}(\frac{1}{2}b_{i-1} + \frac{1}{2}b_i) + \eta$	$Pe = \frac{1}{2}Q(\sqrt{2\frac{2E}{N_0}}) + \frac{1}{2}Q(\sqrt{\frac{2E}{N_0}})$
AWGN+ISI($1.5T$), $h(\tau) = \delta(\tau) + \delta(\tau - 1.5T)$	$z_i = \sqrt{E}b_i + \sqrt{E}(\frac{1}{2}b_{i-2} + \frac{1}{2}b_{i-1}) + \eta$	$\frac{1}{8} + \frac{1}{2}Q(\sqrt{\frac{2E}{N_0}}) + \frac{1}{4}Q(2\sqrt{\frac{2E}{N_0}})$

In order to introduce randomness in the magnitudes of the paths involved in the channel, independent Gaussian random variables with unit mean and nonzero variance are assigned as magnitudes to the paths which are distributed uniformly on the time delay axis. Figure 4.6 shows the bandwidth efficiency of the vehicular channel for different variances of the magnitude random variables. For each variance value, 500 magnitude random variable vectors are generated to average. In each case, 2000 time samples of vehicular channel are used to average capacity. The simulation is performed for 2, 8 and 20 paths for illustration. With nonzero variances of the magnitudes, the average power of the channel impulse responses is not constant. This is corrected for a fair comparison by power normalization of the channel impulse responses before the capacity calculation in each simulation. Bandwidth efficiency is observed to be higher for larger values of magnitude variances.

4.2 Performance Comparison of Single Carrier and Multicarrier Systems

Multicarrier modulation systems provide greater immunity to impulse noise and fast fades with their longer symbol time. They also have ability to combat frequency selectivity of wireless channels. However, it was shown that their performance isn't quite different than single carrier systems' under certain conditions [18, 19]. Rather than QAM modulation which was the case in the earlier simulations, with BPSK modulation, performances of a single carrier and a multicarrier system are analyzed and compared for simple AWGN channels with and without ISI in this section.

In a single carrier system, the transmitted BPSK signal can be written as

$$s(t) = \sqrt{E} \sum_{j=-\infty}^{\infty} b_j p_T(t - jT) \cos \omega_c t, \tag{4.6}$$

where E is the energy, $b_j \in \{-1, 1\}$, ω_c is the carrier frequency. Pulse shape is shown in Figure 4.7 as $p_T(t)$. The matched filter or correlator receiver structure is defined as in Figure 4.7. AWGN is taken as $u(t) : N[0, N_0/2]$. Decision variable z_i is found to be

$$z_i = b_i \sqrt{E} + \eta \tag{4.7}$$

for $h(t) = \delta(t)$, i.e. AWGN only channel where $\eta : N[0, N_0/2]$. Probability of error can be found as

$$Pr\{E\} = \frac{1}{2} P(e|1) + \frac{1}{2} P(e|0) = Q(\sqrt{\frac{2E}{N_0}}). \tag{4.8}$$

Excess delay in the channel causes combined partial reception of consequent symbols at the receiver in $[iT, (i+1)T]$. In coherent detection this results in increased probability of error and is called intersymbol interference [20]. Severeness of it depends on the symbol duration of the transmitted signal and delay of the channel. For several delays, the decision expressions and the corresponding probability of errors are shown in Table 4.1. These results are plotted in Fig. 4.8. As the delay

increases from 0 to multiples of T, higher probability of errors result. In the figure, $T/3$, $T/2$, $2T/3$, $0.93T$ and T ($m = 1$) curves show how the receiver faces an error floor as it tries to demodulate the signal. As the delay becomes longer than the symbol period T, the performance curve starts oscillating between two error floors as shown between the mT and $mT + T/2$ curves (m is a positive integer).

Compensation of the intersymbol interference, or in other words, improving the degraded system performance due to channel distortion can be solved by equalization [20]. Decision feedback equalization is the generally prefered equalization scheme. The current decision $\hat{b_i}$ is fed back to the input of the symbol-by-symbol detector to remove the intersymbol interference from the present decision z_i. In Figure 4.8, for AWGN+ISI channel single carrier analytical and simulation results are shown. DFE is applied to the receiver for the channel $h(\tau) + h(\tau - T)$ (ISI, 1+T) to remove the intersymbol interference. The decision feedback in practice could be inaccurate due to incorrect estimation of channel parameters. For imperfect ($0.5T$ and $0.75T$) delays fedback to the detector input, the simulations show that the receiver overcomes the error floor and reaches AWGN performance for high SNR values. Perfect delay DFE simulation performance is the best achievable curve for a practical single carrier DFE system. Ideally, the correct bits would be fed back with perfect delay and the performance would give the same results as the AWGN performance.

For comparison, a multicarrier system with 3 subcarriers is chosen. The transmitter and receiver structure is shown in Fig. 4.10. For N subcarriers, the transmitted signal can be written as

$$s(t) = \sqrt{E} \sum_{j=-\infty}^{\infty} [\sum_{n=0}^{N-1} d_{jn} \cos(2\pi f_n t)]\, p_T(t - jT), \tag{4.9}$$

where one multicarrier symbol duration is $T = N\triangle t$ and rate $R = 1/\triangle t$ is slowed down to R/N in each subchannel after serial to parallel conversion. For AWGN channel, the decision random variable in each subchannel in the receiver can be

found as

$$z_{im} = \int_{iT}^{(i+1)T} [s(t) + n(t)]\, 2\cos 2\pi f_m t\, dt = \sqrt{E} d_{im} + \eta. \tag{4.10}$$

For an AWGN channel with intersymbol interference ($h(t) = \delta(t) + \delta(t - \tau)$), the received signal is $r(t) = s(t) + s(t - \tau) + n(t)$ and decision variables can be written as

$$z_{im} = \sqrt{E}[d_{im}\frac{\tau}{T} + d_{(i-1)m}(\frac{T - \tau}{\tau})] + \eta. \tag{4.11}$$

Equations 4.17 and 4.18 are the same analytical expressions found for single carrier system decision variables. The performance curves for this multicarrier system appears as in Figure 4.9. In each branch of the receiver, DFE can be applied, this would give similar results as in Figure 4.9. These results are in agreement with the comparisons in [10, 11, 19]. In practice, imperfect filtering in the multicarrier receiver results in intercarrier interference (band spill-over). This is another factor that degrades the performance of the multicarrier system.

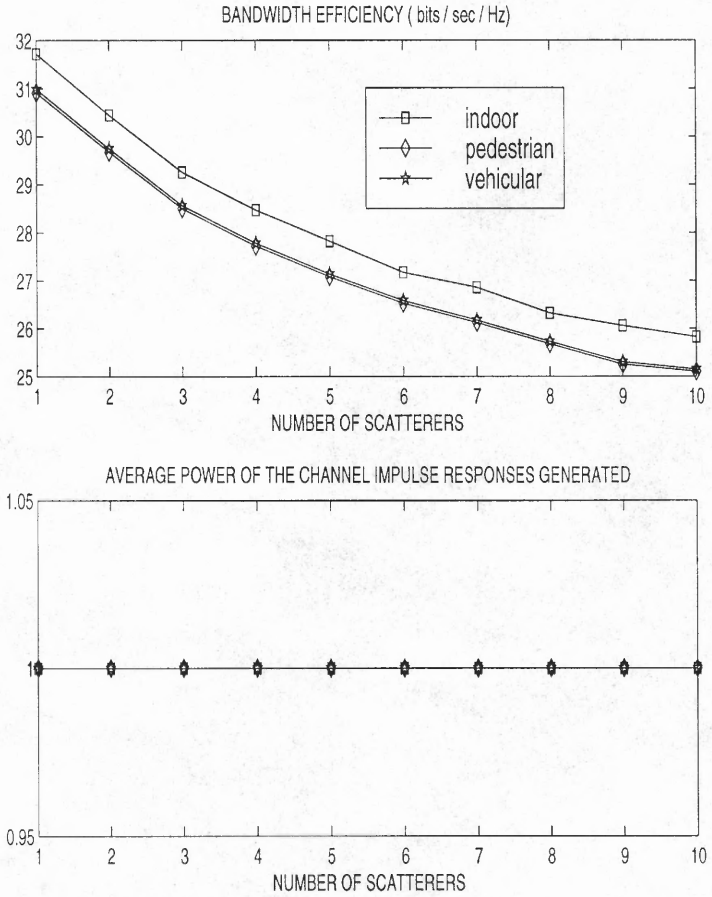

Figure 4.2 a. Bandwidth efficiency (bits/sec/Hz) vs. number of scatterers, vehicular scenario, b. Average power of the channel impulse responses generated.

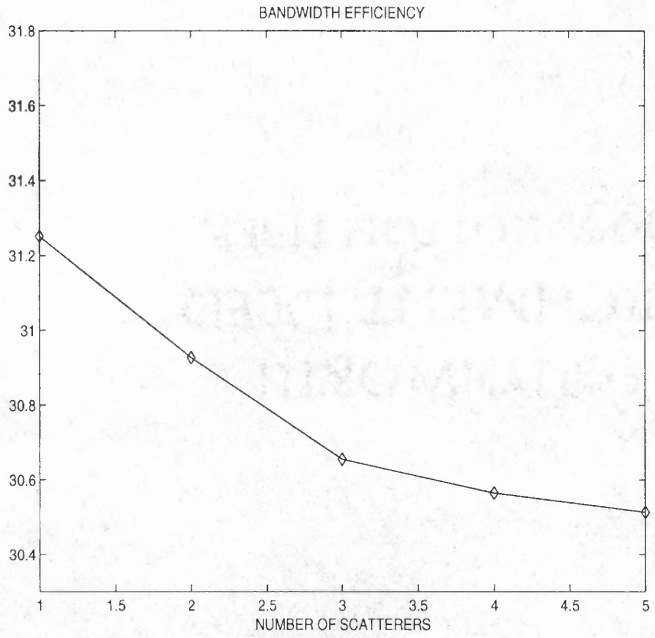

Figure 4.3 Bandwidth efficiency (bits/sec/Hz) vs. number of scatterers, magnitudes and arrival times of 5 scatterers from ETSI model in a vehicular scenario are considered.

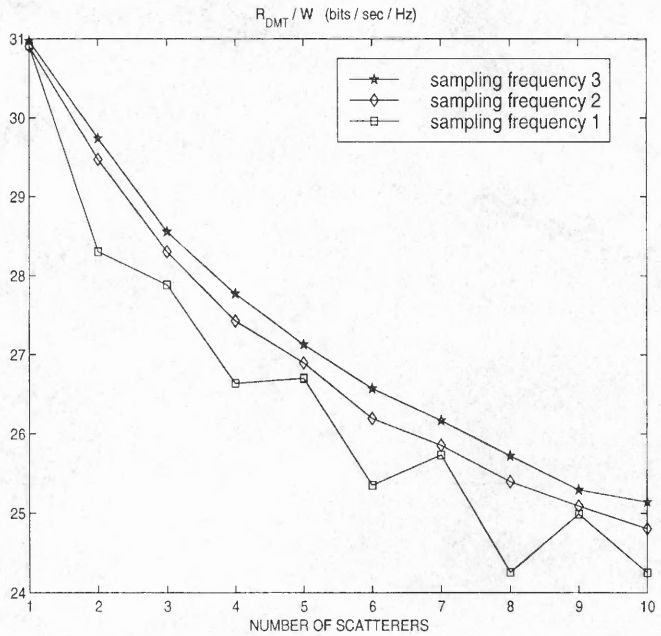

Figure 4.4 Bandwidth efficiency (bits/sec/Hz) vs. number of scatterers, vehicular scenario, 3 different sampling frequencies.

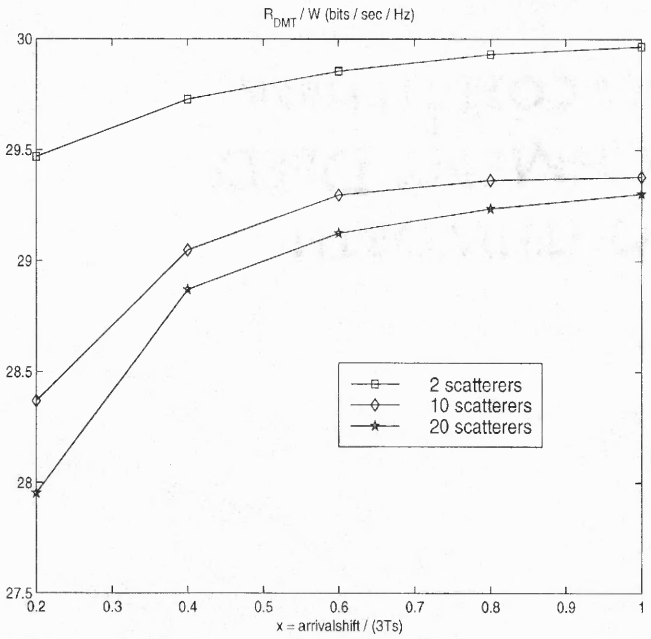

Figure 4.5 Bandwidth efficiency (bits/sec/Hz) vs. standard deviation of the path delay shifts, 10 unit magnitude scatterers are shifted from their uniformly distributed delays with increasing deviation on time delay axis with constant maximum excess delay $= 3.31\mu s$.

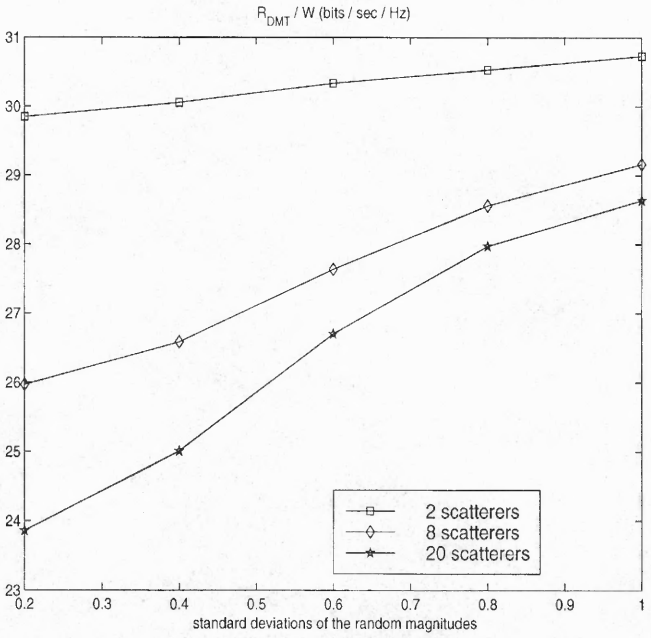

Figure 4.6 Bandwidth efficiency (bits/sec/Hz) vs. standard deviation of the scatterer magnitudes. 10 scatterers have random magnitudes distributed uniformly on path delay axis with maximum excess delay $= 3.31\mu s$. x-axis shows the standard deviation of the magnitude random variables $N(1, x)$.

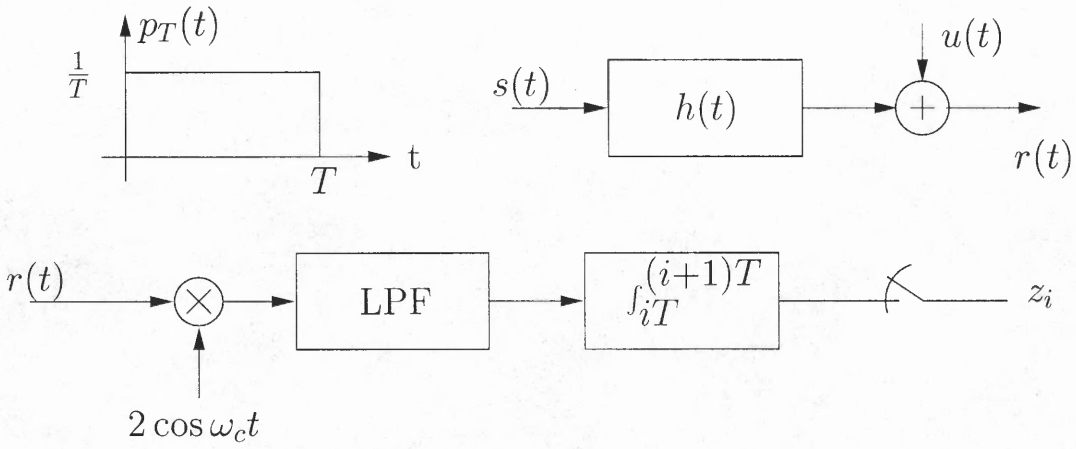

Figure 4.7 Single carrier BPSK receiver structure (matched filter, correlator receiver).

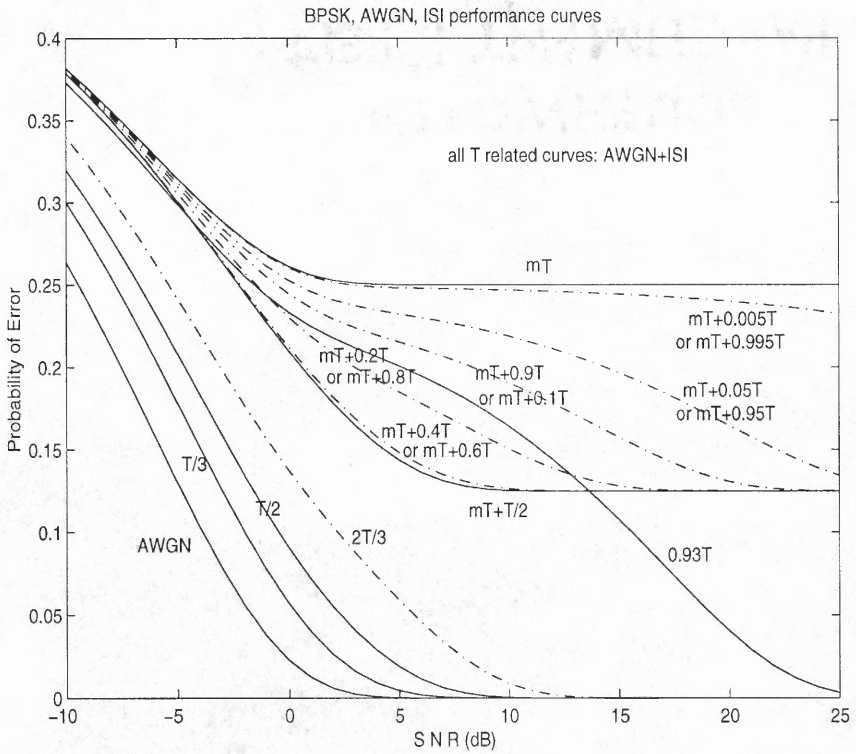

Figure 4.8 Performance analysis of single carrier receiver.

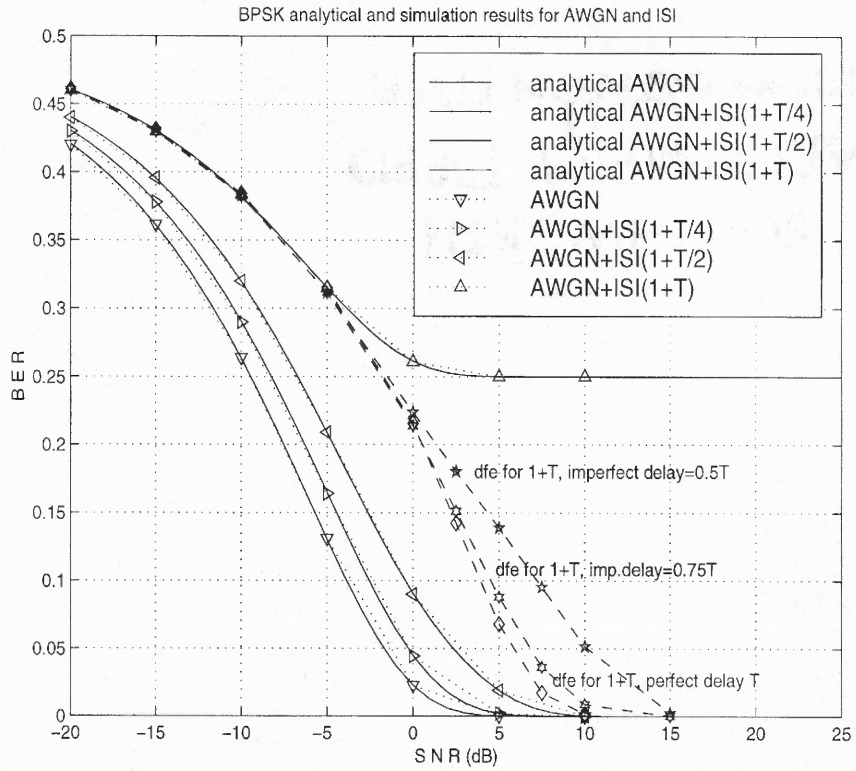

Figure 4.9 Performance simulations of single carrier receiver with and without DFE.

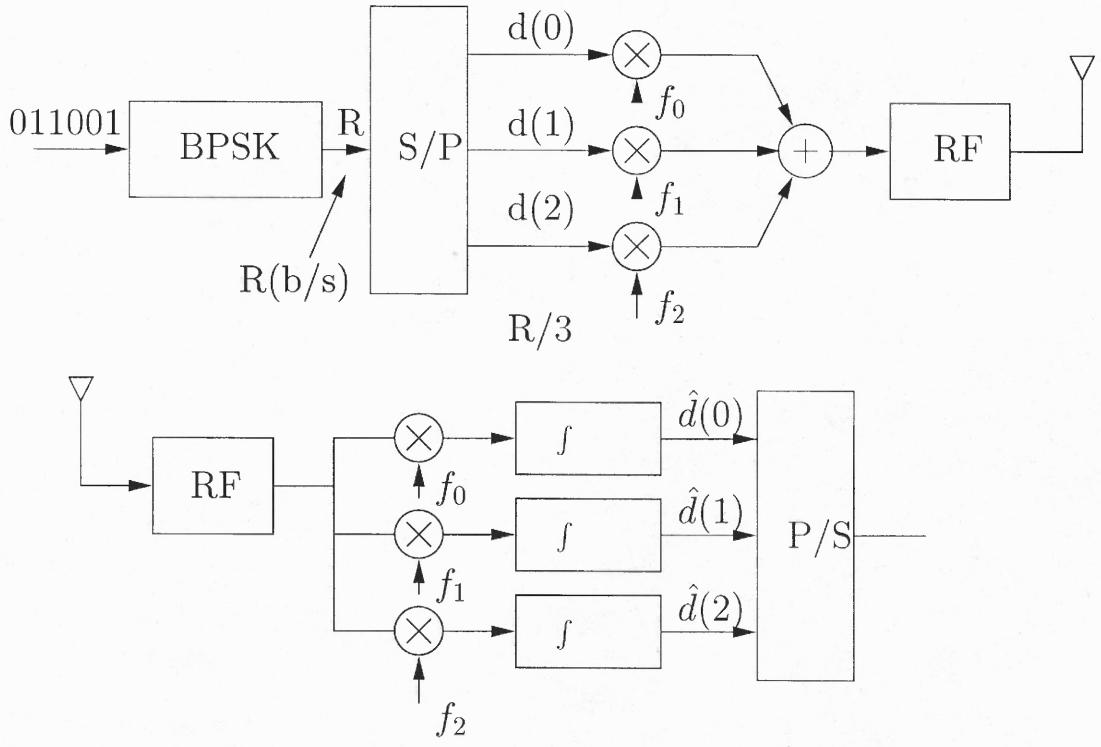

Figure 4.10 Multicarrier system transmitter and receiver structures.

CHAPTER 5

DOWNLINKS WITH DIFFERENT INTERBLOCK DATA RATES

So far we considered energy as the major resource in the propagation channel and we analyzed ways of using it with irregular subbands and equal bin multicarrier systems. In this chapter, starting with spreading and diversity methods, we consider CDMA downlink structures and we perform simulations with several configurations to achieve trade-off strategies among transmission parameters.

5.1 DS-CDMA and MC-CDMA Systems with Diversity Combining

This section includes descriptions of the spread spectrum and multicarrier CDMA as they are the chosen application for multicarrier and adaptive loading. Using separate carriers also allows overlaying additional user data on existing IS-95 downlink system.

5.1.1 Spread Spectrum Notion and CDMA

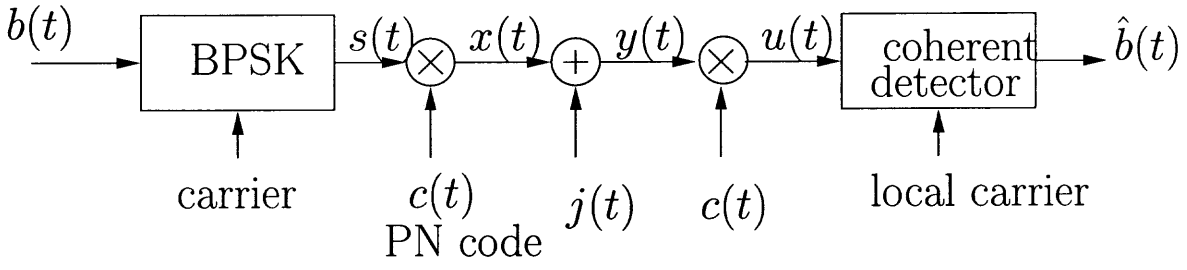

Figure 5.1 Direct sequence code division multiple access BPSK communication scheme

Protection against externally generated interfering signals (or in case of CDMA other users appear as interference) is provided by spreading the information bearing signal into a wideband [21, 20]. The spreading is done by multiplication in time

domain. As a simple illustration a direct-sequence spread BPSK system is considered as in Figure 5.1. The binary data sequence $b(t)$ is first turned into non-return-to-zero polarity and modulated with a carrier frequency giving $s(t)$. After spreading this signal we have

$$x(t) = c(t)s(t) = \pm\sqrt{\frac{2E_b}{T_b}}c(t)\cos 2\pi f_c t. \tag{5.1}$$

The spreading code consists of N chips and we can express $x(t)$ as

$$x(t) = \pm\sqrt{\frac{E_b}{N}}\sum_{k=0}^{N-1} c_k\phi_k(t), \tag{5.2}$$

where the symbol period is $T_b = NT_c$ and $\phi_k(t) = \sqrt{\frac{2}{T_c}}\cos(2\pi f_c t)$ $(kT_c \leq t \leq (k+1)T_c)$ in the inphase basis function. On quadrature axis we have $\tilde{\phi}_k(t) = \sqrt{\frac{2}{T_c}}\sin(2\pi f_c t)$ $(kT_c \leq t \leq (k+1)T_c)$ as basis function which is orthogonal to $\phi_k(t)$. Information bearing signal stays on inphase axis in BPSK but interference is on quadrature axis too,

$$j(t) = \sum_{k=0}^{N-1} j_k\phi_k(t) + \sum_{k=0}^{N-1} \tilde{j}_k\tilde{\phi}_k(t), \quad 0 \leq t \leq T_b, \tag{5.3}$$

where $j_k = \int_0^{T_b} n(t)\phi_k(t)dt$, $\tilde{j}_k = \int_0^{T_b} n(t)\tilde{\phi}_k(t)dt$, $k = 0, 1, \ldots, N-1$. Total interference power is $J = \frac{1}{T_b}\int_0^{T_b} j^2(t)dt = \frac{2}{T_b}\sum_{k=0}^{N-1} j_k^2$, assuming interference is divided equally in inphase and quadrature domains.

Receiver removes the code from received signal and this operation spreads the interference while the data signal is being despreaded. The coherent detector output can be expressed as

$$V = \sqrt{\frac{2}{T_b}}\int_0^{T_b}(x(t)+j(t))c(t)\cos(2\pi f_c t)dt = V_s + V_{cj} = \pm\sqrt{E_b} + \sqrt{\frac{T_c}{T_b}}\sum_{k=0}^{N-1} C_k j_k \tag{5.4}$$

where $E[C_k j_k | j_k] = \frac{1}{2}j_k - \frac{1}{2}j_k = 0$ and $var[V_{cj}|j] = \frac{1}{N}\sum_{k=0}^{N-1} j_k^2 = \frac{T_b J}{2N} = \frac{JT_c}{2}$. Processing gain relates the input SNR to output SNR and given as $PG = \frac{T_b}{T_c} = N$. The decision variable is $V = \pm\sqrt{E_b} + V_c j$. At high processing gains V_{cj} can be taken

as a Gaussian rv (central limit theorem) and probability of error can be found as

$$P_r(e) = P[V_{cj} > \sqrt{E_b}] = Q(\sqrt{\frac{2E_b}{JT_c}}) \tag{5.5}$$

for the given direct-sequence spread BPSK system.

5.1.2 Multicarrier CDMA

Multicarrier code division multiple access (MC-CDMA) is introduced as an intentional dispersive signaling over different subcarriers. This scheme uses direct-sequence CDMA for multiplexing but modulation on carriers is done by OFDM principle [22, 23]. In this section, generation of BPSK MC-CDMA signaling will be covered. Corresponding analytical expressions will be overviewed to provide a standpoint on ideas of MC-CDMA related future work proposed in the last section.

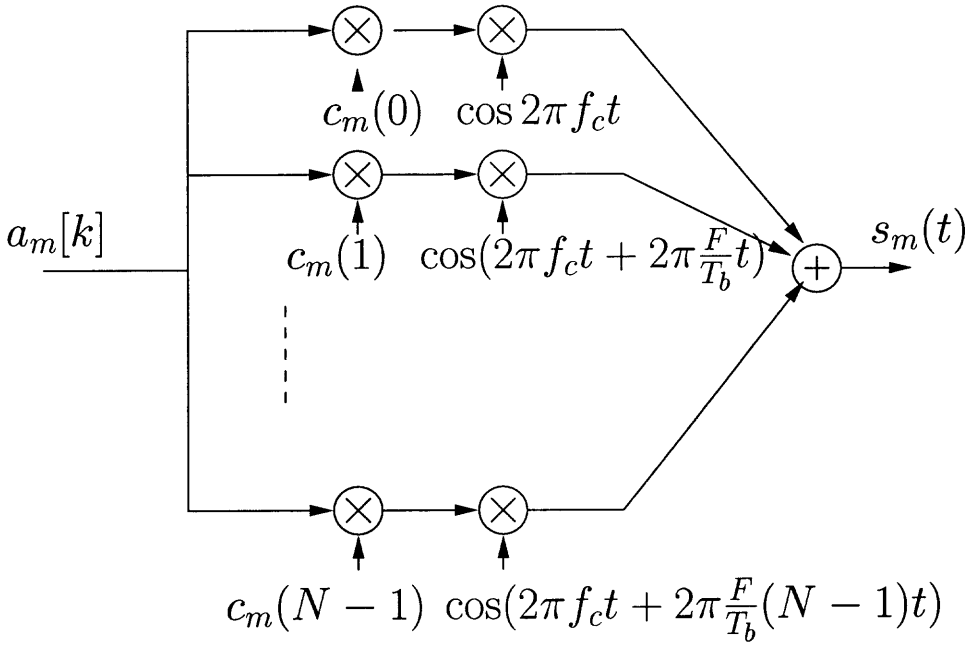

Figure 5.2 Multicarrier CDMA BPSK transmitter

As in Figure 5.2, a single data symbol is copied into N parallel branches. At each branch, data bits are multiplied by one chip of a spreading code of length N and then BPSK modulated to a subcarrier spaced by $\frac{F}{T_b}$ ($F = 1$ corresponds to OFDM). Transmitted signal can be written as

$$s_m(t) = \sum_{i=0}^{N-1} c_m[i] a_m[k] \cos(2\pi f_c t + 2\pi i \frac{F}{T_b} t) p_{T_b}(t - kT_b) \tag{5.6}$$

corresponding to k^{th} data bit of m^{th} user, $c_m[i] \in \{-1, 1\}$ and $p_{T_b}(t)$ is unit amplitude in $[0, T_b]$ and elsewhere. Input data $a_m[k]$ is assumed to be in polar form $\{\pm 1\}$.

Bandwidth of the transmitted signal is $\frac{F}{T_b}$ as seen from Equation (24). Coherence bandwidth, BW_c, is in the order of $1/T_d$, T_d is the excess delay of the channel. As $\frac{F}{T_b} \gg BW_c$ channel is frequency selective causing ISI.

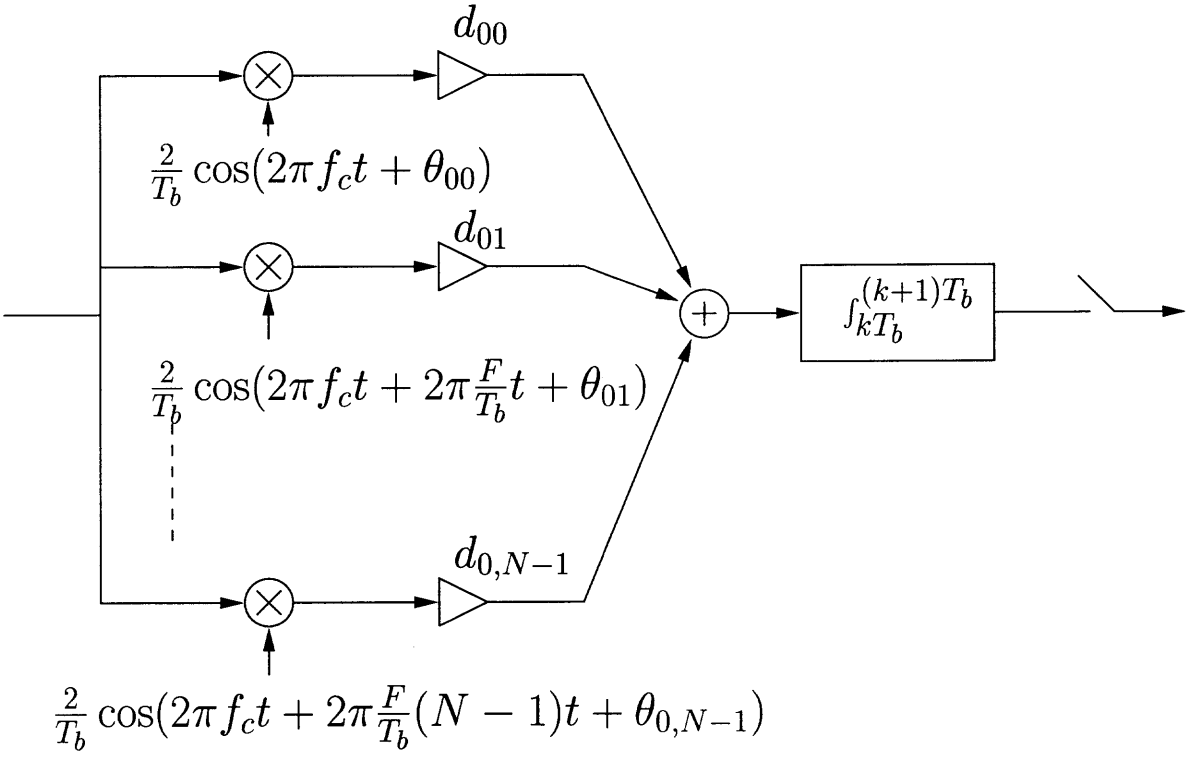

Figure 5.3 Multicarrier CDMA BPSK receiver

In uplink, base station receives signals from different users and frequencies, so channel can be expressed as $H_m(f_c + i\frac{F}{T_b}) = \rho_{mi} e^{j\theta_{mi}}$. These channel parameters have

to be estimated and used for prefered combining or equalizing purposes as will be clear in upcoming receiver description.

In downlink, a mobile terminal receives different interfering user signals $m = 1, \ldots, M-1$ over the same channel with the wanted signal $m = 0$, $\rho_{mi} = \rho_{0i}$, $\theta_{mi} = \theta_{0i}$. Receiver collects signals from M transmitters with any preferred combining method.

The receiver structure is shown in Figure 5.3. The input at the receiver can be expressed as a sum of M user signals from M active transmitters

$$r(t) = \sum_{m=0}^{M-1} \sum_{i=0}^{N-1} \rho_{mi} c_m[i] a_m[k] \cos(2\pi f_c t + 2\pi f_c \frac{F}{T_b} t + \theta_{mi}) + n(t) \tag{5.7}$$

for k^{th} data bit. AWGN is shown as $n(t)$. Local mean power of i^{th} subcarrier of m^{th} user can be found as $\bar{p_{mi}} = \frac{1}{2} E[\rho_{mi}^2]$. Since the N branches carry iid variables, local mean power of m^{th} user is $\bar{p}_m = N\bar{p}_{mi}$. The decision variable of the k^{th} bit is

$$v_0 = \textstyle\sum_{m=0}^{M-1} \sum_{i=0}^{N-1} \rho_{mi} c_m[i] d_{0i} a_m[k]$$
$$\times \frac{2}{T_b} \int_{kT_b}^{(k+1)T_b} \cos(2\pi f_c t + 2\pi i \frac{F}{T_b} t + \theta_{mi}) \cos(2\pi f_c t + 2\pi i \frac{F}{T_b} t + \theta_{0i}) dt + \eta, \tag{5.8}$$

for $m = 0$ desired user.

Different diversity combining methods [16, 22, 23] are possible to choose from. In equal gain combining (EGC), the gain is $d_{0i} = c_0[i]$ and the decision variable is $v_0 = a_0[k] \sum_{i=0}^{N-1} \rho_{0i} + \beta_{int} + \eta$. In maximum ratio combining (MRC), the gain is $d_{0i} = c_{0i}\rho_{0i}$ and decision variable can be found as $v_0 = a_0[k] \sum_{i=0}^{N-1} \rho_{0i}^2 + \beta'_{int} + \eta$. Corresponding probability of error expressions can be found using the decision variables. MRC combats the AWGN component better than EGC does when there is no multiuser interference. Combating interference and noise appear as goals opposing each other. EGC maintains orthogonality between the users when the number of users is high and performs better than EGC in this region. Using threshold power levels orthogonality can be maintained in a controlled equalization (CE). CE outperforms both EGC and MRC for most number of user cases. This discussion is valid for downlink where the mobile terminals receive. In uplink, since base station collects signals from all

users in different frequencies, $H_m(f_c + i\frac{F}{T_b}) = \rho_{mi}e^{j\theta_{mi}}$ orthogonality of the codes are invalidated. The receiver can only combat AWGN and MRC outperforms EGC.

5.2 Downlinks with Different Interblock Data Rates

Significant improvements are expected for third generation (3G) cellular systems over their second generation ancestors. A wide variety of quality of service requirements await the 3G standardization in North America for IS-95 wideband CDMA system [24].

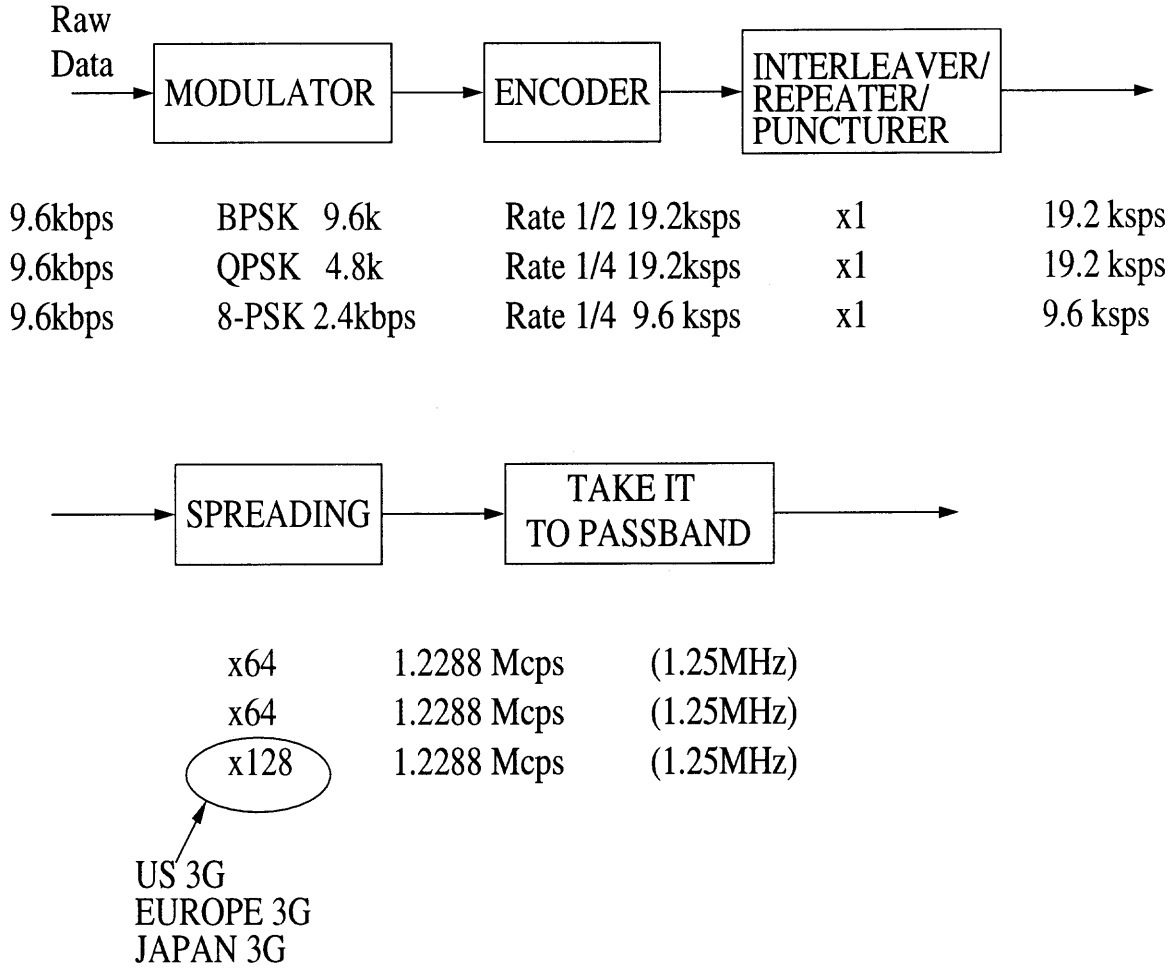

Figure 5.4 3G wireless communication system or physical layer radio interface

ITU forces 3G systems to accomplish reliable communication (both circuit and packet switched) between multiple networks in high speed. Highly asymmetric but secure channels have to be provided placing new requirements on radio interface system. As shown in Figure 5.4, various elements of the wireless communication system such as modulator, encoder, interleaver/repeater/puncturer, spreading provide variable parameters of bandwidth, transmission quality, and delay with negotiated, mixed, matched requirements of the mobile service on a time-varying wireless channel.

It is possible to reach high transmission rates with various trade-offs: Raw input data can be modulated adaptively (Figure 5.4, modulator). With realizable feedback to transmitter, using either optimal power rate adaptation or constant power with rate adaptation, capacity of adaptive modulation in conjunction with diversity combining can be derived [25] for certain conditions. Encoding can be done with variable rates as in the 3G European GSM evolution path, EDGE. Interleaver/repeater/puncturer is followed by the chosen spreading. The main variables to design the satisfactory radio interface are

- Allocated power per subcarrier per user
- Spreading gain per subcarrier per user
- Transmission rate per subcarrier (with the corresponding modulation, convolutional coding /interleaving rate and spreading gain).

All these variables can be set jointly for each active user to maximize the total throughput of the system. As a new user is added to the radio network, its modulation, coding and spreading parameters will have to be set according to the current channel fading conditions and the adaptive loading and noise levels of the multicarriers all the while making sure the required probability of error is maintained with the lowest possible transmission power allocated to the user. The optimization

algorithm may have to arrange the powers allocated for each subcarrier for each user jointly rather than just the new user alone to reach the goal of maximum system throughput. That is, adaptation of the above mentioned parameters for each of the active users may be necessary everytime a new user becomes active or an active user becomes dormant.

5.2.1 Comparison of Different Interblock Data Rate Downlinks

Different QoS and data rate requirements of communication channels can be satisfied by varying one or more of the coding, digital modulation and spreading blocks. Keeping transmission bandwidth fixed as in IS-95, four different interblock data rate configurations are compared. User powers are kept constant in the performance simulations. Various coding, modulation and spreading rate combinations yield different performance characteristics in AWGN, flat fading and multipath environments permitting trade-off decisions on choices of rate, QoS, and implementation.

5.2.2 Provision of a Multitude of Services for 3G

Third generation wireless systems will enable provision of a multitude of services each with potentially different QoS and data rate requirements. Given a fixed transmission bandwidth, operating on one multicarrier frequency, one basic method to implement a variable rate service in the downlink physical layer DS-CDMA system is to have variable spreading factors [24]. This could be accomodated with variable coding and modulation rates which are shown [36] to provide different performance characteristics in additive white Gaussian noise, flat and frequency selective fading mobile environments.

A brief overview of the simulated downlink physical layer system is given in the next section. The following section describes the simulation details. Perfor-

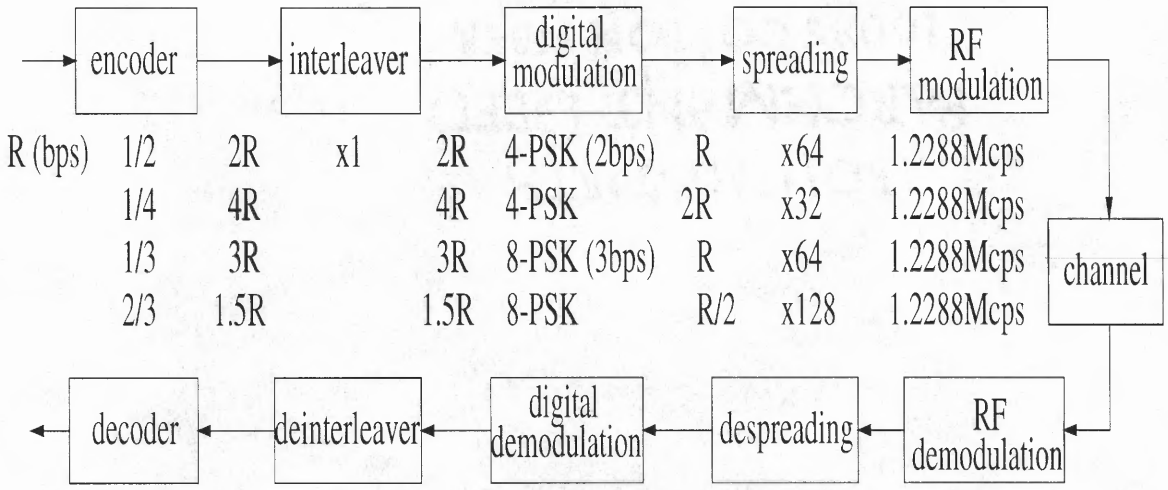

Figure 5.5 Block diagram of downlink physical layer radio interface with variable data rates.

mances of the different rate configurations are compared and trade-off on transmission parameters is discussed.

5.2.3 DS-CDMA Downlink System Description

Users' transmitted signals travel through the same channel. Receiver of each user receives the superposition of all intended user data sequences from the base station. Therefore, the downlink physical layer is synchronous. Transmission powers of the active users are kept equal. This corresponds to perfect power control as the solution to near-far problem. Coding, interleaving, digital modulation and spreading are the blocks of the downlink system as shown in Figure 5.5.

A convolutional encoder generates n encoded bits for each k information bits and k/n is called the coding rate [35]. The shift register consists of n linear algebraic function generators and K stages. Number of stages, K is the constraint length of the

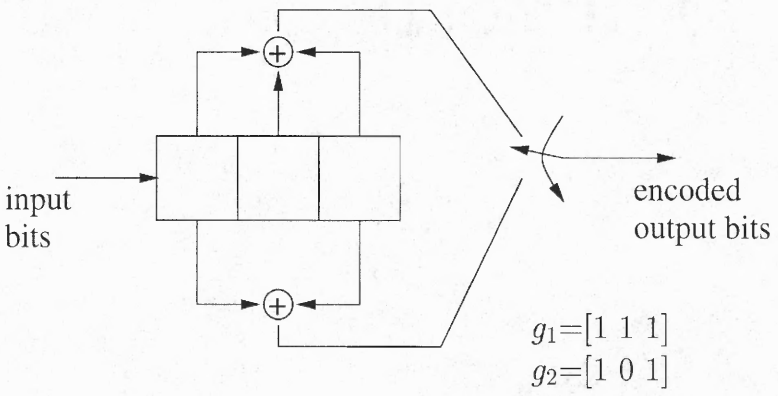

Figure 5.6 Shift register for convolutional coding with rate 1/2, K=3.

convolutional code. Figure 5.6 shows the shift register, structure of a convolutional coder with rate 1/2 and $K = 3$. The generator polynomials [1 1 1] and [1 0 1] show the stages of the bits to be modulo-2 added in order to obtain the redundant bits. Generating polynomials are in general shown in octal form, this corresponds to [7,5] in the example of Figure 5.6.

Two sets of realizations are considered for the encoding block. In the first set, for 1/2, 1/4, and 1/3 rate coders, different generating polynomials are chosen. This requires different coder/decoder structures in the transmitter and receiver. The generator polynomials are [7,5], [4,5,7], [23,35,27,33] for 1/2, 1/3, and 1/4, respectively. The 2/3 code is generated from 1/2 rate code by puncturing every other bit in the second output stream of 1/2 coder as in [32, 33, 34]. This corresponds to three code-word bits for every two information bits. The receiver inserts erasures at the points where bits have been punctured. This allows the same Viterbi decoder usage with additional erasure insertion only which greatly simplifies the decoder block in the receiver. The second realization or implementation set considered in the simulations include the rate-compatible convolutional codes which is based on a

family of punctured convolutional codes. The code-word bits from the higher-rate codes are embedded in the lower-rate codes. Rate-compatible punctured convolutional (RCPC) codes allow implementing a variable-rate error control system using a single code in the transmitter and a single decoder in the receiver.

The random data bits of users are first convolutionally encoded. Following the encoding block, interleaving is performed. Interleaving is used to obtain time diversity against the deep fades of the wireless channel. This method of scrambling the information bits before transmission prevents to use of overhead [29]. In case of a noise burst or deep fade in the channel, block of source data is not corrupted at the same time because it is distributed in time. In other words, the design of the interleaver is done such that the duration of the deep fade is shorter than the interleaving seperation. In our simulations, approximately 20ms interleaving seperation between subsequent bits are used as in IS-95. However, this causes a delay in the receiver that the deinterleaver has to wait until scramble period is filled with received bits. Only then the deinterleaver can descramble and reform the intended sequence of the data bits. As the result of the fading channel and the interleaver, the erronous bits are distributed evenly in the stream and this enhances the performance of the decoder.

Digital modulation is carried out by fixed 4-PSK and 8-PSK. Gray encoding is present among the subsequent nodes in the constellations. Complex symbols of the digital modulation are seperated into the inphase and quadrature components displayed as in Figure 5.7. On the inphase and quadrature branches, user specific orthogonal Walsh codes are used to spread the real user data symbols with the gains as shown in Figure 5.7. These spreading gains maintain the fixed transmission bandwidth of 1.2288 Mcps (IS-95). Figure 5.8 shows the channel and transmission symbol durations at the same chip rate for all multirate configurations as used in the simulations. This corresponds to fixed transmission bandwidth. So that these configurations can be used simultaneously in the downlink. Depending on the performance

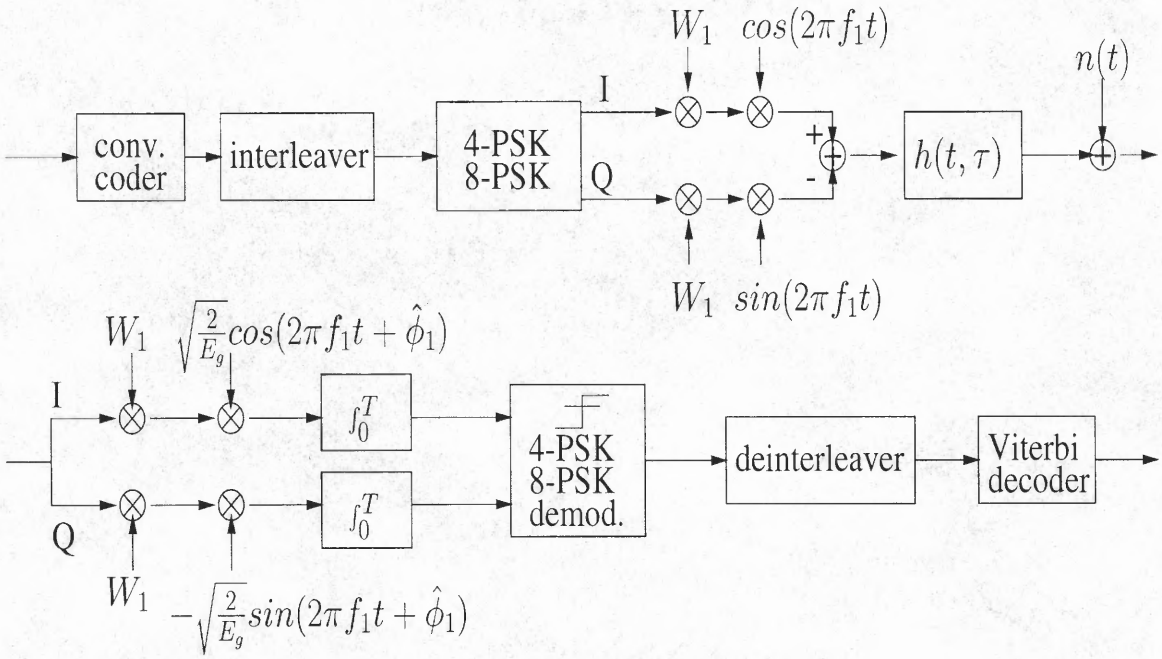

Figure 5.7 Synchronous downlink transmitter and receiver diagram used for single user AWGN and flat fading performance simulations.

of each configuration, one can prefer assigning one of the configurations to an active user.

RF modulation is done at 2 Ghz in which the wireless channel is simulated. For the time being, additive white gaussian noise and flat fading channels with a single RAKE finger at the receiver are considered. Fading channel is assumed to stay unchanged for one data bit period as shown in Figure 5.8. Simulations with multipath channel will be explained after AWGN and flat fading performances.

The receiver demodulates the received signal at RF frequency. Orthogonal despreading is done on real symbols at both inphase and quadrature components. M-PSK demodulation converts the complex information symbols into bits. Viterbi decoder decodes the deinterleaved bit stream.

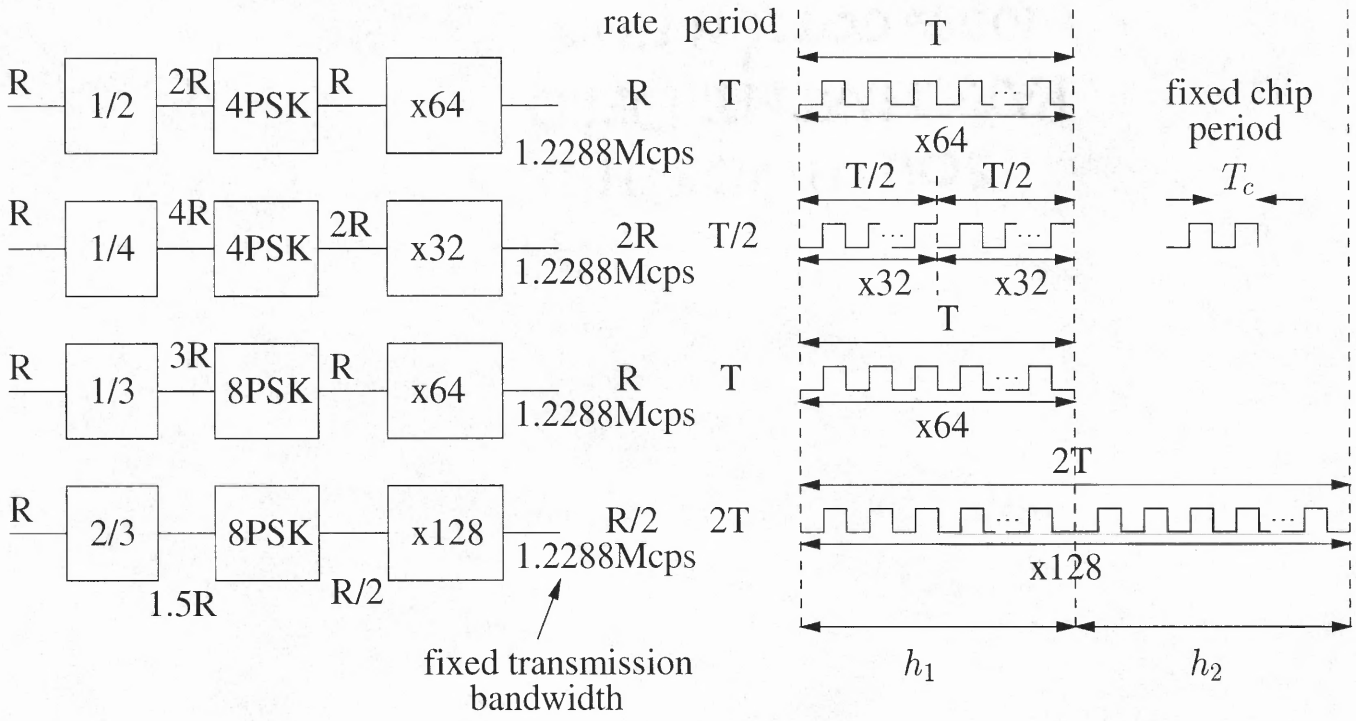

Figure 5.8 Same chip period and fixed transmission bandwidth in all multirate configurations.

5.2.4 System Performance Simulations and Discussions

To observe the bit error rates or quality of services one can achieve, two sets of simulations are performed. In the first set of simulations, for 1/2, 1/4, and 1/3 rate coders, different generating polynomials are chosen. This requires different coder/decoder structures in the transmitter and receiver. The generator polynomials are [7, 5], [4, 5, 7], [23, 35, 27, 33] for 1/2, 1/3, and 1/4, respectively. The 2/3 rate code is generated from 1/2 rate code by puncturing every other bit in the second output stream of 1/2 coder.

The same rates can be achieved by using the rate-compatible punctured convolutional (RCPC) codes. This is the way the codes are achieved in the second

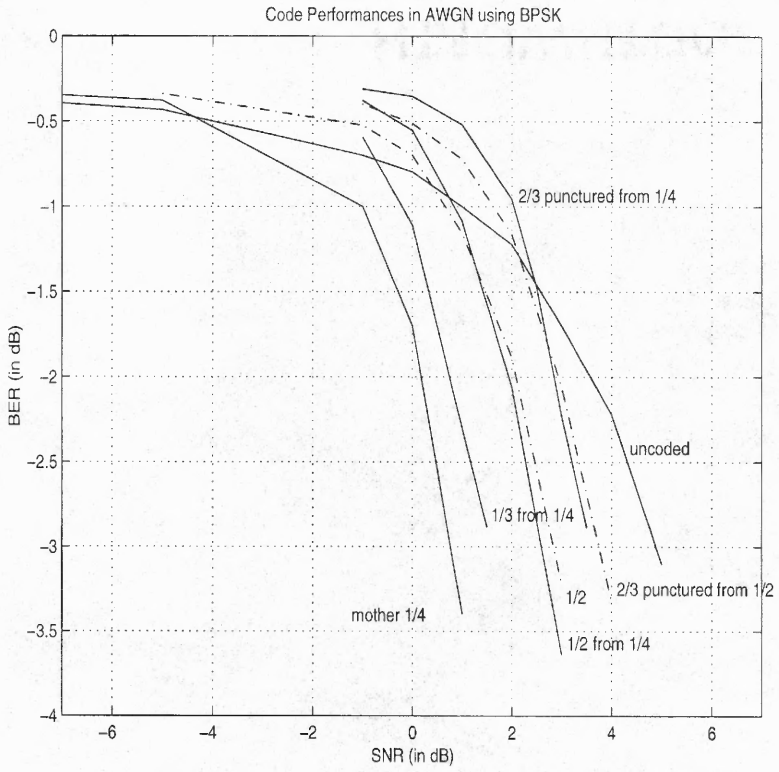

Figure 5.9 Code performances for BPSK in additive white gaussian noise.

simulation set. Mother 1/4 rate code [23, 35, 27, 33] is punctured to obtain the remaining three codes with the puncturing matrices in [34]. These puncturing matrices are shown in Table 5.1. This allows the usage of the same coder/decoder structure with an addition of a puncturing/depuncturing operation. The ones in the matrices show the code-word bits that are transmitted and the zeros show the deleted or punctured code-word bits of the convolutional shift register output. All

Table 5.1 Puncturing matrices used for 1/2, 1/3, 2/3 from the 1/4 mother code.

Rate	2/3	1/2	1/3	1/4
Puncturing Matrices	1111 1111	1111 1111	1111 1111	1111 1111
	1010 1010	1111 1111	1111 1111	1111 1111
	0000 0000	0000 0000	1111 1111	1111 1111
	0000 0000	0000 0000	0000 0000	1111 1111

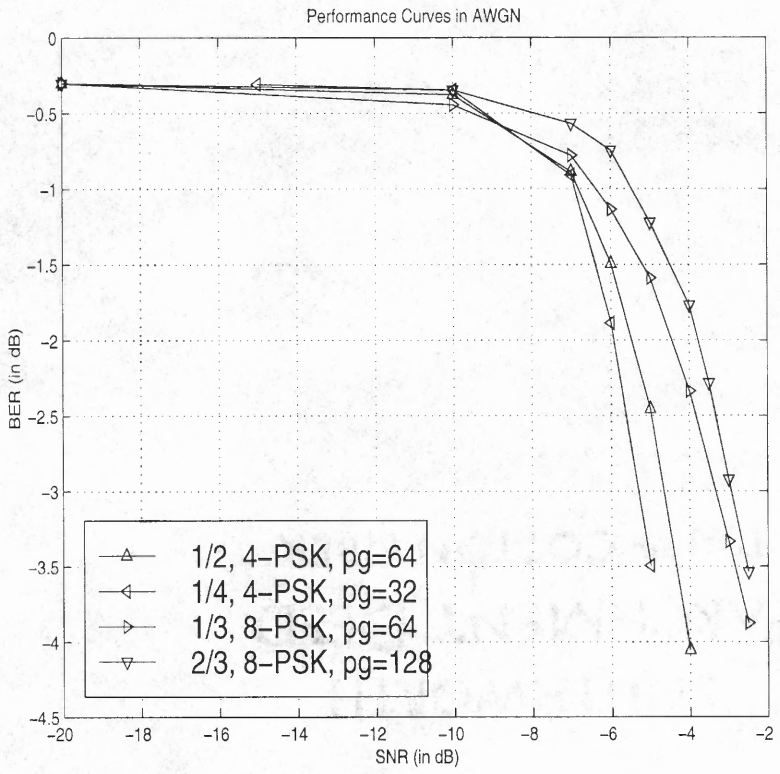

Figure 5.10 Performance characteristics in additive white gaussian noise when different generator polynomials and different coder/decoder structures are used.

the code-word bits of the 1/4 rate are transmitted. In the receiver, in the place of the punctured code-word bits, erasures are inserted. Note that only the 1/4 rate mother-code decoder are used. Erasures are ignored in the calculation of the trellis metrics in Viterbi decoder [20, 34, 32, 33] since there are no code-word bits transmitted at their erased slots. The performances of all the codes mentioned operating on BPSK modulated bits in additive white Gaussian noise are plotted in Figure 5.9.

The performance simulations using the first set of codes are displayed in Figures 5.10 and 5.11. For the four different rates, digital modulation and spreading blocks change the data rates among the blocks as shown in Figure 5.5. Before transmission, the fixed 1.2288 Mcps transmission chip rate is maintained. During

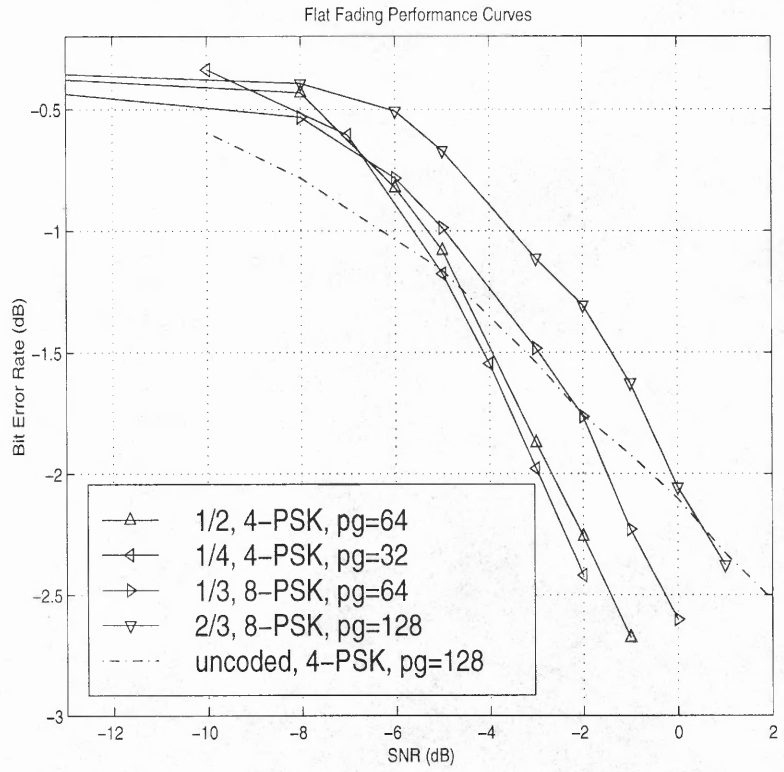

Figure 5.11 Performance characteristics in flat fading when different generator polynomials and different coder/decoder structures are used.

the channel simulation, the chip duration is kept constant and the fading channel is assumed to stay unchanged during 64 chips as shown in Figure 5.8. This assumption is valid in the other rate configurations as well for a fair comparison. Signal to noise ratio is measured before all the receiver blocks. Thus, in the performance curves, coding and spreading gains are seen all together.

In the second set, rate compatible punctured convolutional (RCPC) codes are used. This changed the results slightly as can be seen in Figures 5.12 and 5.13. 1/4 rate coder helps the system outperform the other rate configured systems. For the chosen spreading gains, modulation sizes and code rates, the coding block seems to be the dominating factor in the overall performance of AWGN and flat fading

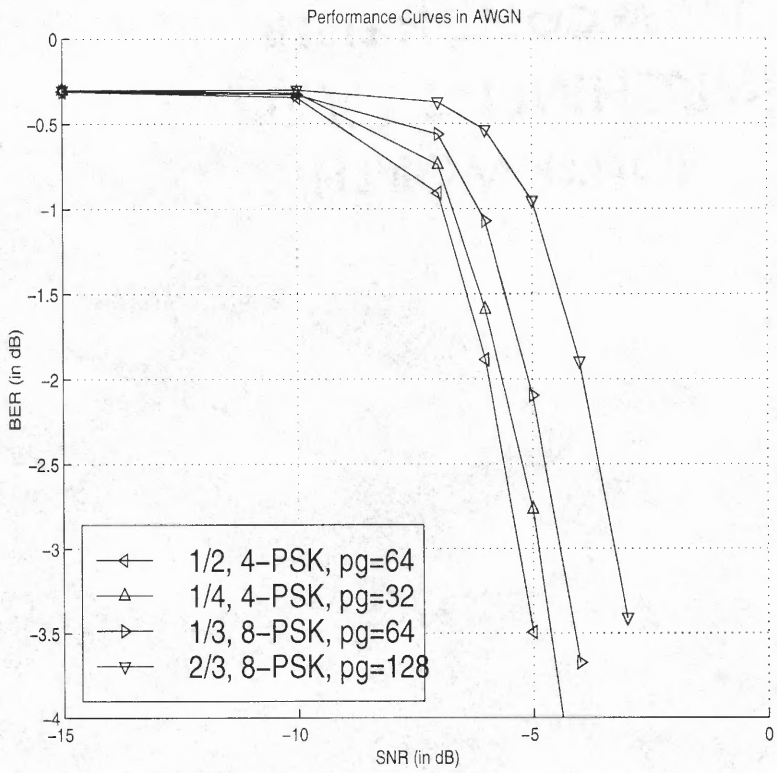

Figure 5.12 Performance characteristics in AWGN when the same coder/decoder structure (with RCPC codes) is used to generate higher rate codes by puncturing.

channels. Less than 0.25 dB difference in bit error rate at SNR = - 2 dB in the performance of the first three configurations is observed under flat fading channel. In AWGN channel this difference is more pronounced.

In AWGN and flat fading channel performances, we see the perfect user seperation with orthogonal Walsh codes. Thus the results demonstrate only one active user performance.

In multipath environment, a two path fading channel is simulated. In all simulations, Rayleigh fading coefficients are Doppler shaped [16], assuming a 70

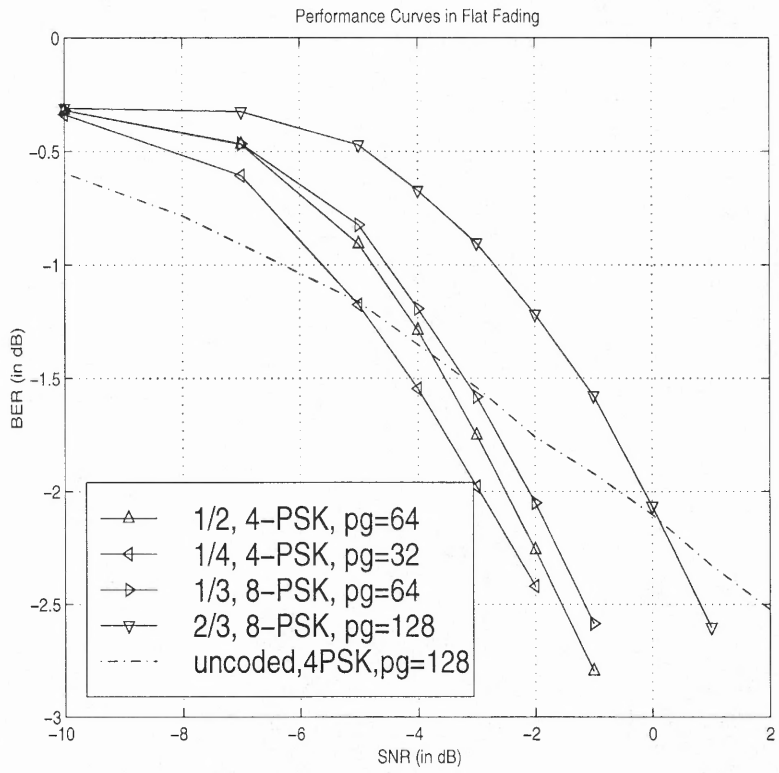

Figure 5.13 Performance characteristics in flat fading when the same coder/decoder structure (with RCPC codes) is used to generate higher rate codes by puncturing.

mph maximum velocity in the time-varying mobile wireless channel as explained in detail in Chapter 2.

In the multipath fading (frequency selective) case, in addition to user specific Walsh codes, receiver also makes use of a user specific long PN code which is $2^{42} - 1$ chip long [29]. Direct spreading is used in each downlink configuration. Each user is assigned a unique long PN code. The long code is generated using the characteristic polynomial

$$g(x) = x^{42} + x^{35} + x^{31} + x^{27} + x^{26} + x^{25} + x^{22} + x^{21} + x^{19} + x^{18} + x^{17}$$
$$+x^{16} + x^{10} + x^{7} + x^{6} + x^{5} + x^{3} + x^{2} + x^{1} + 1.$$

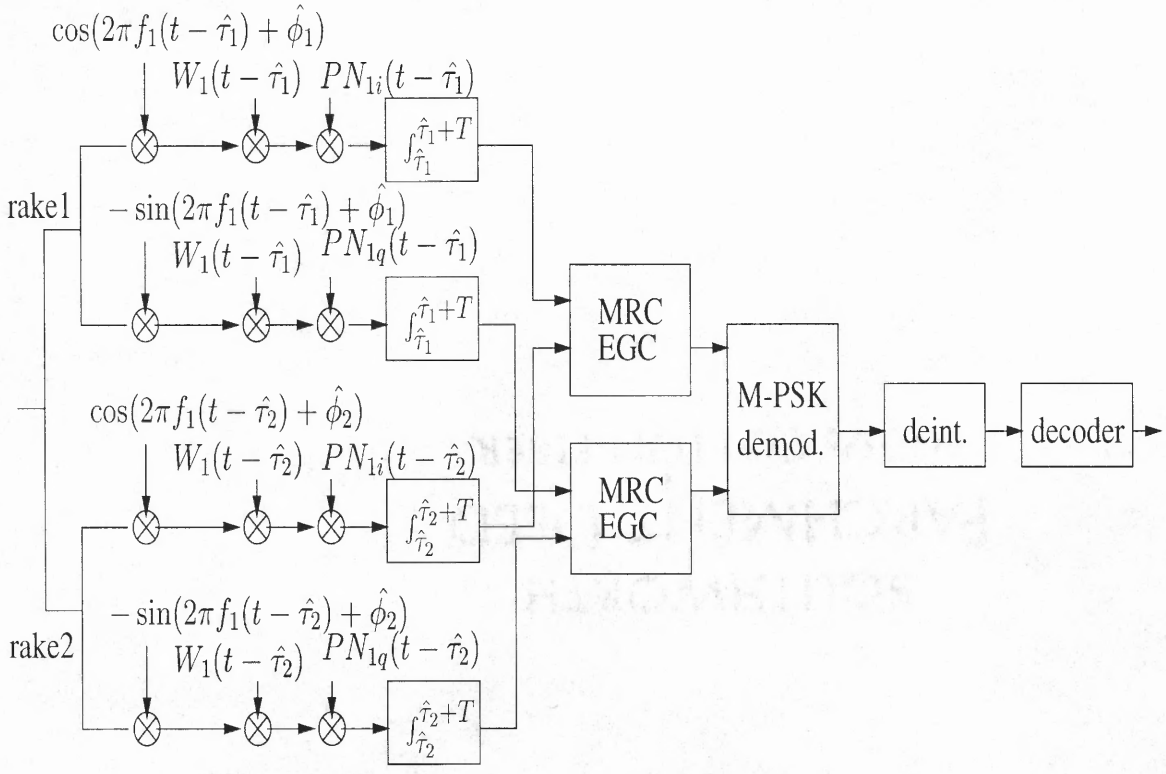

Figure 5.14 Downlink receiver diagram of user1 with two RAKE fingers for two-multipath fading performance simulations when there are more than one active user.

In addition to the long PN code uniquely assigned, each user also has orthogonal seperation maintained by Walsh codes. The receiver structure with seperate RAKE fingers is shown in Figure 5.14. Maximum ratio and equal gain combining methods are used to combine the RAKE contributions coming from different multipaths. Perfect channel parameter estimation is assumed.

Complex spreading shown in Figure 5.15 is also tested and observed to perform the same as the direct spreading as expected.

Figure 5.16 shows the performance when there are two active users operating in the system with an additional multipath at approximately 2 ms of excess delay in the fading wireless channel. The curves show equal gain combining and maximum

ratio combining diversity results operating on the two seperate RAKE receivers locked on the uncorrelated multipaths at the mobile receiver. Figure 5.17 shows the performance characteristics when soft decision is used in the decoder for the fourth rate configuration.

Figure 5.18 shows the effect of the number of active users in the system on the bit error rate. All users operate at the same transmission power at SNR = -4dB. From these curves, we see the same performance behaviors among the given rate configurations as in AWGN and flat fading performance simulations. Rather than the fixed modulation sizes (no adaptive modulation considered) or the various spreading gains, the coding rate proves to be the dominating parameter in the system observing the performance curves obtained.

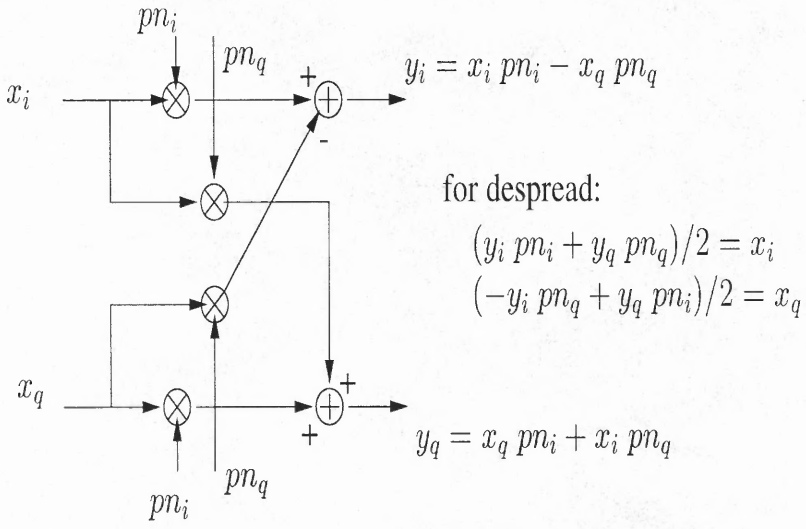

Figure 5.15 Complex spreading for inphase and quadrature channels.

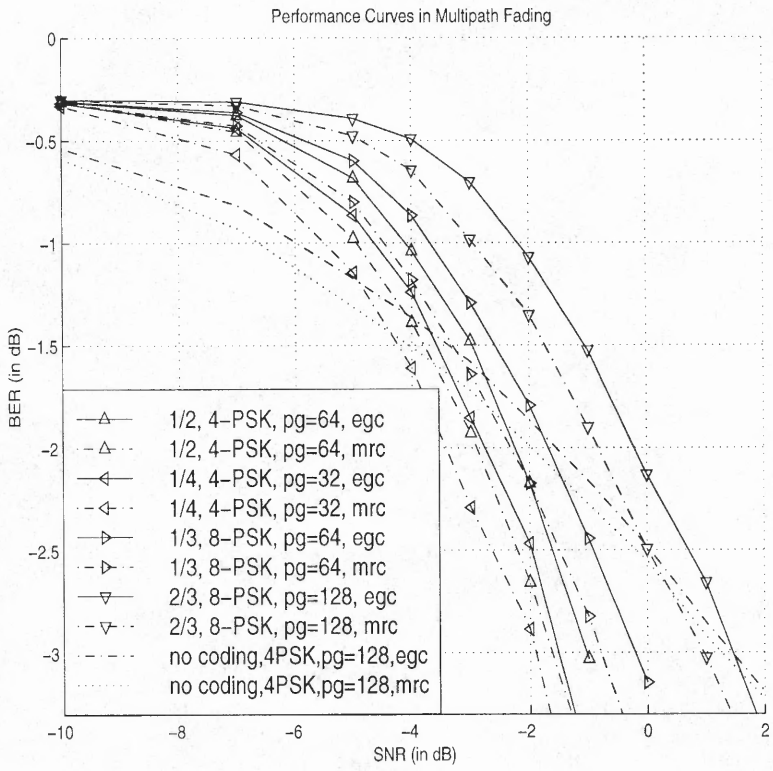

Figure 5.16 Performance characteristics (with RCPC codes) in multipath fading environment when there are two active users.

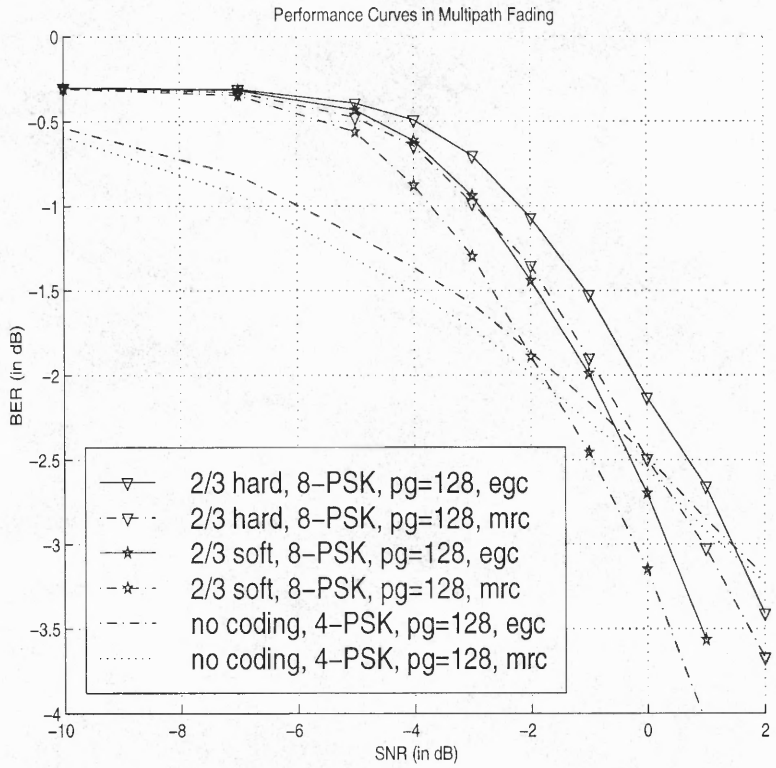

Figure 5.17 Soft vs hard decision decoding for the fourth rate configuration in performance characteristics (with RCPC codes) in multipath fading environment when there are two active users.

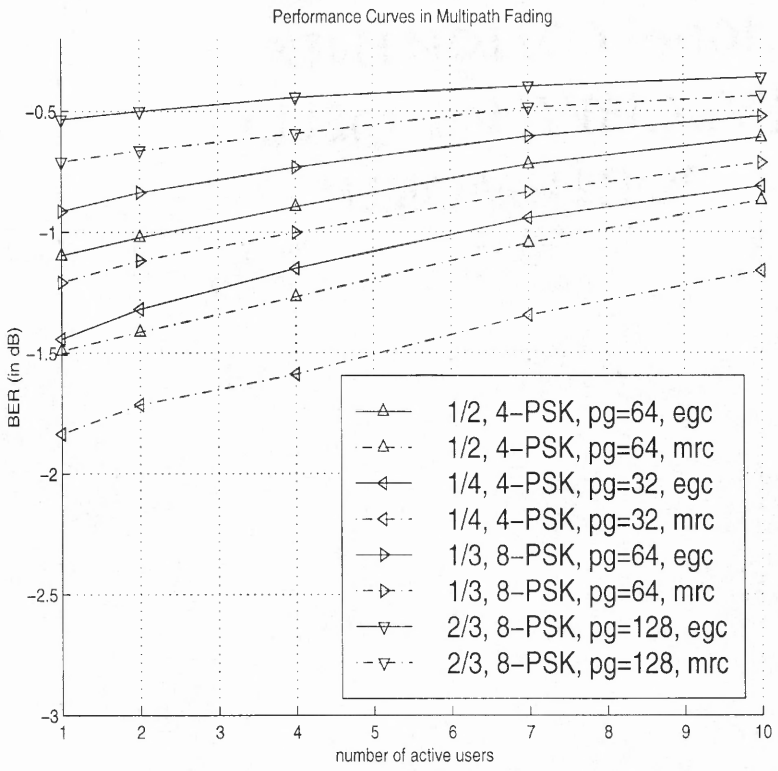

Figure 5.18 Bit error rates (with RCPC codes) in multipath fading environment at a specific SNR for different numbers of active users.

CHAPTER 6

MULTICODE CDMA DOWNLINK IN SHADOWED MULTIPATH FADING

It is possible to provide a user with high data rates by assigning multiple codes. Multiplexing the high rate bit stream to seperate branches allows us to share the allocated bandwidth with the existing IS-95 services without any burden. Providing extended bandwidth for the multicode user appears as additional active user interference for already active existing users. This method is used with two different iterative decoding methods and compared in two different synchronous downlink schemes operating under given channel conditions with the same transmission bandwidth as in IS-95. Performance characteristics of multicode CDMA downlink with systematic convolutional (Turbo) coding are obtained under shadowed multipath fading mobile channel. Multicode CDMA with LogMAP decoding [37] is observed to provide better QoS with lower bit and frame error rates, reasonable complexity and shorter decoding delay compared to DS-CDMA downlink with single code pair assigned to each user.

6.1 Multicode CDMA with Higher Data Rates and Overlaying Capability

To meet the needs for the third generation of wireless communication systems, a wideband spread spectrum radio interface that uses Code Division Multiple Access technology is being standardized. Providing a multitude of services, each with different QoS and input data rate requirements on a given fixed transmission bandwidth with overlay capability on existing IS-95 system is pointed [24] as the challenge for the standardization process. Variable coding, modulation rates and spreading factors with fixed transmission bandwidth in downlink DS-CDMA

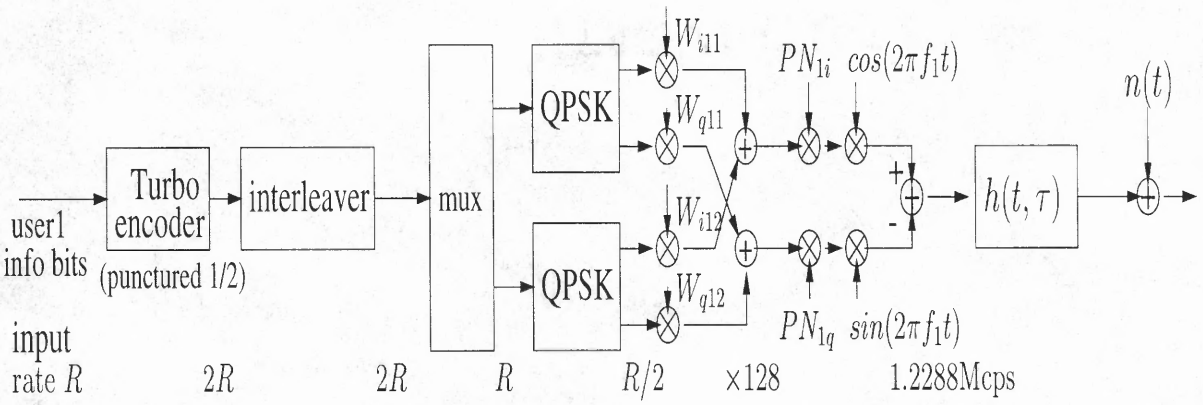

Figure 6.1 Systematic convolutional (Turbo) coded, multicode CDMA downlink transmitter.

physical layer is shown to be one way to provide different performance characteristics in additive white Gaussian noise, flat and frequency selective fading mobile environments [36]. Performances of different interblock rate configurations were compared and trade-off possibilities on transmission parameters were discussed in Chapter 6.

In this part, multicode CDMA downlink performance is investigated and tested with the already proven downlink system used earlier in Chapter 6. For the coding block in the DS-CDMA downlink, systematic convolutional (Turbo) codes are used which make use of time diversity through interleaving. On the receiver side, two different iterative decoding techniques [37] are used and their performances are compared. To achieve higher data rates, it is possible to allocate multiple code channels [24]. Multiple orthogonal codes are assigned to users on multiplexed branches with lower rates. This multicode scheme is implemented and performance simulations are obtained in shadowed frequency selective mobile fading channel based on maximum vehicular velocity, base-mobile distance and empirical modeling

[16, 38, 39]. Multicode DS-CDMA downlink performance results are compared with single code pair per user downlink where no multiple spreading codes are assigned to users and no multiplexing is used. Performances of both systems are obtained under the same channel conditions.

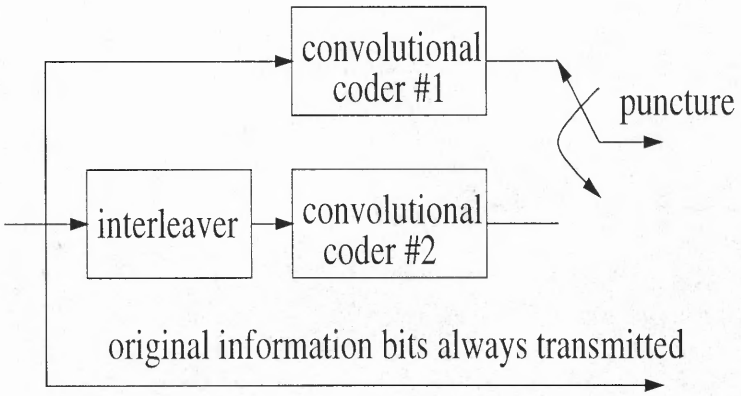

Figure 6.2 Systematic convolutional (Turbo) coder.

In the next section, the downlink DS-CDMA system with its building blocks are described. The structures of the multicode system and the system that uses no multiplexing with a pair of single orthogonal code (on inphase and quadrature channels) allocated to each user are detailed. The shadowing, excess delay and fading parameters of the wireless channel are explained in the simulation details. In the last section, the simulation results, advantages and disadvantages of both downlink schemes are compared and discussed.

6.2 Direct Spread and Multicode Downlink Systems Description

In the multicode CDMA downlink transmitter, there are coder, interleaver, multiplexer, digital modulator, Walsh-Hadamard orthogonal seperation on inphase and quadrature channels, user specific long PN code spreading and RF modulator blocks as shown in Figure 6.1. Turbo encoder consists of two systematic recursive convolu-

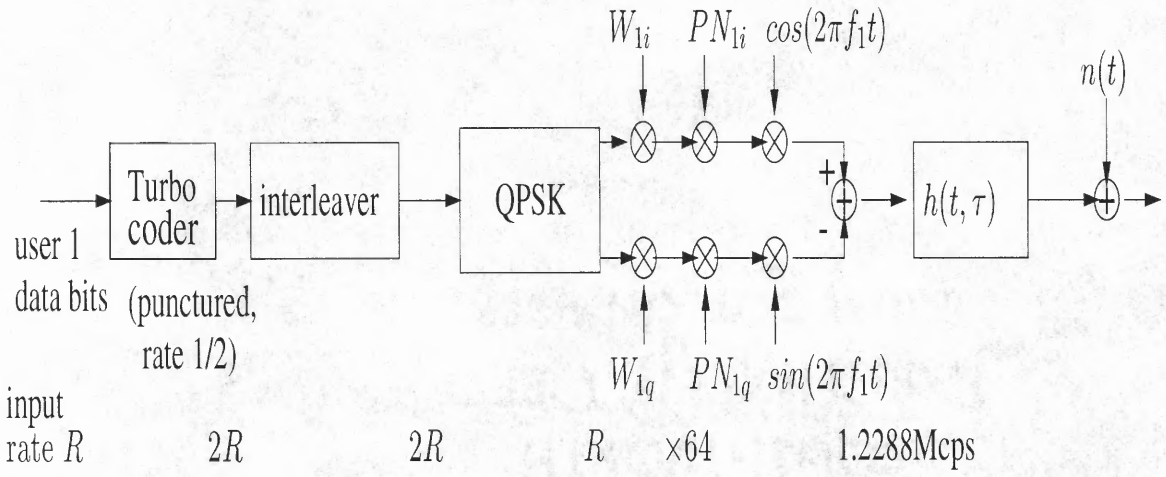

Figure 6.3 Systematic convolutional coded, single code pair per user DS-CDMA downlink transmitter.

tional codes operating in parallel [37]. As shown in Figure 6.2, the first constituent coder encodes the input information bits in their original order. The second encodes the output of a Turbo interleaver which pseudorandomly scrambles the original information bits. The original information bits are always transmitted. The output of the constituent encoders are selected according to the desired coding rate. For our purposes, one out of every two parity bits are punctured to obtain a coding rate of 1/2. The output of the Turbo coder is interframe interleaved. This provides approximately 20ms interleaving seperation in subsequent bits as in IS-95. In the multicode CDMA downlink, multiplexer reduces the rate of the sequence at each multiple branch. Digital modulation is carried out by QPSK. Gray encoding is present among the subsequent nodes in the constellation. Complex symbols of the digital modulation are seperated into inphase and quadrature components as in Figure 6.1. Then, the user bits seperated into these multiple branches are individually spread with different orthogonal Walsh codes. Thus multiple orthogonal codes are assigned to a single user.

Spread components at inphase and quadrature branches of both multiplexed streams are combined and further spread with user specific long PN codes which are $2^{42} - 1$ chips long [29]. The same characteristic polynomial is used here as in Chapter 6. RF modulation is done at 2 Ghz in which the wireless channel is simulated. The shadowing will be explained in the following section.

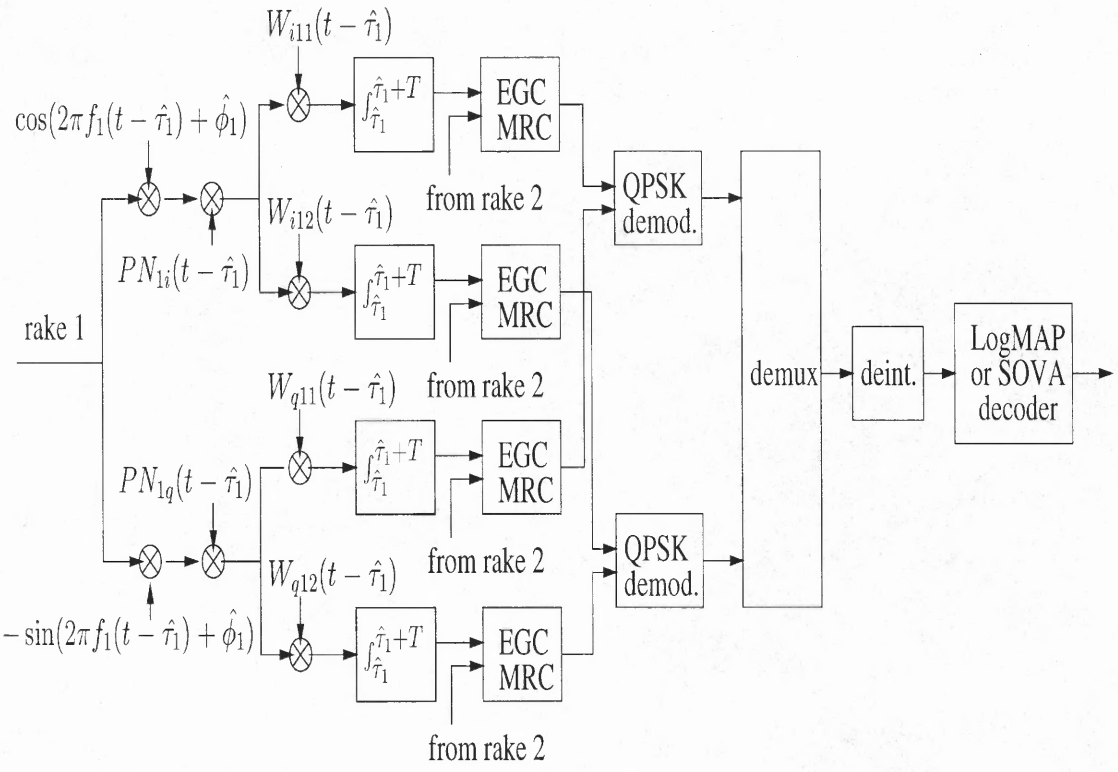

Figure 6.4 Multicode CDMA downlink receiver. Only one rake finger is shown.

DS-CDMA downlink transmitter where a single pair of orthogonal codes are assigned per user are shown in Figure 6.2. The same coding rate is used. There is no multiplexer and the rate is thus higher than multicode. To achieve the same transmission rate of 1.2288 Mcps, spreading is done with half of the processing gain of the multicode scheme.

The receivers of both schemes consist of RAKE fingers that operate on the multipath components of the received signal. In Figure 6.4, only one of the RAKE multicode receivers is shown where the combining blocks make use of the other parallel RAKE finger matched filter outputs. Each RAKE operates on the corresponding path response, despreading the long PN code from the RF demodulated signal and despreading the orthogonal multicodes at each multiplexed branch. Perfect channel estimation is assumed. Digital demodulator outputs are demultiplexed and deinterleaved. For the decoder, symbol-by-symbol maximum a posteriori (LogMAP) and soft-in/soft-out Viterbi algorithm (SOVA) [37] are implemented.

The receiver for single code pair per user DS-CDMA downlink was shown in Figure 5.14.

6.3 Shadowing Path Gain - Delay Spread Propagation Model

In addition to the mobile multipath fading channel model with Doppler spectral shaping in Chapter 2, we also consider shadowing in this chapter. With shadowing, the effects of base-to-mobile distance, correlation between delay spread and shadow fading [38] are taken into account for a more realistic simulation of the mobile radio channel including large-scale effects on the propagation environment. The compact statistical model for the joint distribution of path gain and delay spread are combined with empirical evidence, drawn from a wide range of published reports. The model is suitable for use with the Monte Carlo simulations in this chapter.

Path gain is defined as the received power to transmitted power. The propagation model consists of locally averaged path gain g and the effect to path gain, scattering or multiple echoes (multipath). The fading is modeled as described in Chapter 2. Path gain, g, characteristically falls as a power γ of base-to-mobile distance, typically $3 < \gamma < 4$. It has a random variation caused by large-scale shadowing. Its distribution is Gaussian with standard deviation between 6-12dB.

Multipath delay was described in Chapter 2 and its multipath dispersion effect (inter-symbol interference, ISI) and decision feedback equalization as multipath mitigation solution was shown in Chapter 4. In the CDMA spread spectrum downlinks, RAKE finger combining has been the focus for the last three chapters.

The relevant index of multipath dispersion is square root of the second central moment of the power-delay profile, τ_{rms}. According to the conjectures with collected empirical evidences in [38], τ_{rms} is lognormal at any distance, its median increases with distance, τ_{rms} tends to increase with shadow fading.

Taking the normalized path gain at delay τ_i as

$$S_i = P_i/g, \quad where \ g = \sum_i P_i, \quad and \quad \sum_i S_i = 1, \tag{6.1}$$

power-delay profile is defined as the $\{S_i, \tau_i\}$ set. The rms delay spread can now be computed as

$$\tau_{rms}^2 = \sum_i \tau_i^2 S_i - (\sum_i \tau_i S_i)^2. \tag{6.2}$$

The propagation in cellular channels have properties of a wide-sense stationary uncorrelated-scattering (WSSUS) [1]-[4],[16, 40, 41] as described in detail in Chapter 2. According to the postulate derived from the curve fitting collection from several published propagation measurement reports [38, 42, 43, 44, 45, 46, 47], τ_{rms} is lognormally distributed, its median and standard deviation are taken as $T_1 d^{\epsilon}$ ($0.5 \leq \epsilon \leq 1.0$) and σ_y ,respectively. Here, T_1 is the median value of τ_{rms} at base-to-mobile distance, d=1km. The probability distribution function of d selected randomly in the cell area is

$$p_d(d) = \frac{2d}{d_{max}^2}, \quad 0 \leq d \leq d_{max}. \tag{6.3}$$

The conditional pdf of τ_{rms} is

$$p_\tau(\tau_{rms}|d) = \frac{10/\ln 10}{\sqrt{2\pi}\sigma_y \tau_{rms}} exp\{-\frac{1}{2}[\frac{\ln \tau_{rms} - \ln(T_1 d^{\epsilon})}{\ln 10 \sigma_y/10}]^2\}. \tag{6.4}$$

Integrating (7.4) using (7.3) and with the substitution of $u = \ln x$, the probability distribution function of τ_{rms} can be found as

$$p_\tau(\tau_{rms}) = \frac{1}{\epsilon\tau_{rms}} exp(\frac{2y}{\epsilon} + \frac{2(\sigma_y \ln(10)/10)^2}{\epsilon^2}) \cdot erfc(\frac{y}{\sqrt{2}(\ln(10)\sigma_y/10)} + \frac{\sqrt{2}(\ln(10)\sigma_y/10)}{\epsilon}), \quad (6.5)$$

where $y \triangleq \ln(\tau_{rms}/T_1 d^\epsilon)$. So, from (6.5) it is clear that the distribution of τ_{rms} is lognormal and at a distance d, $10\log\tau_{rms}$ tends to be Gaussian distributed. The variation of decibel shadow fading (path gain) about its median is also Gaussian distributed. The mathematical model can be written as follows. The path gain or shadow fading is

$$g = \frac{G_1}{d^\gamma} x, \quad (6.6)$$

where d is in km and $3 \leq \gamma \leq 4$. The median value of g at d=1km is calculated by the empirical formula provided in [39],

$$G_1 = L_p = 69.55 + 26.16\log_{10}(f_c) - 13.82 \times log_{10}(h_b) - a \times h_m + (44.9 - 6.55\log 10(h_b))\log 10(d) \quad (dB), \quad (6.7)$$

where h_b is the effective base station antenna height in meters (taken as 30m in simulations), f_c is the carrier frequency in MHz, a is a correction constant, h_m is the effective mobile height ($a \times h_m$ is taken to be 0dB in the simulations), and x is a lognormal variable which makes $X = 10\log(x)$ a Gaussian random variable at distance d, having zero mean and standard deviation, σ_x, between 6-12dB. Delay spread can be written as

$$\tau_{rms} = T_1 d^\epsilon y, \quad (6.8)$$

where T_1 is the median value of rms delay spread at 1km taken in microseconds, ϵ is an exponent $0.5 \leq \epsilon \leq 1$, and y is a lognormal variable which enables $Y = 10\log(y)$

to be a Gaussian random variables at distance d, having zero mean and a standard deviation, σ_y, between 2-6dB. The correlation between g and τ_{rms} is represented as

$$\rho = \frac{cov(X,Y)}{\sigma_x \sigma_y}, \quad where \quad cov(X,Y) = E[(X - m_x)(Y - m_y)], \tag{6.9}$$

and

$$\overline{XY} = \rho \sigma_x \sigma_y. \tag{6.10}$$

The correlation coefficient, ρ, should be negative because large τ_{rms} is associated with small g. Figures 6.5 and 6.6 show 5000 realizations for distribution of rms delay spread and shadowing path loss for $\gamma = 3.74$ and correlation coefficient ρ =0, -0.5, -0.65, and -0.85. For each of the Monte Carlo runs in the simulations explained in the next section, a new delay spread shadowing path loss pair is generated for $\rho = -0.75$ and γ=3.74 as used in [38]. This distribution with 5000 realizations is shown in Figure 6.7.

6.4 Performance Simulation Results under Shadowed Multipath Fading

For both the multicode CDMA and DS-CDMA schemes, the transmission chip rate is kept constant. Coding, digital modulation and spreading blocks change the rates as shown in Figures 6.1 and 6.3. The fading channel is assumed to stay unchanged during one transmission symbol as shown in Figure 5.8. This assumption is applied for simulations of both schemes for a fair comparison. Multipath (frequency selective) environment is simulated with two Rayleigh fading paths. In all realizations, Rayleigh fading coefficients are Doppler shaped [16], assuming a 70mph maximum vehicular velocity in the time-varying mobile radio channel as described in Chapter 2. Base-to-mobile distance is taken randomly with the probability distribution function discussed in the previous section. Correlated rms delay spread and shadow path-loss [38] are calculated as a function of base-to-mobile distance. In Figure 6.7, a realization of delay spread and shadow path-loss is shown for base-to-mobile

distance of 1km as they are used in our simulations. In all the simulations, empirical propagation parameters are taken as in [39] which were reviewed in the previous section.

Performance characteristics of multicode CDMA downlink are shown in Figures 6.8-10. Since diminishing returns are obtained, iterations for both LogMAP and SOVA decoding are terminated at 5. All iteration results with equal gain combining and maximum ratio combining are averaged for a number of Monte Carlo runs. At each run, a new shadow realization is generated. Approximately 20ms of frame size corresponding to 400 information bits/frame/user is assumed and frame error rates are obtained as in Figure 6.10. Performance of single code per pair DS-CDMA scheme with LogMAP and SOVA decoding under the same channel conditions are shown in Figures 6.11 and 6.12. All 5 iteration results are included for both decoding methods. For multicode single code comparison, however, only 1 and 5 iteration results are included. These comparisons are plotted in Figures 6.13-16. Symbol-by-symbol maximum a posteriori (LogMAP) decoding method performs better than SOVA method which is comparable to Viterbi decoder in complexity. Decoding delay of LogMAP method is also noted to be shorter compared to SOVA. Multicode CDMA receiver with LogMAP decoder needs approximately 0.6dB less input E_b/N_0 to achieve $10^{-3.5}$ bit error rate in shadowed frequency selective fading channel with maximum ratio combining compared to the receiver with SOVA decoder for 5 decoding recursive iterations. Multicode CDMA scheme outperforms single code scheme in both decoding methods. With maximum ratio combining and 5 LogMAP iterations, multicode CDMA scheme needs approximately 1.5dB less input E_b/N_0 than single code DS-CDMA to achieve a bit error rate of 10^{-2}. Multicode scheme can also be observed to perform better under the given conditions from frame error rate curves.

Multicode system, as shown in Figure 6.4, consists of multiplexed parallel branches. In the multicode scheme, when the same processing gain is assigned as the DS-CDMA, each branch appears as a new active standard service user to the system which gives multicode scheme the overlay capability. Without any modifications on the existing standard voice services, multicode scheme can offer twice or higher the rate offered by the standard service. The offered rate can be adjusted by the number of multiplexed branches. Each branch with its unique orthogonal code appears as a new user interference on the other users.

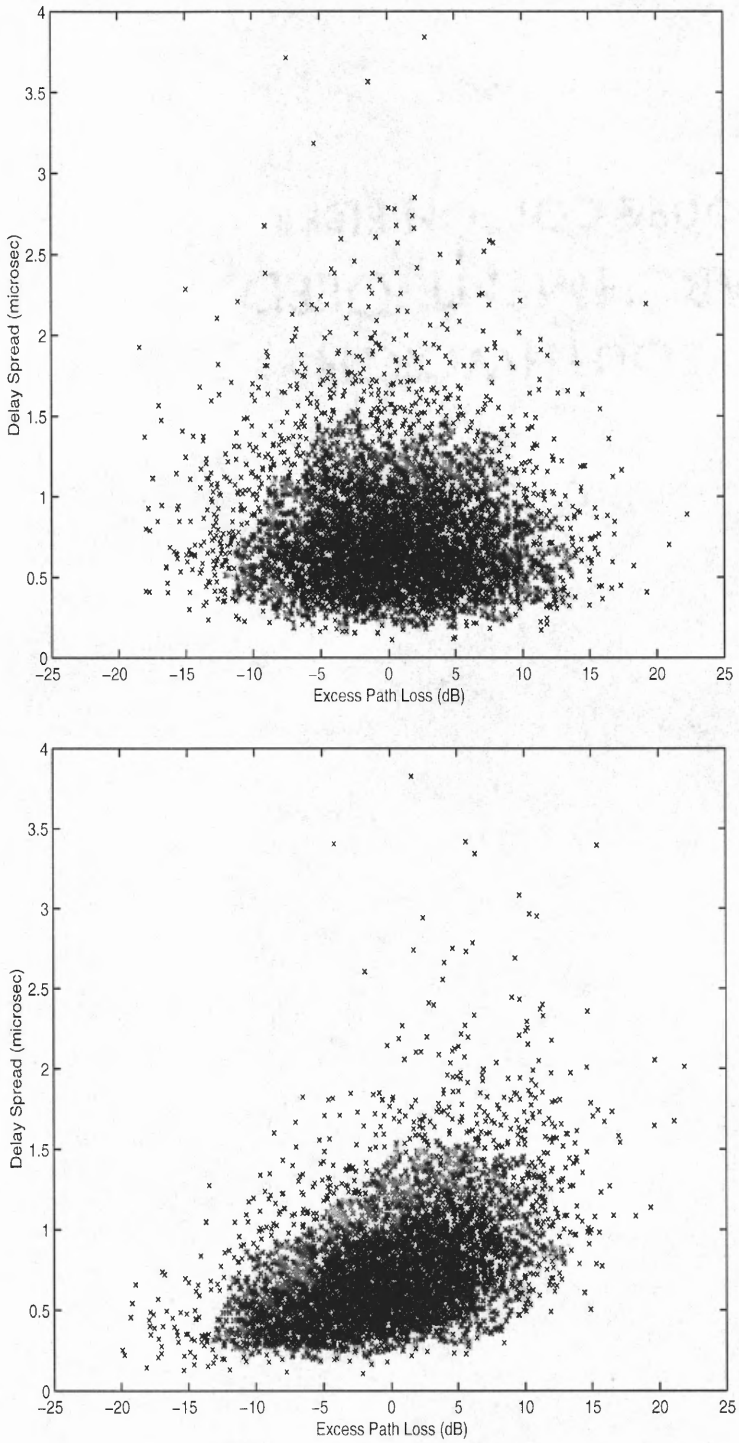

Figure 6.5 Realization of correlated shadow path-gain and delay spread at 1km base-mobile distance, a) $\rho = 0$, b) $\rho = -0.5$.

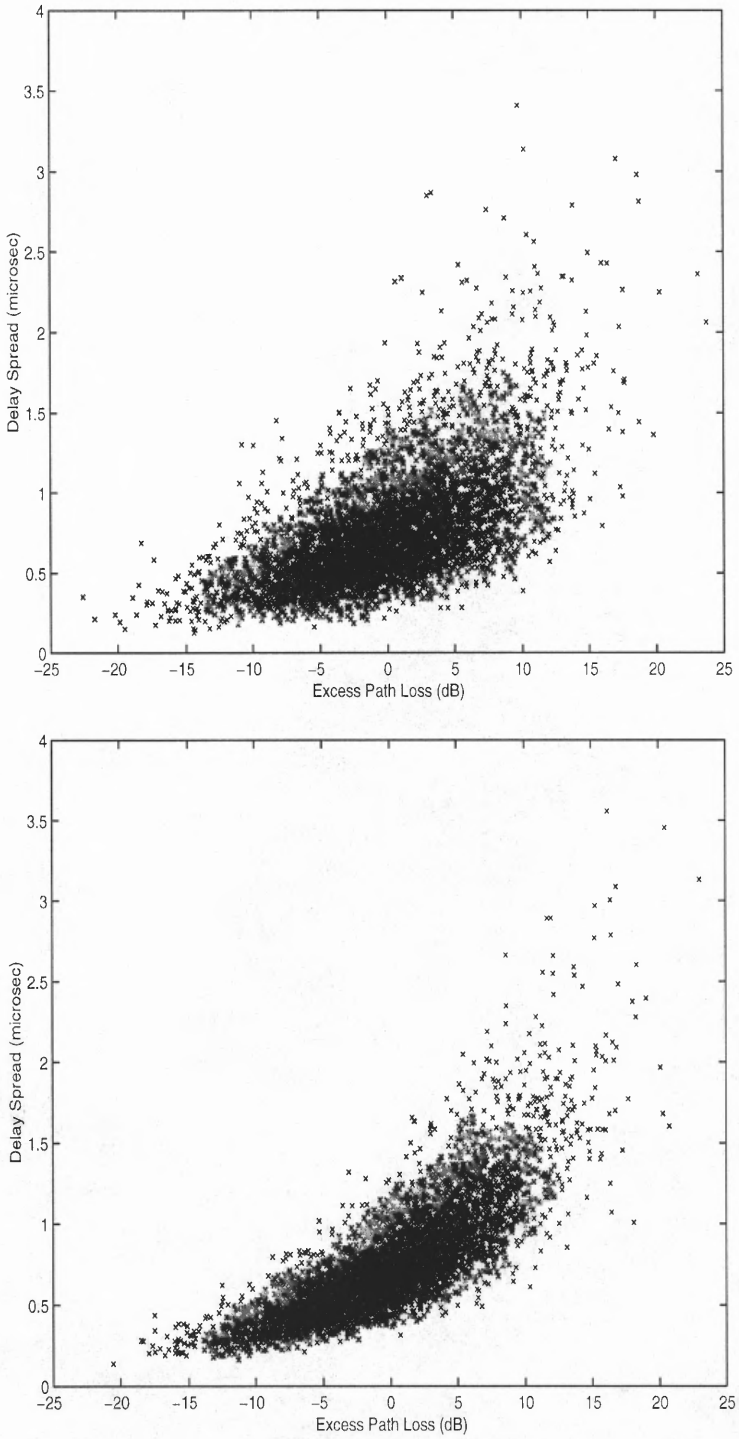

Figure 6.6 Realization of correlated shadow path-gain and delay spread at 1km base-mobile distance, a) $\rho = -0.65$, b) $\rho = -0.85$.

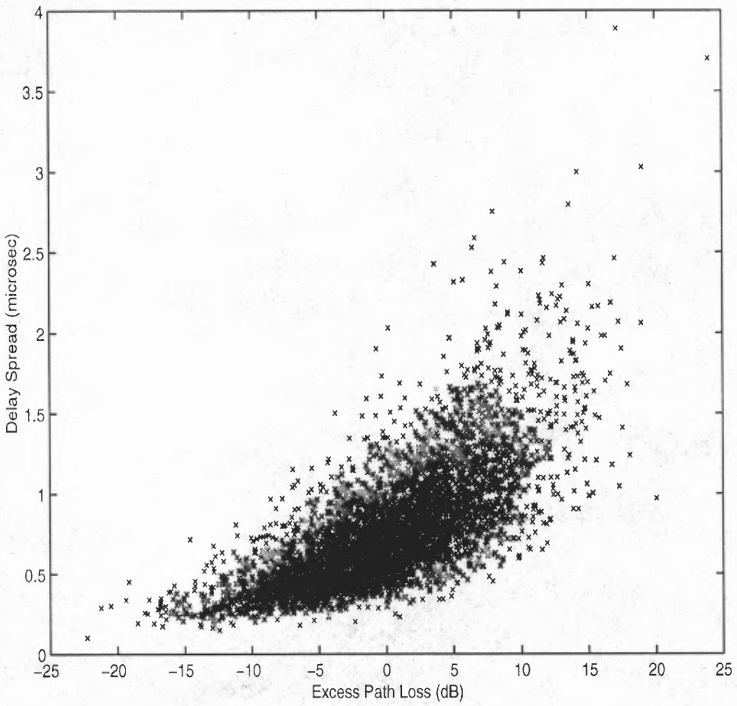

Figure 6.7 Distribution of correlated shadow path-gain and delay spread at 1km base-mobile distance as they are used in simulations, $\rho = -0.75$.

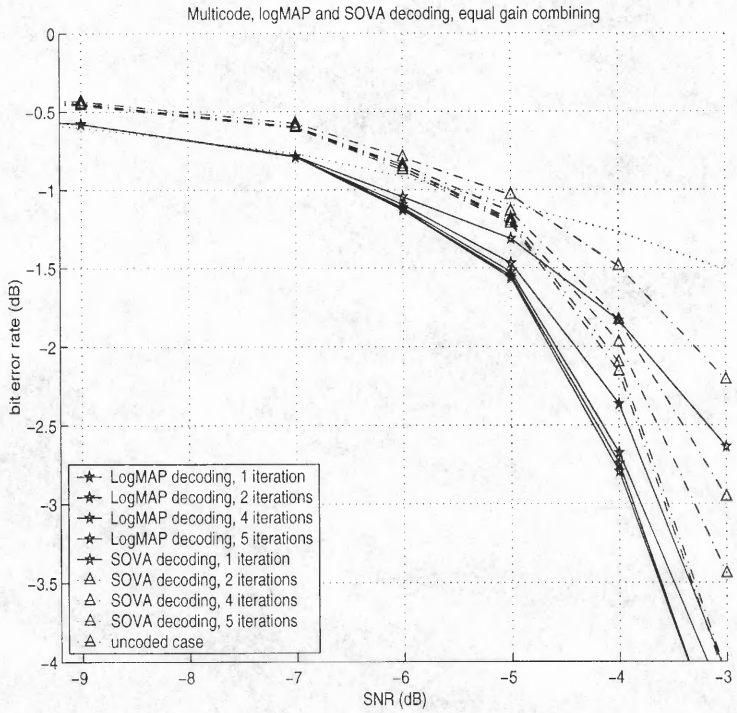

Figure 6.8 Multicode CDMA downlink bit error rates in shadowed frequency selective fading mobile channel with equal gain combining.

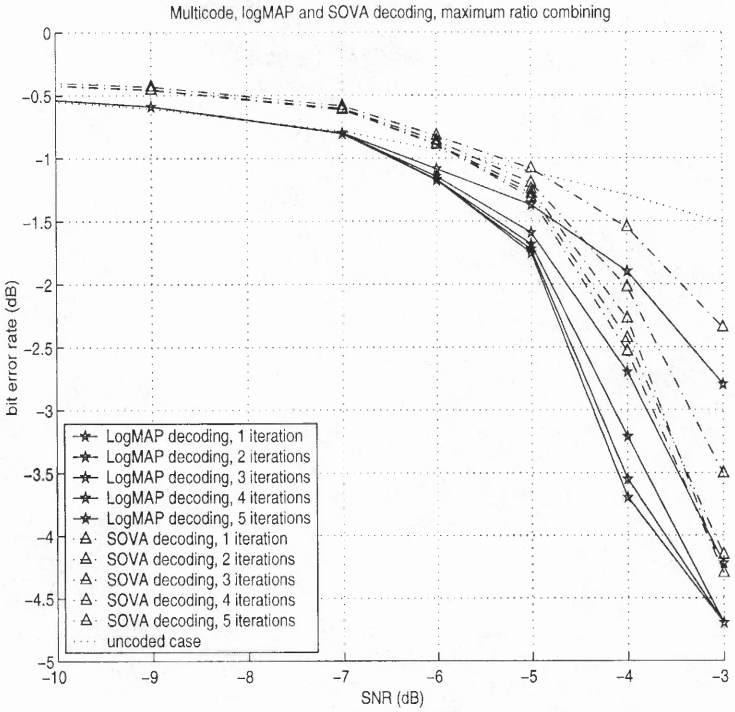

Figure 6.9 Multicode CDMA downlink bit error rates in shadowed frequency selective fading mobile channel with maximum ratio combining.

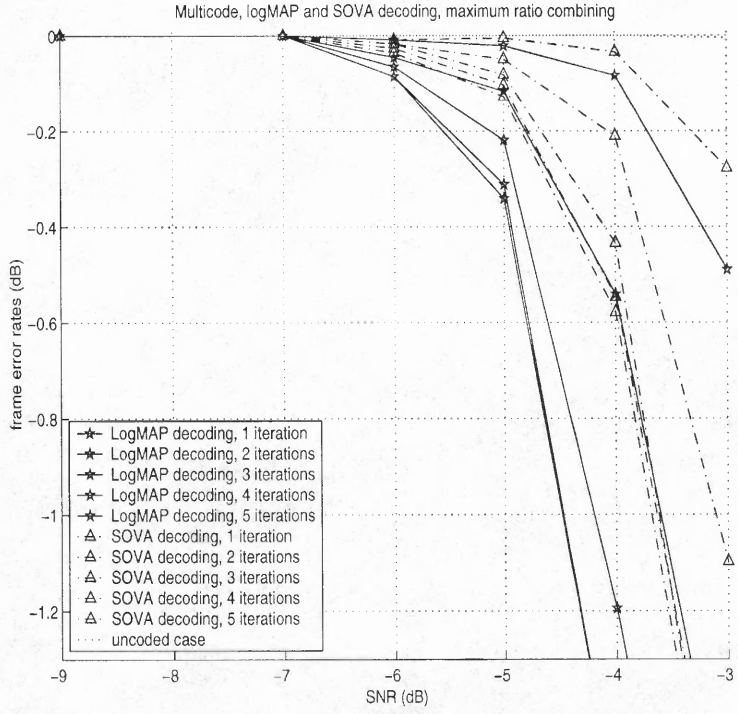

Figure 6.10 Multicode CDMA downlink frame error rates in shadowed frequency selective fading mobile channel, maximum ratio combining.

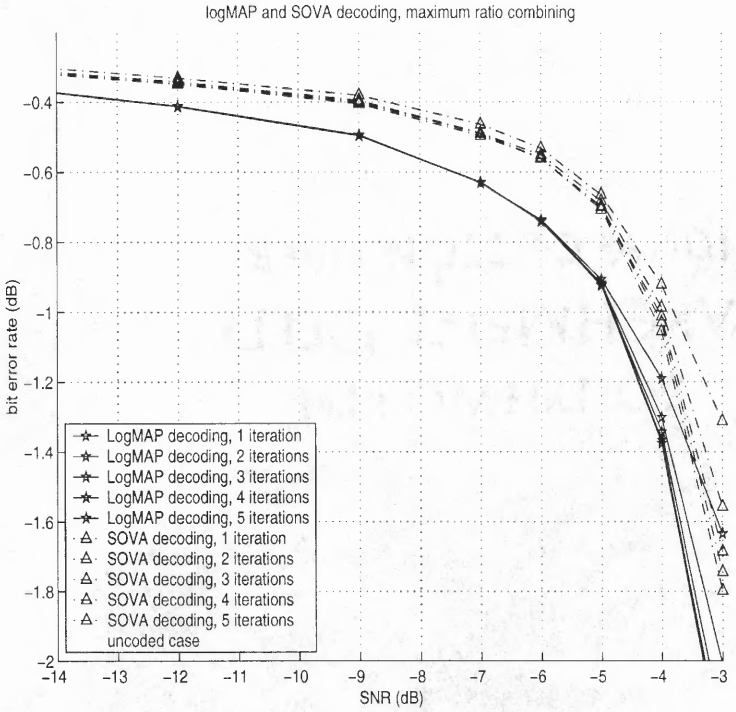

Figure 6.11 Single code pair per user DS-CDMA downlink bit error rates in shadowed frequency selective fading mobile channel, maximum ratio combining.

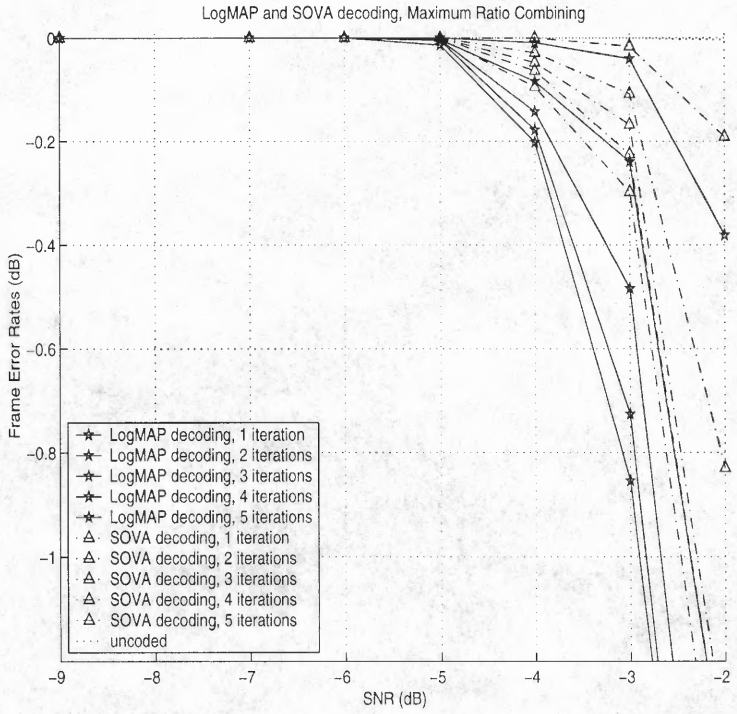

Figure 6.12 Single code pair per user DS-CDMA downlink frame error rates in shadowed frequency selective fading mobile channel with maximum ratio combining.

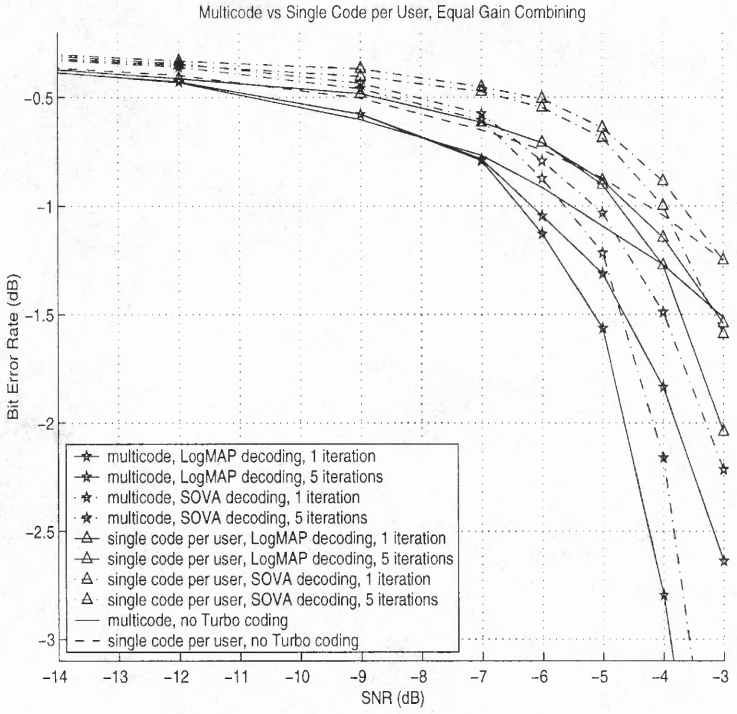

Figure 6.13 Multicode versus single code CDMA downlink bit error rates in shadowed frequency selective fading mobile channel with equal gain combining

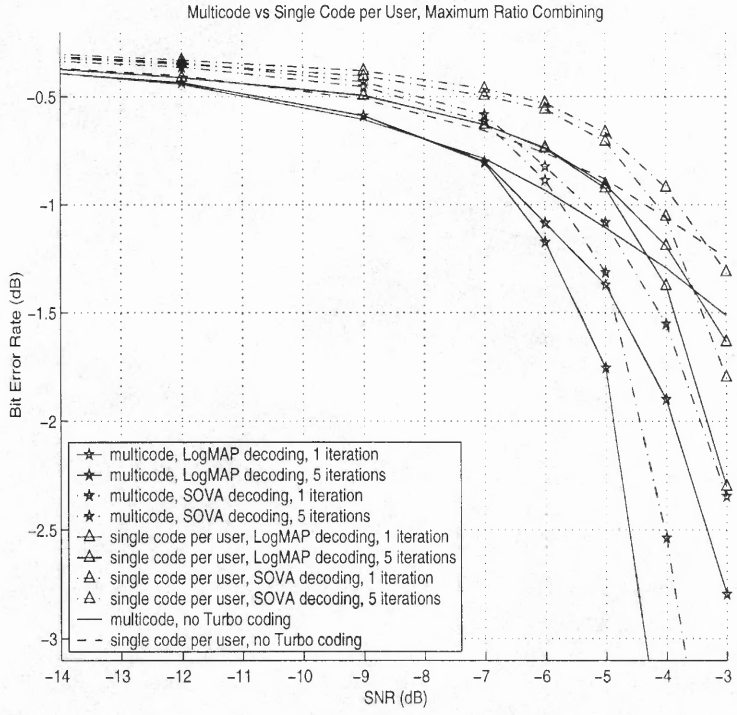

Figure 6.14 Multicode versus single code CDMA downlink bit error rates in shadowed frequency selective fading mobile channel with maximum ratio combining.

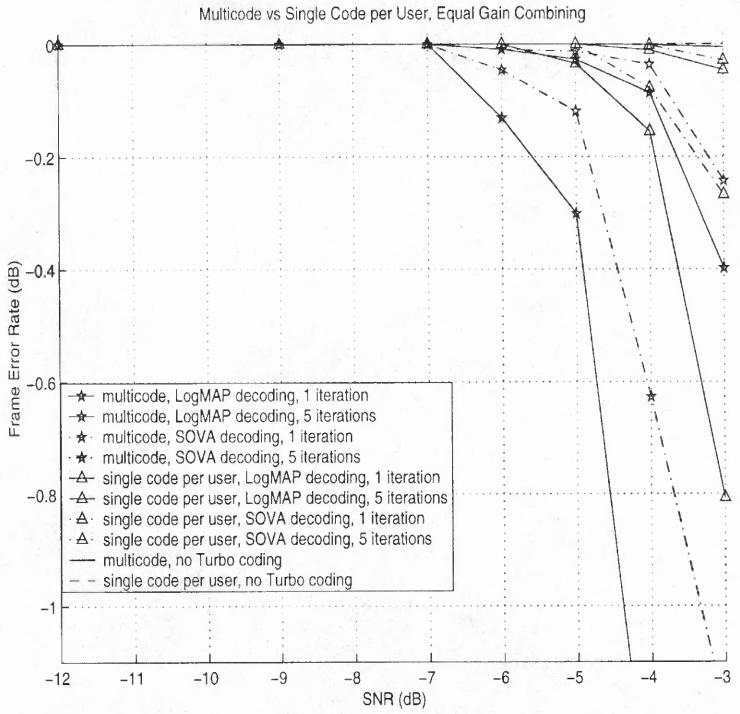

Figure 6.15 Multicode versus single code CDMA downlink frame error rates in shadowed frequency selective fading mobile channel with equal gain combining

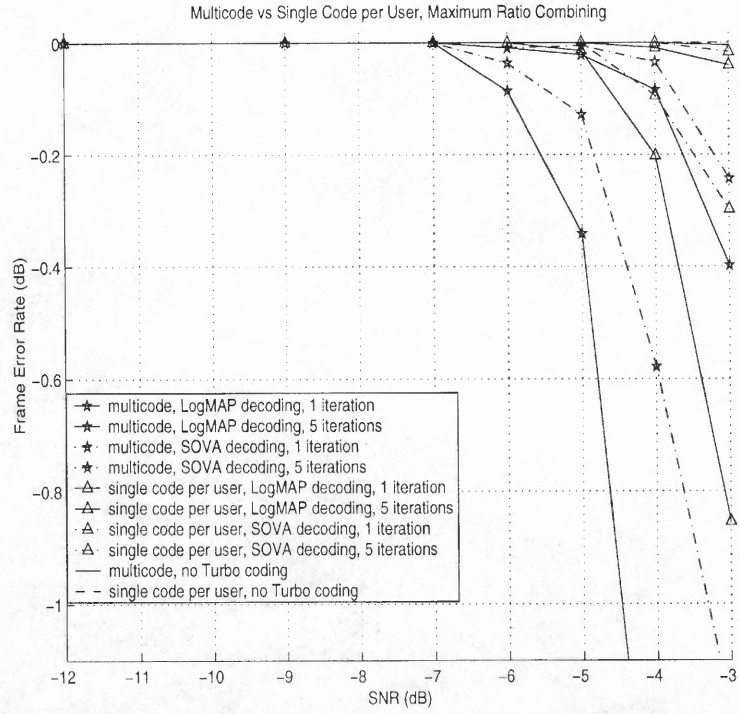

Figure 6.16 Multicode versus single code CDMA downlink frame error rates in shadowed frequency selective fading mobile channel with maximum ratio combining.

CHAPTER 7
CONCLUSIONS

The main resource for radio link is channel availability. Wireless mobile channel imposes limitations on the physical layer communication reliability, introducing delays and fades, thus appears as the main challange in achieving reliable high data rates and satisfying the quality of services. The following paragraphs summarize our contributions to allocate the resources in downlink physical layer.

Channel energy is not distributed evenly in the spectrum. To localize the unevenly distributed energy concentration in spectrum, multirate signal processing techniques are used for filter design. Composite time-varying mobile wireless channel modeling techniques are used to prepare received pilot signals as inputs to trace the energy concentration for indoor, pedestrian and vehicular environments. Irregular tree structure is formed according to channel data and practical perfect reconstruction quadrature mirror filters are implemented for analysis/synthesis. With the tree structure, we are able to modify the multiresolution one can achieve. It is found that narrower filters need to be implemented for channels with higher rate of change (higher Doppler frequencies or higher mobile speeds). The algorithm runs each time new channel data is available. Thus, tree structure traces the energy localization in the channel adaptively. With synthesis filters, the original signal is retrieved with negligible reconstruction error.

After irregular filter structures, equal bin subbands in frequency spectrum which corresponds to Discrete Multitone or Orthogonal Frequency Division Multiplexing methods are analyzed for multicarrier option of next generation wireless services. Noise levels in the multicarriers, environmental effects and availability of the channel are related to achievable bit rates using generic adaptive loading. Optimum power loading technique is used in each QAM modulated multicarrier to maximize total achievable bit rate. Channel delays and magnitudes are randomized

by adding Gaussian random variables. The variance is used as a measure to represent randomness in the channel parameters. Bandwidth efficiency or average achievable bit rate is found as a function of delay and magnitude randomness, scatterer numbers and maximum Doppler frequency. Advantages/disadvantages of using multicarrier systems versus single carrier systems are analyzed with decision feedback equalization.

In CDMA systems, for a fixed bandwidth allocation, the transmission rate can be altered by varying one or more of the coding, interleaving, modulation and spreading block parameters. In the downlink of DS-CDMA systems, once the parameters of the above mentioned blocks are set, the base station will transmit at the lowest power level that can provide the QoS requirements of the service provided. Spreading gains, coding rates, modulation sizes, ie. interblock data rates can be set jointly for each active user to maximize the total throughput of the system. In order to see how varying interblock data rate configurations would perform, performance analysis is done with the constraint of keeping transmission bandwidth fixed for all configurations as in IS-95. Various coding, modulation and spreading rate combinations yield different performance characteristics in AWGN, flat fading and multipath environments permitting trade-off decisions on choices of rate, QoS, and implementation. Given fixed transmission bandwidth and equal active user transmission powers, four different rate configurations among the coding, digital modulation and spreading blocks are compared in AWGN, flat fading and multipath fading mobile environments for a DS-CDMA downlink system. Regardless of the chosen modulation indices and spreading gains, the coding rates dominate the bit error rate performance characteristics for the rate configured systems. Higher processing gains in the spreading block are not sufficient to compansate the loss due to weaker coding for the given conditions in our performance simulations.

Given fixed transmission bandwidth, bit and frame error rate performance characteristics of multicode CDMA downlink with systematic convolutional (Turbo) coding are obtained under shadowed frequency selective fading mobile wireless channel. LogMAP and SOVA Turbo decoding methods are compared in two different synchronous downlink scenarios operating on long and short term fading channel conditions. Correlated shadow fading and delay spread distribution is generated. In addition to shadowing fade, temporal Doppler correlated Rayleigh fading is applied independently for each multipath. Correlated shadow fade - delay spread pair is updated for each Monte Carlo run. Multicode CDMA performance is observed to outperform the DS-CDMA downlink with single pair of orthogonal codes assigned to each user. Multicode CDMA downlink with LogMAP decoding appears to provide a better QoS with lower bit and frame error rate, shorter decoding delay and reasonable decoding complexity. Multicode scheme also allows higher data rate services with overlay capability on existing voice services without any modifications.

REFERENCES

1. P. A. Bello, "Characterization of randomly time-variant linear channels", IEEE Transactions on Communication Systems, pp. 360-393, Dec. 1963.

2. H. Suzuki, "A Statistical Model for Urban Radio Propagation", IEEE Transactions on Communications, Vol. Com.25, No. 7, July 1977.

3. H. Hashemi, "Simulation of the Urban Radio Propagation Channel", IEEE Transactions on Vehicular Technology, Vol. VT-28, No. 3, Aug. 1979.

4. T. S. Rappaport, et. al., "Statistical Channel Impulse Response Models for Factory and Open Plan Building Radio Communication System Design", IEEE Transactions on Communications, Vol. 39, No. 5, May 1991.

5. R. K. Young, Wavelet theory and its applications. Kluwer Academic Publishers, 1995.

6. A. N. Akansu and R. A. Haddad, Multiresolution Signal Decomposition. Academic Press, 1992.

7. M. V. Tazebay, "On optimal design and applications of linear transforms", Ph.D dissertation, New Jersey Institute of Technology, Jan. 1996.

8. P. P. Vaidyanathan, Multirate Systems and Filter Banks, Prentice Hall, New York, 1993.

9. Irving Kalet, "The multitone channel", IEEE transactions on communications, Vol. 37, No. 2, Feb. 1989.

10. Xueming Lin, "Orthogonal transmultiplexers: extensions in digital subscriber line (DSL) communications", Ph.D dissertation, New Jersey Institute of Technology, Jan. 1998.

11. J. M. Cioffi, et. al., "MMSE Decision-feedback equalizers and coding - parts I and II", IEEE transactions on communications, Vol. 43, No. 10, Oct. 1995.

12. A. Bircan, S. Tekinay, A. N. Akansu, "Time-Frequency and Time-Scale Representation of Wireless Communication Channels", IEEE Time-Frequency Time-Scale Conference, Pittsburgh PA, Oct. 1998.

13. P. S. Chow, J. M. Cioffi, J.A.C. Bingham, "A practical discrete multitone transceiver loading algorithm for data transmission over spectrally shaped channels", IEEE transactions on communications, Vol. 43, No. 2/3/4, Feb., March, Apr. 1995.

14. Robert F. H. Fischer and Johannes B. Huber, "A new loading algorithm for discrete multitone transmission", IEEE Globecom 1996.

15. Andreas Czylwik "Adaptive OFDM for wideband radio channels", IEEE Globecom 1996.

16. W. C. Jakes, Microwave Mobile Communications, IEEE Press, 1974.

17. Anıl Bircan, Ali N. Akansu and Şirin Tekinay, "Model Based Capacity Measurements For Wireless DMT Channels", 33rd Annual Conference on Information Sciences and Systems (CISS), March 17-19, 1999, Baltimore, MD.

18. N. A. Zervos and I. Kalet "Optimized Decision Feedback Equalization vs Optimized OFDM for High-Speed Data Transmission Over the Local Cable Network", IEEE ICC 1989.

19. John A. C. Bingham "Multicarrier Modulation for Data Transmission: An Idea Whose Time Has Come", IEEE Communications Magazine, May 1990.

20. John G. Proakis "Digital Communications", 3rd edition, McGraw Hill 1995.

21. Simon Haykin "Communication Systems", 3rd edition, Wiley 1994.

22. N. Yee, J. P. Linnartz, G. Fettweis "MC-CDMA in Indoor Wireless Radio Networks", IEICE Transaction on Com., Japan Vol. E77-B, No7, July 1994, pp. 900-904.

23. N. Yee and J. P. Linnartz "MC-CDMA in an Indoor Wireless Radio Channel", Memorandum UCB/ERL M94/6, UC Berkeley.

24. Oguz Sunay, "IS-95 Evolution Towards the IMT-2000 Era", Biennial Symposium on Communications Kingston, Ontario, Canada, June 1998.

25. Mohammed-Slim Alouini and Andrea Goldsmith, "Capacity of Rayleigh Fading Channels Under Different Adaptive Transmission and Diversity-Combining Techniques", IEEE Transactions on Vehicular Technology, Vol. 48, pp. 1165-1181, July 1999.

26. Shinsuke Hara, T.H. Lee, R. Prasad, "BER Comparison of DS-CDMA and MC-CDMA for Frequency Selective Fading Channels", Proc. of 7th Tirrenian International Workshop on Digital Communications, Viareggio, Italy, Sep'95.

27. Leonard J. Cimini, "Analysis and Simulation of a Digital Mobile Channel Using Orthogonal Frequency Division Multiplexing", IEEE Transactions on Communications, Vol.33, No.7, July 1985.

28. Leonard J. Cimini, "Performance Studies for High-Speed Indoor Wireless Communications", Wireless Personal Communications 2: pp.67-85, 1995.

29. T. S. Rappaport, Wireless Communications Principles and Practice, Prentice Hall, 1996.

30. R.Steele, Mobile Radio Communication, IEEE Press, 1992.

31. Telia Research AB Technical Report on " Creating discrete impulse responses for ITU and ETSI fading radio channels", Nov. 26, 1997.

32. J. B. Cain et al., "Punctured Convolutional Codes of Rate (n-1)/n and Simplified Maximum Likelihood Decoding", IEEE Transactions on Information Theory, Vol. IT-25, No. 1, Jan. 1979.

33. George C. Clark, J. Bibb Cain, Error-Correction Coding for Digital Communications, New York, Plenum Press, 1981.

34. Stephen B. Wicker, Error Control Systems for Digital Communication and Storage, Prentice Hall, 1995.

35. Shu Lin, Daniel J. Costello, "Error Control Coding, Fundamentals and Applications", Prentice Hall, 1983.

36. Anil Bircan, M. Oguz Sunay, and Ali N. Akansu, "Comparison of Different Interblock Data Rate Downlinks" Proc. IEEE GlobeCom conference, Nov-Dec. 2000, San Francisco, CA.

37. Joachim Hagenauer, Elke Offer, and Lutz Papke, "Iterative Decoding of Binary and Convolutional Codes", IEEE Trans. on Inform. Theory, Vol.42, No.2, pp. 429-445, March 1996.

38. Larry J. Greenstein, Vinco Erceg, Yu Shuan Yeh, and Martin V. Clark, "A New Path-Gain/Delay-Spread Propagation Model for Digital Cellular Channels", IEEE Trans. on Vehicular Technology, Vol. 46, No. 2, May 1997.

39. Masaharu Hata, "Empirical Formula for Propagation Loss in Land Mobile Radio Services", IEEE Trans. on Vehicular Technology, Vol. VT-29, No. 3, August 1980.

40. A. Papoulis, Probability, Random Variables, and Stochastic Processes, Third Edition, McGraw Hill, 1991.

41. Alberto Leon-Garcia, Probability and Random Processes for Electrical Engineering, Second Edition, Addison Wesley, 1994.

42. D. C. Cox, "Distribution of multipath delay spread and average excess delay for 910-MHz urban mobile radio paths", IEEE Trans. Antennas and Propagation, Vol. AP-23, pp. 206-213, Mar. 1975.

43. T. S. Rappaport, S. Y. Seidel, and R. Singh, "900 MHz multipath propagation measurements for US digital cellular radiotelephone", IEEE Trans. Veh. Technology, Col. 39, pp. 132-139, May 1990.

44. D. M. J. Devasirvatham, "Radio propagation studies in a small city for universal portable communications", in Proc. 38th IEEE Veh. Tech. Conf., 1988.

45. E. S. Sousa, V. M Jovanovich, and C. Daigneault, "Delay spread measurements for the digital cellular channel in Toronto", IEEE Trans. Veh. Tech. Vol. 43, pp. 837-847, Nov. 1994.

46. J. van Rees, "Measurements of the wide-band radio channel characteristics for rural, residential, and suburban areas", IEEE Trans. Veh. Tech. Vol. VT-36, pp. 2-6, Feb. 1987.

47. T. Tanaka, S. Kozono, and A. Akeyama, "Urban multipath propagation loss and delay spread characteristics in mobile communications", Elec. Comm. Japan, Vol. 74, pp. 80-88, Aug. 1991.